POLITECNICO DI TORINO

Corso di Laurea in Ingegneria Aerospaziale

Tesi di Laurea Magistrale

Turbulent transport and evolution in transient condition of water drops across a warm cloud-air interface

Relatore
prof.ssa Daniela Tordella

Studente
Mattia Tomatis
matricola: 245879

Anno accademico 2019-2020

Abstract

The analysis of collisions of water droplets in a turbulent field is important from many points of view, with academic and industrial applications. It is a multidisciplinary problem, from the turbulent fluid dynamics to the particles growth model. In this thesis, with the help of numerical simulations, we want to investigate how water droplets collide with themselves in a turbulent cloud-clear air environment.
Of course clouds are not the only application of this multi-phase problem, indeed there are still many industrial applications in which multi-phase flows are treated or used.
In this work will be shown the numerical measurements of collision kernels in homogeneous, isotropic, cloud turbulent environment but also in very anisotropic environments as the turbulent mixing between cloud and clear air, where are distributed multi and mono disperse population of particles. A collision kernel is substantially a measure of collision probability between two classes of particles, characterized by volume (radius). These results will also be compared with the analytical model available in scientific literature. In the end of this work there is also an analysis of the tendency of droplet to group in clusters in low enstrophy portions of the domain.

Acknowledgements

I would like to thank Professor Daniela Tordella that gave me the great opportunity to work, but above all to learn, much in a multidisciplinary environment, which ranges from fluid dynamics to the dynamics of particle populations and parallel computational science. Special thanks also go to Dr. Federico Fraternale who, despite many academic commitments, has constantly provided support for this work, proving to be a friend as well as a colleague. Many thanks also go to my workmates: Dr. Mina Golshan, doctor of engineering Shahbozbek Abdunabiev and future doctor of engineering Ludovico Fossà, who contributed, with project manager Dr. Anja Visocnik, to create a profitable, peaceful and enjoyable working environment. The last, but not least, thanks go to my parents and my whole family, which has constantly provided economic and moral support for this to happen.

Computational resources were provided by HPC@POLITO, a project of Academic Computing within the Department of Control and Computer Engineering at the Politecnico di Torino (http://hpc.polito.it) and CINECA, that with the approval of the IscrC RAINFALL project, into which this thesis work is inserted, provided 560'000 CPU hours on MARCONI cluster to develop our job.

Contents

Chapter 1

Problem's equations

Introduction

In this job are reported the results of several CFD simulations of water droplets in atmospheric turbulent environments, focusing in particular on the collisions probability between droplets (direct measure of the geometric collision kernel) and on cluster mechanism that affects droplets in a turbulent environment. The problem of studying the dynamics of liquid water particles in a cloud/air turbulent system is based on a wide set of equations, some of them directly linked to the fluid dynamics (like the Navier-Stokes equations), others useful to solve thermodynamics processes (like condensation). Still others are strictly necessary to determine the dynamics of the particles. All these equations are implemented in code *DNS_TurIsMI_v141* [7], that is the processing code adopted to run all the simulations, that will allow us to investigate the phenomenon.

1.1 Navier-Stokes equations in Boussinesq approximation

The foundations on which the problem is built are the Navier-Stokes equations, in particular the incompressible ones. They describe the conservation of mass and momentum of the fluid. This set of equations has been modified in order to be adapt to describe a multiphase flow. In particular a term of buoyancy appears in the momentum balance, it is based on Boussinesq approximation: the density of the flow is considered as constant, apart for the bouyancy term. The flow that will be simulated is that of a turbulent shearless mixing, it is characterized by a null mean velocity field, which is why the Navier-Stokes equations reported refer to the fluctuations of the velocity field.

$$\begin{aligned} &\nabla \cdot \boldsymbol{u} = 0 \\ &\frac{\partial \boldsymbol{u}}{\partial t} + \boldsymbol{u} \cdot \nabla \boldsymbol{u} = -\frac{\nabla p}{\rho} + \nu \nabla^2 \boldsymbol{u} - B\boldsymbol{g} \end{aligned} \tag{1.1}$$

where:

- $\boldsymbol{u}$ is the velocity **fluctuations** vector (3D)

- ρ is the flow density, it is constant in the equations except for the buoyancy term (Boussinesq approximation)
- p is the fluid dynamic pressure
- ν is the kinematic viscosity of air
- B is the buoyancy term, it includes also weight force and it will be treated in detail in section 1.3.
- $\boldsymbol{g}$ is the gravity acceleration vector

As seen, in the equation of momentum does not appear any kind of feedback of the droplets, this is reasonable because the order of magnitude of particles radius is $\sim 10\,\mu m$, much smaller than the Kolmogorov length scale η, therefore the effects on the fluid can be neglected. A preliminary evaluation of the turbulence micro scale can be done using the order of magnitude of Reynolds number and the macro scale l of the vortexes (the choice of this value will be exposed later).

$$\left.\begin{array}{l} Re \sim 1 \cdot 10^3 \\ l \sim 0.1\,m \end{array}\right\} \Rightarrow \eta = l \cdot Re^{-\frac{3}{4}} \simeq 0.5\,mm \tag{1.2}$$

It leads to millimeters sized Kolmogorov length scale. This configuration of the problem has been used yet, see Franklin *et al*, 2004 [3]. Major details about Reynolds number and macro scale will be provided in chapter 2.

Of course this set of equation is not complete in order to solve the problem, so others equations are added.

1.2 Temperature and Froude number

The temperature is treated as a passive scalar, it means that it is evolving transported by the fluid, following the law:

$$\frac{\partial T'}{\partial t} + \boldsymbol{u} \cdot \nabla T' = K_a \nabla^2 T' + \frac{L}{c_p} C \tag{1.3}$$

Where

- T' is the **fluctuation** of temperature, its meaning is explained in the next section
- K_a is the thermal diffusivity of air
- L is the latent heat of evaporation of water
- c_p is the air specific heat at constant pressure
- C is the condensation rate per unit volume

The temperature is decomposed into a constant term and a fluctuating one:

$$T(\boldsymbol{x},t) = \underbrace{T_{min} + Gz}_{\text{background temperature}} + T'(\boldsymbol{x},t) \tag{1.4}$$

Where G is the mean temperature gradient along z direction (L is the length of the domain in that direction) and it's constant, not affected by the time evolution. In the code this will act as a source term into the momentum dynamics.

$$G = \frac{T(L) - T(0)}{L} = \frac{\Delta T}{L}$$

Conversely $T'(\boldsymbol{x},t)$ is the fluctuating temperature term, and it is the only one allowed to change with DNS evolution. In the computational domain the **initial** fluctuating temperature term T' depends only by z coordinate, with an hyperbolic tangent development:

$$T'(z,0) = \Delta T \cdot \left[tanh\left(55\left(\frac{z}{L} - \frac{1}{2}\right)\right) - \frac{2z}{L} + 1 \right] \tag{1.5}$$

The influence of temperature in **non-dimensional** momentum equation is included in the bouyancy term:

$$\frac{D\tilde{\boldsymbol{u}}}{Dt} = ... + \frac{1}{Fr^2}\left[\tilde{G}\tilde{z} + \tilde{T}'\right] \tag{1.6}$$

The stability or instability of the simulation depends on the sign of ΔT and therefore of G. We have stable condition if $G > 0$, neutral condition if $G = 0$ and unstable condition for $G < 0$. It is common, instead of using G, to refer to the squared Froude number in order to describe the stability of stratified flow. It is defined with the root mean square value of velocity fluctuations u'_{rms}, a length scale l (we selected the initial one associated to macro scale vortexes, although in literature the mixing zone length is often used) and the Brunt-Vaisala frequency $\mathcal{N}$.

$$Fr = \frac{u'_{rms}}{l\mathcal{N}} \tag{1.7}$$

Where the Brunt-Vaisala frequency indicates the oscillating frequency of a fluid particle that is slightly moved from its equilibrium condition in a stable stratification environment. It defines as

$$\mathcal{N} = \sqrt{\frac{gG}{T_{mean}}} \tag{1.8}$$

It is clear that since for unstable simulation $G < 0$, $\mathcal{N}$ will be an imaginary number, it means that it will be an amplification factor instead of an oscillation frequency. In this work we will have

$$\mathcal{N}^2 = \frac{9.81 \cdot (\pm 1.95)}{281} \simeq \pm 0.068 \ \left[s^{-2}\right] \tag{1.9}$$

In a further section we will see that $u'_{rms} \simeq 0.15\, m/s$ and that the initial macro scale of the turbulence vortexes is $l \simeq 0.085\, m$. Substituting we get

$$Fr^2 = \frac{0.15^2}{0.085^2 \cdot (\pm 0.068)} = \pm 45.4 \Rightarrow |Fr| = 6.7 \tag{1.10}$$

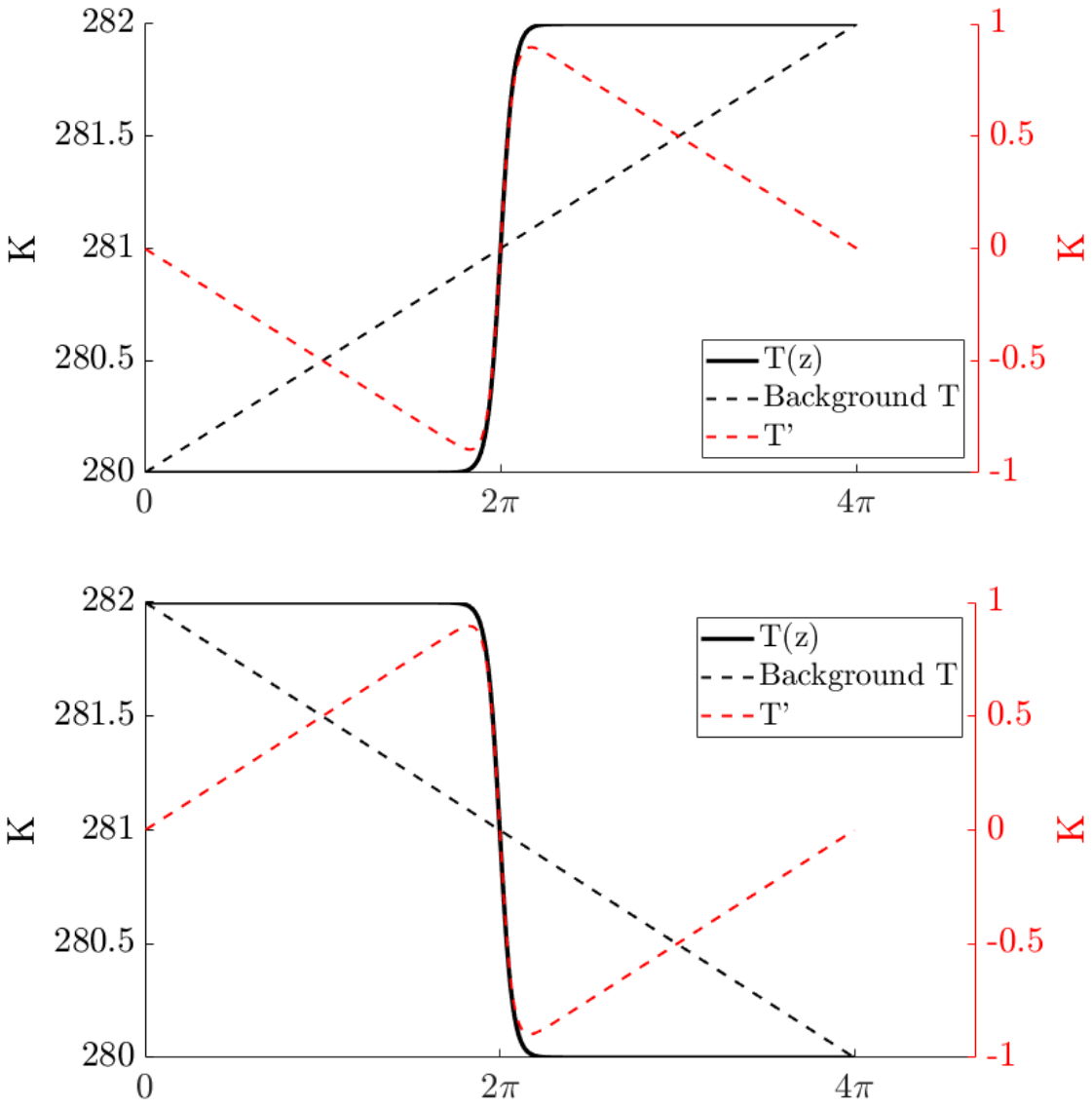

Figure 1.1. Initial temperature profile, respectively in stable and unstable condition. The code works in a way that only the red function evolves in DNS, the mean gradient is kept constant in time. This is because pseudo spectral numerical methods require periodic continuous functions.

1.3 Buoyancy

The buoyancy effect appears in the momentum equation, in particular it acts along the vertical direction. This dynamic contribution is due to the different composition of the fluid, in fact every point of the domain is characterized by a concentration of air, vapor and a temperature value. In particular the term B, that appears in the equation 1.1,

represents the dynamic effect due to density fluctuations. It is expressed as the ratio of the fluctuations $\Delta\rho$ and a constant density value ρ_0.

$$B = \frac{\rho - \rho_0}{\rho_0} = \frac{\Delta\rho}{\rho_0} \tag{1.11}$$

Now one can evaluate the term ρ in 1.11. Assuming small perturbations, using a first order Taylor's approximation around the average value ρ_0, it is possible to write:

$$\rho(\rho_a, \rho_v, T) = \rho_0 + \frac{\partial\rho}{\partial T}\Delta T + \frac{\partial\rho}{\partial\rho_v}\Delta\rho_v + \frac{\partial\rho}{\partial\rho_a}\Delta\rho_a \tag{1.12}$$

Where Δ denotes small variation from the mean value.
Since 1.11 it is

$$\begin{aligned} \frac{\partial\rho}{\partial\rho_a} &= 1 \\ \frac{\partial\rho}{\partial\rho_v} &= 1 \end{aligned} \tag{1.13}$$

The derivative $\partial\rho/\partial T$ is evaluated through the introduction of a thermal expansion coefficient α, that is inversely proportional to the average temperature T_0:

$$\frac{\partial\rho}{\partial T} \sim \rho_0\alpha = -\frac{\rho_0}{T_0} \tag{1.14}$$

Therefore relation 1.12 reduces to

$$\rho = \rho_0 + \rho_0\frac{\Delta T}{T_0} + \Delta\rho_a + \Delta\rho_v \tag{1.15}$$

The last two terms in 1.15 represent the bouyancy due to gas mixture. These are studied using the theory of incompressible gas, ignoring the volume occupied by the droplets of liquid water. Starting from the total and partial volumes, respectively v_{tot}, v_i:

- $v_{tot} = const$
- $v_i = \frac{RT}{p}\frac{m_i}{\mathcal{M}_i}$

Since $v_{tot} = \sum v_i$ it is possible to write $\sum v_i = \frac{RT}{p}\sum\frac{m_i}{\mathcal{M}_i} = const$, dividing by v_{tot} you get

$$\frac{RT}{p}\sum\frac{m_i}{v_{tot}\mathcal{M}_i} = const \Rightarrow \sum\frac{\rho_i}{\mathcal{M}_i} = const$$

Adapting this result to the air-vapor mixture

$$\frac{\rho_a}{\mathcal{M}_a} + \frac{\rho_v}{\mathcal{M}_v} = \underbrace{\frac{\rho_{a0}}{\mathcal{M}_a} + \frac{\rho_{v0}}{\mathcal{M}_v}}_{\text{constant average values}}$$

Recalling that the general variation express as $\Delta\rho_i = \rho_i - \rho_{i0}$, it is possible to rewrite

$$\Delta\rho_a = -\frac{\mathcal{M}_a}{\mathcal{M}_v}\Delta\rho_v \tag{1.16}$$

This relation can be substituted in 1.15, thus eliminating the dependence on the density of the air, obtaining a simple equation for the global density.

$$\rho = \rho_0 + \rho_0 \frac{\Delta T}{T_0} + \left(1 - \frac{\mathcal{M}_a}{\mathcal{M}_v}\right) \Delta\rho_v \tag{1.17}$$

At this point one can obtain the buoyancy term B isolating the density ratio of 1.11 from the previous equation.

$$B = \frac{\Delta T}{T_0} + \left(1 - \frac{\mathcal{M}_a}{\mathcal{M}_v}\right) \frac{\Delta\rho_v}{\rho_0} \tag{1.18}$$

1.4 Vapor dynamics

The vapor dynamics is essential to determine a more realistic description of droplets evolution and of the thermodynamics situation.

The domain is composed of two cubic regions: one representing a cloud and the other an air environment. The cloud region is characterized by an initial homogeneous supersaturating condition:

$$\frac{\rho_v}{\rho_{sv}} = 1.02 \tag{1.19}$$

While out of the cloud there is a condition of

$$\frac{\rho_v}{\rho_{sv}} = 0.70 \tag{1.20}$$

That leads to have a non-zero growing factor, mandatory condition for a size of the droplets evolution. Of course the relative humidity will evolve in an inhomogeneous field over time. The vapor balance is regulated by a mass transport law

$$\frac{D\rho_v}{Dt} = D_v \nabla^2 \rho_v - C \tag{1.21}$$

The first term of the right hand side represent the spatial diffusion (D_v is the diffusivity of water vapor), while the second term accounts for the water condensation/vaporative cooling. Note that the coupling with the turbulent field is hidden into the lagrangian derivative term, in particular in the convective component. The condensation term appears also in the temperature balance, it is a source element which takes into account the energy that is released/absorbed due to a droplet growth/decay. The relative humidity field (defined as the ratio between vapor pressure and saturated vapor pressure)

$$\phi(\boldsymbol{x}, t) = \frac{p_v}{p_{sv}}(\boldsymbol{x}, t) \tag{1.22}$$

is determined by solving the vapor balance equation already introduced.

The condensation factor is simply evaluated for every computational volume V with the sum of the growing ratio of the droplets: since the total amount of water must be constant, if the mass of the drops is growing the vapor mass is decreasing and vice versa.

$$C = \frac{1}{V} \sum_k \frac{dm_k}{dt} \tag{1.23}$$

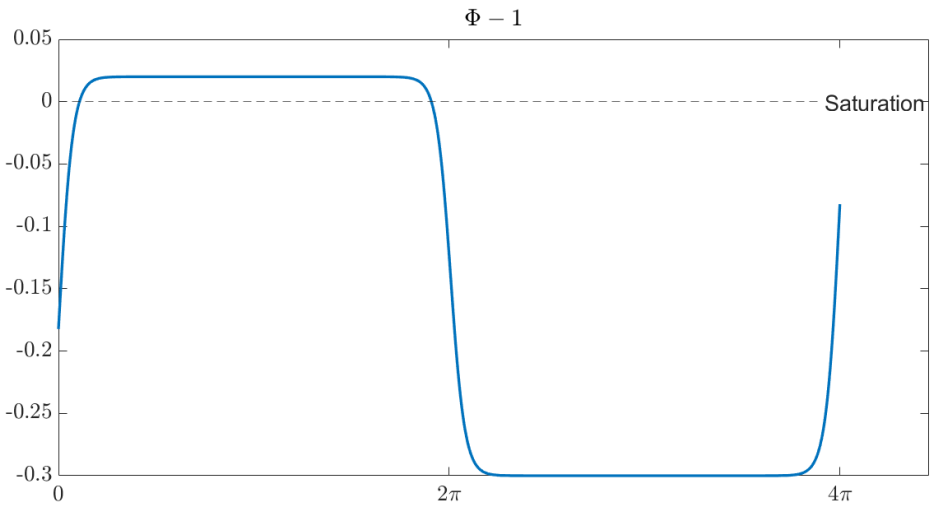

Figure 1.2. Supersaturation initial condition in the domain. Notice that this condition, in addiction to the periodic boundary conditions of the flow, generates two interfaces, at $z = 0 = 4\pi$ and $z = 2\pi$.

1.5 Condensation growth model

The mass of a droplet is the product of the density of water for its volume, so taking into account that the density of the water is constant but the size of the particle varies in an environment like the one we want to study, is possible to introduce the growing ratio: the variation of particles radius in time.

$$\frac{dm}{dt} = \frac{d}{dt}(\rho_w \frac{4}{3}\pi r^3) \Rightarrow \frac{dm}{dt} = \rho_w \frac{4}{3}\pi r^2 \frac{dr}{dt}$$

This variation consists of three contributes (*Ghan et al.* (2011) [5]): the first due to supersaturation S, the second due to the drop curvature ($\propto r^{-1}$) and the last one linked to the solute around which vapor condenses, originating water drops.

$$\frac{dr}{dt} = \frac{C_R}{r}\left(S - \frac{A}{r} + \frac{kr_d^3}{r^3}\right) \tag{1.24}$$

Where

- C_r is the growing factor, it is set as a constant in this numerical analysis. To be honest this factor depends from pressure and temperature, but if the fluxes of heat due to latent heat of evaporation (related to a small variation in droplet temperature) and due to thermal conduction (related to the same temperature variation) are comparable, like in these analysis, its dependence from temperature is negligible [18].
- S is the supersaturation

$$S = \phi - 1 \tag{1.25}$$

- A is a coefficient coming from the Kelvin equation, calculated with the droplets surface tension $\sigma\left[\frac{N}{m}\right]$, it accounts for curvature effects.

$$A = \frac{2\mathcal{M}_w\sigma}{RT\rho_w} \quad [m] \tag{1.26}$$

- k is the hygroscopicity parameter of the solid nuclei around which drops born, it is set according to the job of Saito, Gotoh and Watanabe (2019) [14].
- r_d is the dry radius $[m]$, the radius of solute nuclei around which vapor condenses, originating water drops. Its value is set according to Ovadnevaite *et al.*, 2017 [12]

Parameter	Value	Physical units
$\mathcal{M}_w$	18.02	$[g\,mol^{-1}]$
c_p	1005	$[J\,kg^{-1}K^{-1}]$
D_ν	$2.52 \cdot 10^{-5}$	$[m^2s^{-1}]$
K_a	$2.50 \cdot 10^{-2}$	$[W\,m^{-1}K^{-1}]$
k	0.7	
L	$2.48 \cdot 10^{6}$	$[J\,kg^{-1}]$
A	$1.15 \cdot 10^{-9}$	$[m]$
R	287	$[J\,kg^{-1}K^{-1}]$
σ	$71.97 \cdot 10^{-3}$	$[N\,m^{-1}]$
ρ_a	1.11	$[kg\,m^{-3}]$
ρ_w	1000	$[kg\,m^{-3}]$
r_d	$1 \cdot 10^{-8}$	$[m]$

1.6 Particle dynamics

The particle is a droplet of water studied as a rigid, spherical body on which two forces act: the bouyancy and the aerodynamic drag. So the particle dynamics is described by the following equation

$$m\ddot{\boldsymbol{x}} = \boldsymbol{D} + \boldsymbol{b} \tag{1.27}$$

It is important to underline that in our dynamics are missing some contributions, in order to have a more detailed model one can consult Maxey and Riley (1982)[10].

Aerodynamic drag

We chose to adopt the Stokes drag law for the dynamic of the particles, but one has to satisfy two hypothesis, one on the Reynolds number and the other concerning the laminarity of the flow. The Reynolds number associated to the particle is calculated with the relative velocity between air and drop (here simply called q) and should be less than 1.

$$Re = \frac{q \cdot 2r}{\nu} \sim \frac{q \cdot 10^{-6}}{1.5 \cdot 10^{-5}} < 1 \Leftrightarrow q < 15 \ \ [m/s]$$

if this is verified we have that $Re < 1$. Figures 1.3 shows that during all the time evolution of the simulation the Reynolds number respects the Stokes hypothesis.

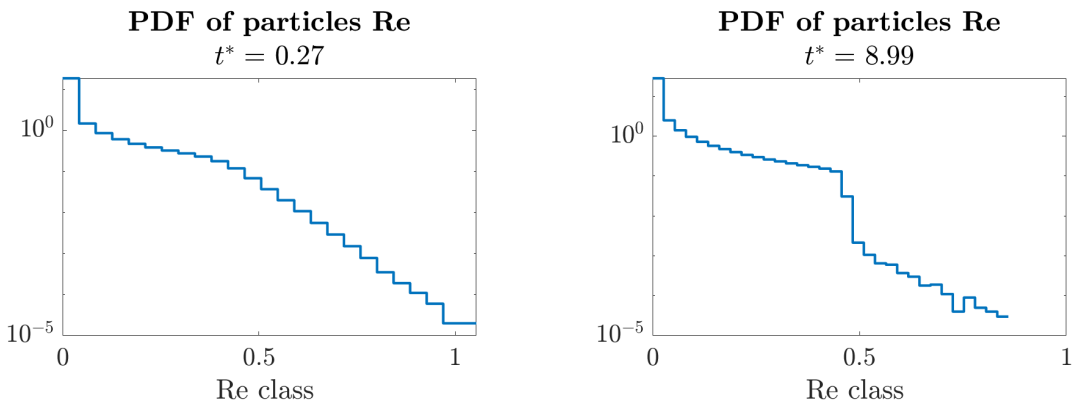

Figure 1.3. Distribution of drops Reynolds numbers in the beginning ($t^* = 0$) and in the end ($t^* = 9$) of the simulation. It is always $Re < 1$ and the portions of particles close to $Re \simeq 1$ have a very low contribution in the distribution: the plot is semi logarithmic in y axis.

In addition one can notice that the Stokes law is valid for laminar flows only, in our simulations the flow is fully turbulent, but the Kolmogorov's length scale is about two order of magnitude bigger than the drops diameter (this will be shown in details in the next chapter). So, since we assume particles as points, the flow around them can be considered laminar. Under these assumptions we adopted the Stokes law as drag model.

$$\boldsymbol{D} = 6\pi\mu r(\dot{\boldsymbol{x}} - \boldsymbol{u}) \tag{1.28}$$

Where

- μ is the air dynamic viscosity $[\frac{kg}{ms}]$
- r is the droplet radius $[m]$
- $(\dot{\boldsymbol{x}} - \boldsymbol{u})$ is the relative velocity of the particle with respect to the fluid $[m/s]$

Particle buoyancy

This contribute is given by the different density of the droplet and the fluid in which is surrounded

$$\boldsymbol{b} = (\rho_p - \rho_f)\boldsymbol{g} \tag{1.29}$$

Law of motion

Substituting 1.28 and 1.29 into the dynamics law, recalling that $m = \rho_p \cdot \frac{4}{3}\pi r^3$ and setting $\rho_f \simeq \rho_a$ the law implemented in the code can be obtained.

$$\ddot{\boldsymbol{x}} = \frac{9}{2}\frac{\rho_a}{\rho_p}\frac{\nu_a}{r^2}(\boldsymbol{u} - \dot{\boldsymbol{x}}) + \left(1 - \frac{\rho_a}{\rho_p}\right)\boldsymbol{g} \tag{1.30}$$

The drag term of this equation hides the relaxation time of the particle τ_p

$$\tau_p = \frac{2}{9}\frac{\rho_p}{\rho_a}\frac{r^2}{\nu_a} \quad [s] \tag{1.31}$$

This time combined with a reference velocity of the turbulent flow U and with the diameter of the particle d_p gives the *local* Stokes number, that estimates the inertial effect on the drop motion.

$$St = \frac{\tau_p U}{d_p} = \frac{\tau_p}{\tau_{flow}} \tag{1.32}$$

For this kind of problems it is usually taken as Stokes number the ratio between particles relaxation time τ_p and Kolmogorov's time scale as the time associated to the flow $\left(\tau_{flow} = \tau_\eta = \sqrt{\frac{\nu}{\eta}}\right)$. This time is characteristic of the smallest eddies in the flow, it means that if is bigger or smaller than τ_p the particles trajectory will be respectively fluid or inertia driven.

$$St = \frac{\tau_p}{\tau_\eta} \tag{1.33}$$

The interpretation of St number is summed up in the following table

St	**description**
«1	The relaxation time of the droplet is much smaller than the fluid's one, so the inertial effects can be neglected and the velocity of the particle will be the same as the fluid one
~ 1	The inertial effects are about the same as those of fluid dynamics
»1	The high inertia of the particle makes it slightly influenced by the fluid dynamics

The diagrams 1.5 show the distributions of Stokes number at the beginning and at the end of simulations in an unstable atmosphere environment. The local St has values much higher than unity, but these are very rare, because they are represented in a semi logarithmic plot. The PDFs of Stokes number computed with τ_η shows that all drops are not inertial driven, this is increasingly true as the simulation progresses and Kolmogorov's time increases. In these picture one can see that there is a jump in the distribution: this is due to the new born by collision particles, that are bigger, but in small number, with respect to the ones injected in the initial distribution.

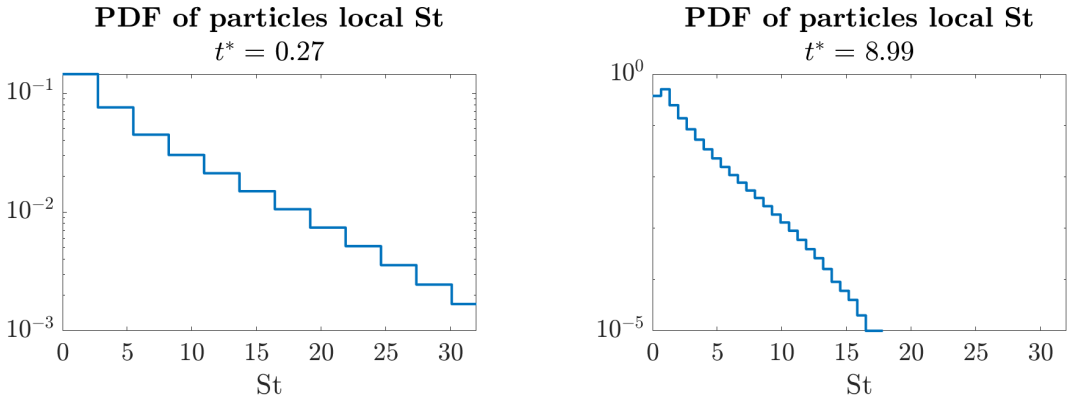

Figure 1.4. PDFs of Stokes numbers computed with the local value of flow velocity. The values $St > 1$ are very unlikely, especially with the evolution of the simulation (t^* is a non dimensional time unit, it will be introduced in a later section).

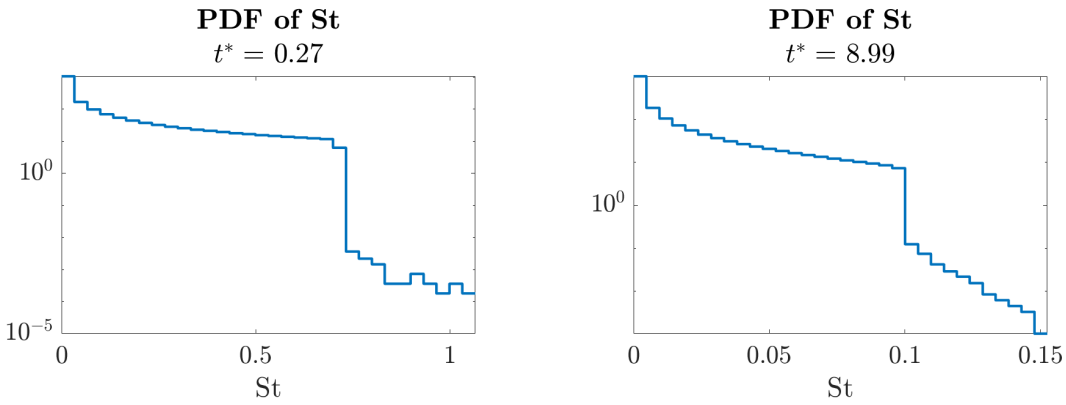

Figure 1.5. PDFs of Stokes numbers computed with the Kolmogorov's time scale, values of St obtained in this way usually are the meaningful ones in droplets dynamics. The jump in the distribution highlights drops born by collision.

Chapter 2

Numerical model

2.1 Discrete approach to the fluid-dynamic problem

The chosen numerical method in DNS code, *DNS_TurIsMI_v141* [7], is pseudo-spectral. A pseudo-spectral method is essentially a numerical decomposition of the Navier-Stokes (incompressible) PDEs rewritten in the Fourier space. The term "pseudo" comes from the fact that the convective term of the equations is solved numerically in the physical space and then re-transformed into the wavenumbers dimensions to proceed in calculations. Instead all the equations describing the particles dynamics and growth are computed in physical space. The time evolution relies on a fourth order explicit Runge-Kutta scheme. The domain is the union of two cubes, usually one representing a portion of cloud and the other representing a region of clear air (however it is possible to change to all cloud or all clear air). Of course the two regions are connected by an interface.

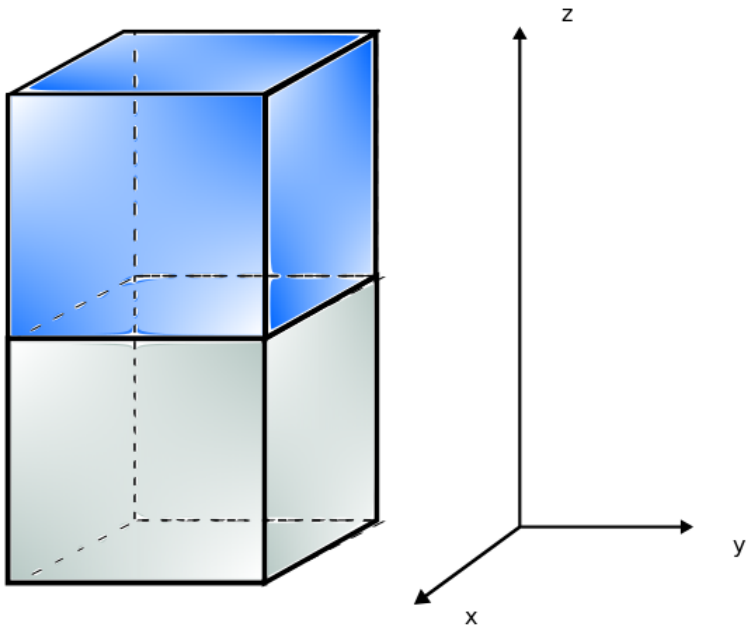

Figure 2.1. Computational domain: is the union of two cubes, one representing the cloudy environment, other the clear air

2.2 Initial conditions

2.2.1 Flow

The initial condition of the flow field is set in order to satisfy the incompressible hypothesis and the shape of a typical turbulent energy spectrum. So the initial flow field is defined as

$$\boldsymbol{u} = \nabla \times \boldsymbol{A} \Rightarrow \nabla \cdot \boldsymbol{u} = 0 \tag{2.1}$$

The Fourier transform of the field $\boldsymbol{A}$ $[m^2/s]$ at the initial time is

$$\boldsymbol{A}(\boldsymbol{x}, t=0) \overset{\text{F.T.}}{\Longrightarrow} \hat{\boldsymbol{A}}(\boldsymbol{k}) = \boldsymbol{\alpha}(\boldsymbol{k})\, e^{i\boldsymbol{k}\xi} \tag{2.2}$$

In this last equation we have that ξ is the phase of the harmonic, and it is randomly chosen in [0,1] (uniform pdf), while $\boldsymbol{\alpha}$ is a three dimensional vector, each component has

a magnitude of

$$\alpha_i = \sqrt{\frac{E(k_i)}{k_i}} \qquad i = \{x, y, z\} \tag{2.3}$$

Where $E(k)$ is the energy spectral density function $[m/s^2]$. The 2.3 derives from the definition of the energy of a signal:

$$\epsilon(\boldsymbol{k}) = \int E(\boldsymbol{k})\, d\boldsymbol{k} = ||\hat{\boldsymbol{u}}(\boldsymbol{k})||^2 \quad \left[\frac{m^2}{s^2}\right] \tag{2.4}$$

Since

$$\epsilon(\boldsymbol{k}) \simeq \sum_j E(\boldsymbol{k}_j)\, \Delta\boldsymbol{k} \tag{2.5}$$

We have

$$||\hat{\boldsymbol{u}}(\boldsymbol{k})||^2 \simeq \sum_j E(\boldsymbol{k}_j)\, \Delta\boldsymbol{k} \tag{2.6}$$

Recalling the definition of 2.1 it is possible to write

$$||\hat{\boldsymbol{u}}(\boldsymbol{k})||^2 = {k_i}^2 {\alpha_i}^2 \tag{2.7}$$

In the end merging the last two relations (with 2.7 written in discrete formulation) we get the 2.3.

The energy density spectrum is computed as an artificial (synthetic) spectrum, in fact it is possible to compute only a portion of a cloud turbulent spectrum (this is due to the lack of computational resources in our actual technological level), in particular we are focused on the last part of the inertial cascade and the dissipation range [4] as represented in 2.2 It is important to notice that the simulation range can not be extended (we can cover 2 or 3 decades in range of wavenumbers, in order to simulate a complete cloud we need 8 decades 2.2) but can be left-shifted in x-direction; doing this one has to be careful that the dissipation will not be included in the simulation and so there will be an accumulation of energy at the highest wave numbers (a slight shift out of the dissipation range can be done without too many consequences, due to the slight numerical dissipation). Back to the artificial energy spectrum, it replies the cloud turbulent one from $\frac{k_0}{2\pi} = 6$ until $\frac{k_{max}}{2\pi} = 169 \simeq 512/3$ with the $-5/3$ power law[1]. It follows a power 2.2 law from $\frac{k_{min}}{2\pi} = 1$ to k_0, for $k > k_{max}$ the spectrum is exponentially decreasing towards $k = 0$, as pointed in figure 2.3.

The flow is characterized by a Reynolds number, it derives from two parameters, one is the dissipation ϵ, that is chosen from known values in literature, the other one is the turbulent macro-scale l, that identifies the typical dimensions of big vortices in turbulence. As already said and showed in fig. 2.2, one can not simulate all the length scales of a cloud, because of lack of computational resources, so knowing the value of Kolmogorov

[1] In order to avoid aliasing issue due to the production of waves with wavelength smaller than the grid resolution, the wave numbers bigger than 1/3 of the biggest possible ($\frac{k}{2\pi} = 512$) are strongly damped

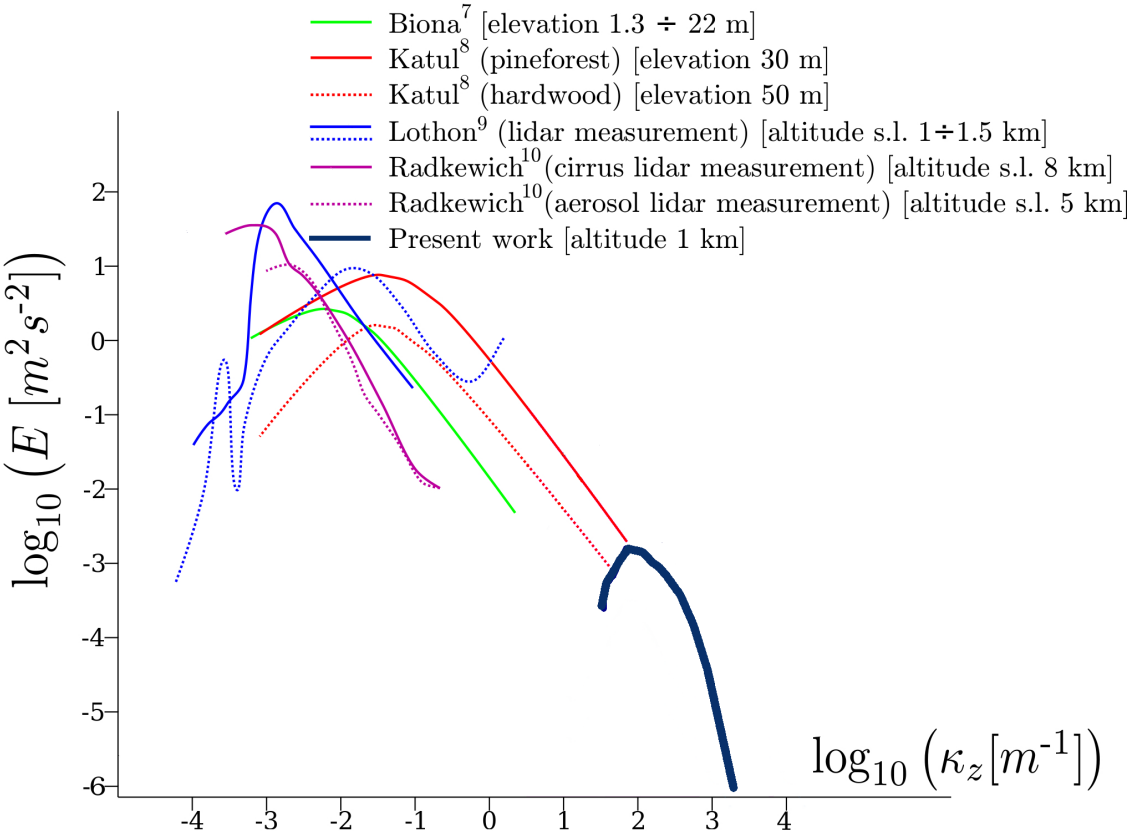

Figure 2.2. Energy density function based on experimental measurements taken from *Gallana, 2014* compared with our job spectrum.

length scale and the number of grid points that can be simulated we can computed the physical length of simulation domain. At this point if we set the wavenumber associated to the macro-scale vortices k_0 we will know the value of l. Once known the value of the dissipation of this kind of cumulus cloud (see Siebert *et al.*, 2006 [15]) and the macro scale, the mean square value of the speed fluctuations can be calculated. With the latter value, the initial Reynolds number associated with the fluctuations can finally be obtained. In our simulations we have initially

$$\left.\begin{array}{l} \epsilon \simeq 600 \ [cm^2/s^3] \\ \nu = 1.57 \cdot 10^{-5} \ [m^2/s] \end{array}\right\} \Rightarrow \eta = \left(\frac{\nu^3}{\epsilon}\right)^{1/4} \simeq 5 \cdot 10^{-4} \ [m]$$

Since the turbulence is decaying η will increase in time, and so a good trade between computational resources and physical accuracy is to set a grid of $1024 \times 512 \times 512$ points, with a spacing of $\Delta x = 1\, mm$. So we have

$$L = 512 \cdot \Delta x = 0.512 \ [m]$$

In the end we can compute the velocity root mean square fluctuation and the Reynolds

number

$$\left.\begin{array}{l}\epsilon \simeq 600\ [cm^2/s^3] \\ l \sim \frac{L}{k_0} = \frac{0.512}{6} \simeq 8.53 \cdot 10^{-2}\ [m]\end{array}\right\} \Rightarrow u'_{rms} = \sqrt[3]{l\epsilon} \simeq 1.5 \cdot 10^{-1}\ [m/s]$$

$$Re_l = \frac{u'_{rms} l}{\nu} \simeq 820$$

For completeness we also report the Reynolds number calculated with the Taylor micro scale λ

$$\lambda = \sqrt{\frac{15\nu}{\epsilon}} \cdot u'_{rms} \simeq 1.15 \cdot 10^{-2}\ [m]$$

$$Re_\lambda = \frac{\lambda u'_{rms}}{\nu} \simeq 110$$

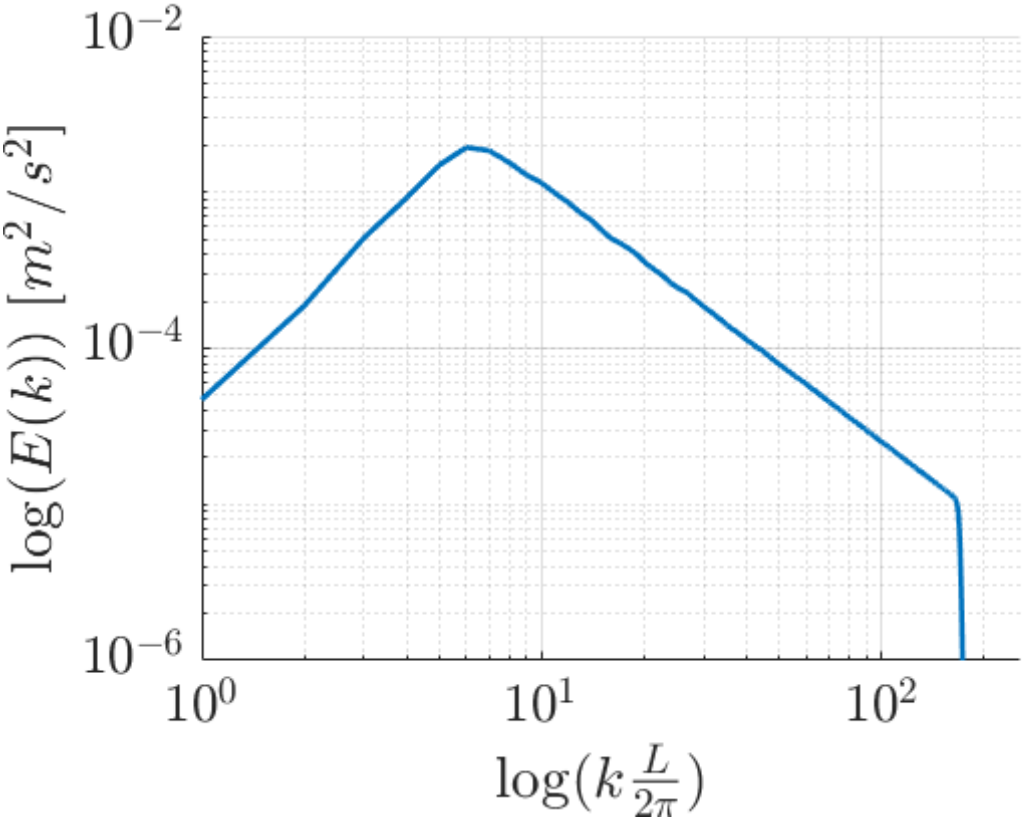

Figure 2.3. Initial energy spectrum associated to one velocity component u'^2

2.2.2 Particles

The liquid phase is distributed in the cloud region, in the form of drops of different size, with the constraint that the total liquid water content is fixed to $8 \cdot 10^{-4}[g/m^3]$, a common

value found in cumulus clouds (Siebert *et al.*,2006 [15]). The initial population of droplets is set in a way that every class of volume (or radius) has the same fraction of liquid water. As will be shown later turbulence dramatically affects the kernel statistics, providing a widely non uniform number of collisions with respect to the radius classes.

2.3 Boundary conditions

Along all three spatial direction are set periodic conditions at the boundaries of the domain: this is mandatory in order to apply a pseudo-spectral discrete method that describe a flow. The droplets are also subject to periodic boundary conditions, except for the lower wall of the domain: particles crossing it are removed, in order to simulate a sedimentation effect.

Chapter 3

Droplet collisions

The collision term is fundamental to describe the life of a population of particles, in particular the purpose of this work is to describe collisions of droplets population in cloud. In order to do so it is fundamental to introduce the collision kernel Γ. This element, multiplied by the numerical volumic density of two family of particles, provides the collision rate (collision per seconds) between the two species. Usually the **population balance equation** (PBE) is the partial differential equation that aim to model the life of a particles population. In this differential equation the collision term is the core of the aggregation term, that acts in the equation as a source element. Introducing $N_i \equiv N(r_i)$, the total number of droplets of the population with radius r_i, and $n_i \equiv N_i/\Delta V$, the volumic density of particle of radius r_i in the population, one can write a PBE where the growth of N is due only to collisions, this is the **Smoluchowski equation** [16], which applies to collisions in which the mass is kept (as for colliding droplets in clouds).

$$\frac{dn_i}{dt} = \frac{1}{2}\sum_{j=1}^{i-1}\Gamma_{i,i-j}n_j n_{i-j} - n_i\sum_{j=1}^{\infty}\Gamma_{i,j}n_j \tag{3.1}$$

Where the first right hand side term describe the increase of particles by collision, the second one accounts for the particles that colliding disappear from their population classes (they merge to create a new drop which belongs to a class different from the two starting ones).

In literature there is a wide list of possible models, each one based on different hypothesis, to describe the kernel. A milestone model is the Saffman and Turner collision kernel [13]. It is now briefly reported, the detailed discussion is given in the appendix. They assume the droplet momentum equation as:

$$\dot{\mathbf{c}} = \underbrace{\frac{9}{2}\frac{\rho_a}{\rho_p}\frac{\nu_a}{r^2}(\mathbf{u}-\mathbf{c})}_{\text{Stokes drag}} + \underbrace{\left(1-\frac{\rho_a}{\rho_p}\right)\mathbf{g}}_{\text{Gravity}} + \underbrace{\frac{\rho_a}{\rho_p}\dot{\mathbf{u}}}_{\text{Added mass effect}} \tag{3.2}$$

Where $\mathbf{c}$ is the absolute velocity vector of the droplet and $\mathbf{u}$ is the local flow field velocity vector. Hence they derived the following expression for the collision kernel in homogeneous, isotropic and statistically steady turbulence (their model is valid only for colliding particles

that have radii ratio lower than 2).

$$\mathbf{\Gamma} = 2\sqrt{2\pi}R^2 \left[\left(1 - \frac{\rho_a}{\rho_p}\right)^2 (\tau_2 - \tau_1)^2 \overline{\left(\frac{D\mathbf{u}}{Dt}\right)^2} + \frac{1}{3}\left(1 - \frac{\rho_a}{\rho_p}\right)^2 (\tau_2 - \tau_1)^2 \mathbf{g}^2 + R^2 \frac{\epsilon}{9\nu} \right]^{\frac{1}{2}} \tag{3.3}$$

Where

- $\tau = \frac{2}{9}\frac{\rho_p}{\rho_a}\frac{r^2}{\nu}$ is the relaxation time of the drop.
- $R = r_1 + r_2$ is the sum of the radii of colliding drops.
- $\epsilon = \partial E/\partial t$ is the dissipation of turbulent kinetic energy, and it is set as a constant parameter.

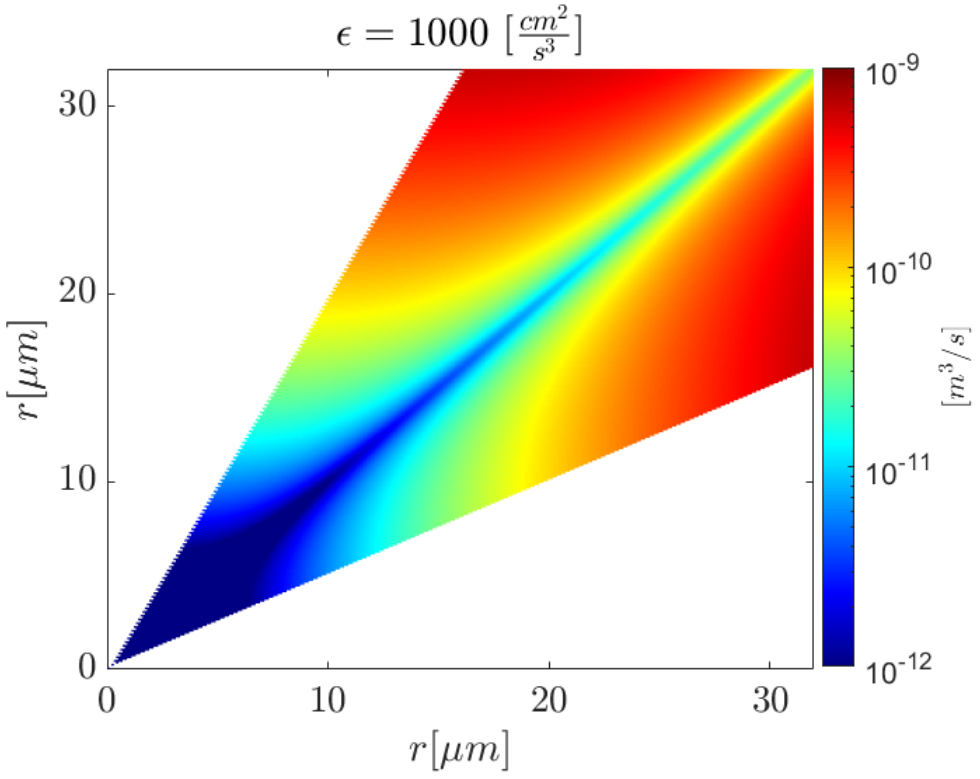

Figure 3.1. Saffman and Turner collision kernel, the limits on radius ratio does not allow to have information about some areas of the kernel. From this picture is evident that the collision involving the biggest particles are the most likely to happen. One can also notice the low rate of collision between equal droplets, this happens because they have same inertia and as a consequence they will evolve following in the same way the streamlines. Since streamlines do not cross, drops will tend to not cross their trajectories.

The model adopted in the simulations is not fitting the hypothesis of statistically steady turbulence, so this analytical formulation is not suitable to

predict our results. However it will be interesting to compare it with our kernels, as if they were a sequence of steady states, in order to see where are the main differences. So, recalling that we do not implement the *added mass effect*, the 3.3 reduces to:

$$\mathbf{\Gamma} = \frac{2\sqrt{2\pi}}{3} R^2 \left[3 \left(1 - \frac{\rho_a}{\rho_p} \right)^2 (\tau_2 - \tau_1)^2 \mathbf{g}^2 + R^2 \frac{\epsilon}{\nu} \right]^{\frac{1}{2}} \tag{3.4}$$

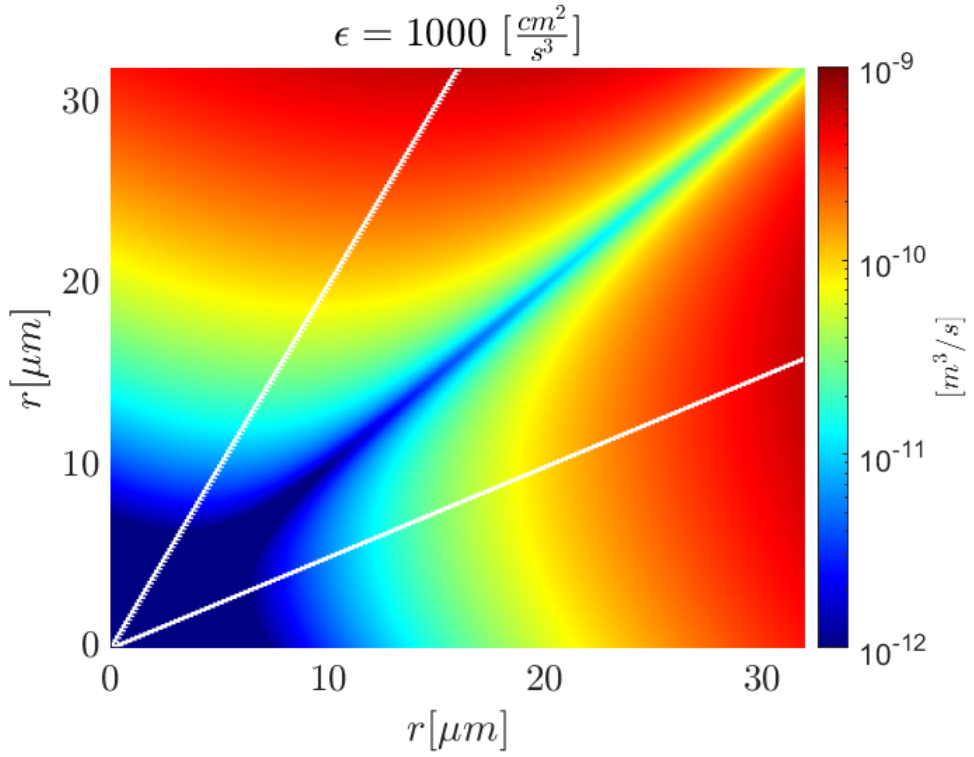

Figure 3.2. Collision kernel for the reduced model (3.4). In this picture the analytical equation has been extended outside the radii ratio limit (highlighted from the two white lines). This extension is done because it has been noticed, that for some analyzes, the pattern emerged was close the one described by Saffman and Turner, even outside this radii ratio limit.

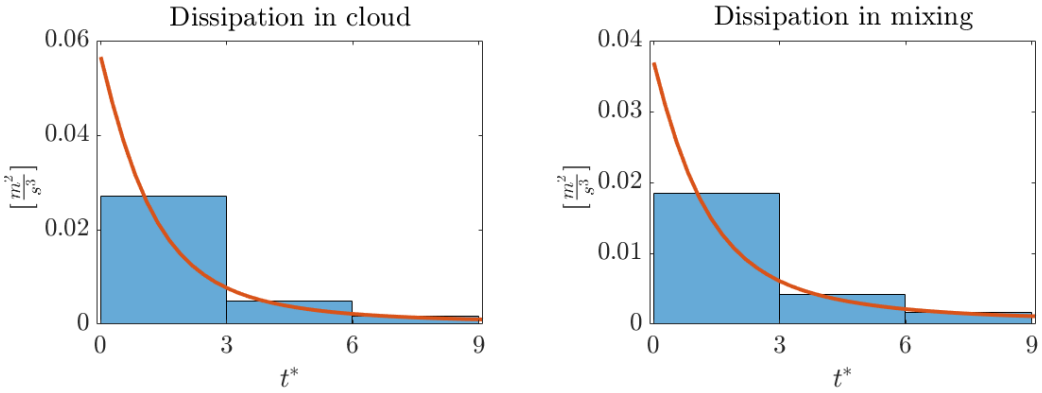

Figure 3.3. Dissipation time evolution in our simulations: the initial value in the cloud is set according to the measurements provided by Siebert *et al.* [15]. The red line is the dissipation $\epsilon(t^*)$, measured into the simulation. the blue columns are dissipation integral mean values, they will be used for computing the reduced model kernels that will be compared with the numerical results. It has been verified that the curve is fitting the $(t^*)^{-2}$ time evolution, as usual for decaying turbulence. The details about the time unit t^*, that represents the time referring to the initial eddy turnover time, are given in section 3.1.1.

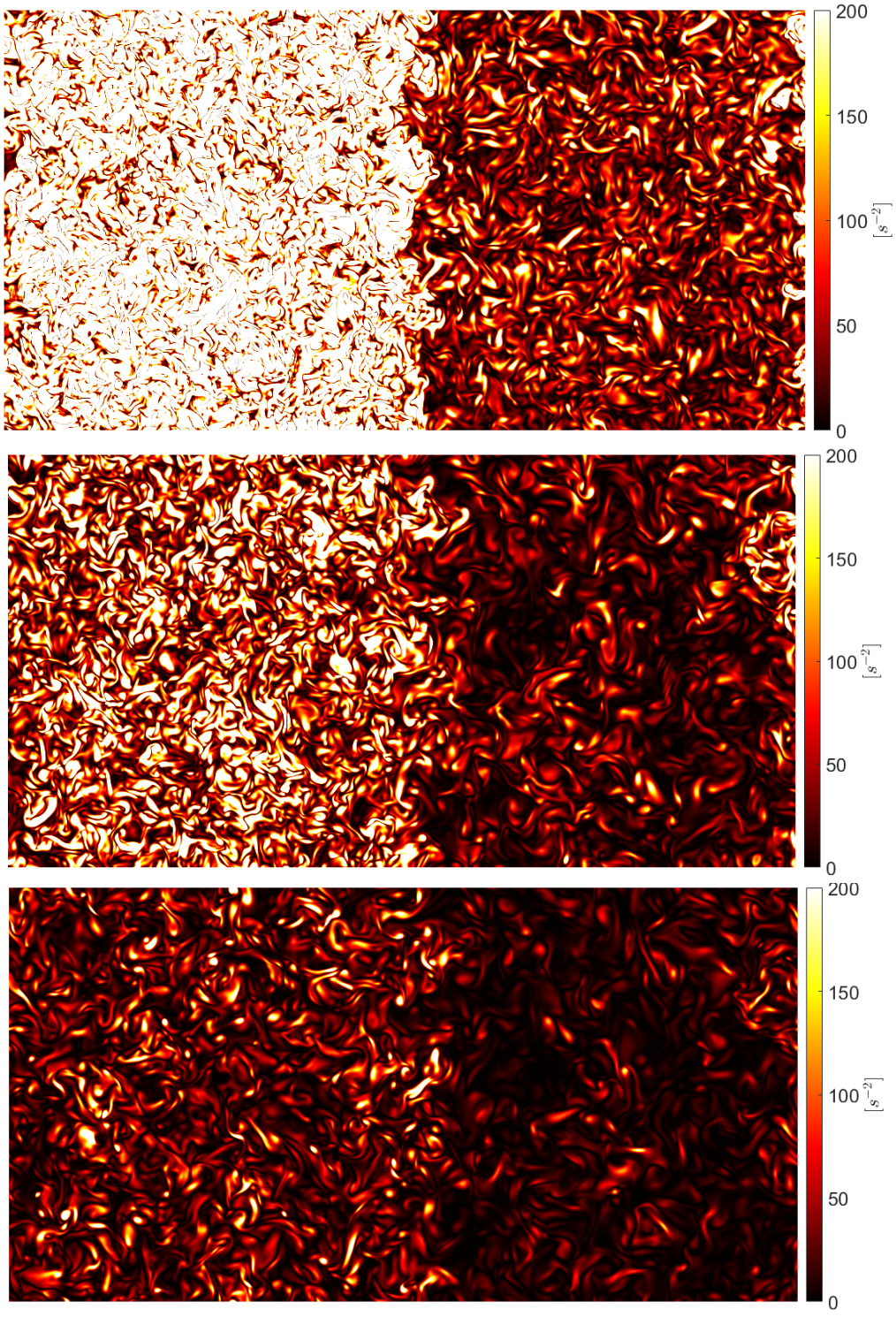

Figure 3.4. Decaying of enstrophy field: the picture shows the enstrophy after 0.3,3,6 time scales all over the domain. It is clear that we are not in a forced turbulent environment. The regions of cloud (more energetic, on the left hand side) and clear air are clearly distinguishable.

3.1 Kernel discrete evaluation

The collision mechanism is based on the idea that if two objects lie below a certain distance, they merge (every collision is detected when the distance between centers of droplets is less or equal than the sum of their radii, the collision efficiency is equal to 1): this way to compute it let us define our kernel as a **turbulent geometric collision kernel**.

Water drops in our simulations have initially characteristic dimension of $0.6 \div 30\ \mu m$, so they are represented as rigid spheres in good approximation. In each time step an algorithm looks for every collision, merges the two colliding droplets into a new one and interpolates its data (position,velocity,..) from its 'parents' data. The information about every collision are stored, so it is possible to compute some statistics, like the collision kernel. The kernel is essentially a matrix that given as an input (multiplied) two population densities gives back as result the collision rate between them, or, from another point of view, it highlights the probability of a collision between two particles of a given radius class. The discrete kernel is computed as the number of collision between two radius classes $(\Delta r_1, \Delta r_2)$ occurred between time t and $t + \Delta t$ divided by the two mean classes population in Δt. This ratio is multiplied by the volume in which the particles are enclosed and divided by the time in which collision are counted.

$$< \mathbf{\Gamma}(\Delta r_1, \Delta r_2) >_{t,t+\Delta t} = \frac{[N_{coll}(\Delta r_1, \Delta r_2)]_{t,t+\Delta t}}{< N_1 >_{t,t+\Delta t} < N_2 >_{t,t+\Delta t}} \cdot \frac{\Delta V}{\Delta t} \quad \left[\frac{m^3}{s}\right] \tag{3.5}$$

In the previous equation the symbol $< . >_{t,t+\Delta t}$ represents temporal bins. Note that it is necessary to introduce the ΔV factor because N is a dimensionless counter $[\#]$, while $\dot{n}, n$ are defined as numbers per unit of volume $[\#/m^3]$.

$$\left[\dot{n} = \frac{Ncoll}{\Delta V \Delta t};\ n_i = \frac{N_i}{\Delta V}\right] \Rightarrow \mathbf{\Gamma} = \frac{\dot{n}_{12}}{n_1 n_2} = \frac{N_{coll}}{N_1 N_2} \cdot \frac{\Delta V}{\Delta t} \tag{3.6}$$

It can be noticed that the analytical kernel is not a function of a time interval, but it is continuous in time; the same thing is observed in the radius dependence. The ideal numerical experiment is is such that $\Delta t, \Delta r \to 0$.

$$\mathbf{\Gamma}(r_1, r_2, t) = \lim_{\Delta t, \Delta r \to 0} < \mathbf{\Gamma}(\Delta r_1, \Delta r_2) >_{t,t+\Delta t} \tag{3.7}$$

3.1.1 Time measurement

In this kind of analysis it is common to refer at a dimensionless time unit, the eddy turnover time (ETT). An ETT physically represents the reference time of turbulent macro scale vortexes. Since turbulence is decaying ETT changes in time, so we will refer to the initial one (τ_0). This ETT can be computed as the ratio between turbulence macro scale l and velocity fluctuations in root mean square u'_{rms}. In these simulation we have

$$\tau_0 = \left(\frac{l}{u'_{rms}}\right)_0 \simeq 0.5\ \ [s] \tag{3.8}$$

So we define the dimensionless time as

$$t^* = \frac{t}{\tau_0} \tag{3.9}$$

3.1.2 Time averaging

It is very important to underline that **the temporal mean value must not be considered instead of the ensemble averages**, because the flow is in transient condition and mediating in time means to remove all information about the evolution. The matter is that since we are in a discrete problem we can not provide a continuous solution, in addition making ensemble averages is very expensive from a computational resources point of view, because it requires to do the same simulation many times changing the initial condition. So we decided to calculate kernels over time, taking collisions that happen in a Δt as small as possible, but which still provide statistically acceptable results. The optimal trade between a reasonable computational resources consumption and physical accuracy led to set $\Delta t^* = 3 \Rightarrow \Delta t \simeq 1.5\, s$, but for some analyzes we have lowered this threshold to $\Delta t^* = 0.8 \Rightarrow \Delta t \simeq 0.4\, s$.

3.1.3 Δr adopted

Select Δr is equivalent to set the number of classes in which the collision kernel will be computed, so the choose of Δr is a trade off between the accuracy of the results that one has to provide and their completeness. As stated in section 3.1, the ideal results are those for $\Delta t, \Delta r \to 0$, but since we are running a numerical analysis is impossible to provide such a result. One can notice that the number of classes is influencing the result, that is not converging to an asymptotic one changing the number of bins. The following pictures report the collision kernels computed for the same simulation using different number of bins, highlighting how an higher resolution kernel (large number of bins adopted) inevitably invalidates the completeness of the pattern, while a low resolution kernel leads to low detailed, coarse results. In order to have complete and detailed collision kernels one should have large computational resources and run several more simulation to compute the ensemble averages. The data here provided comes from an ensemble average made of three simulations. One can see that increasing Δr the magnitude of kernel cells is increasing too; this happens because in this way there is a restriction in the population number (n_i, n_j) used to compute the collision kernel. Simply looking at the way in which we compute the kernel (3.6) one can notice that a decrease of n_i, n_j leads to an increase of Γ_{ij}.

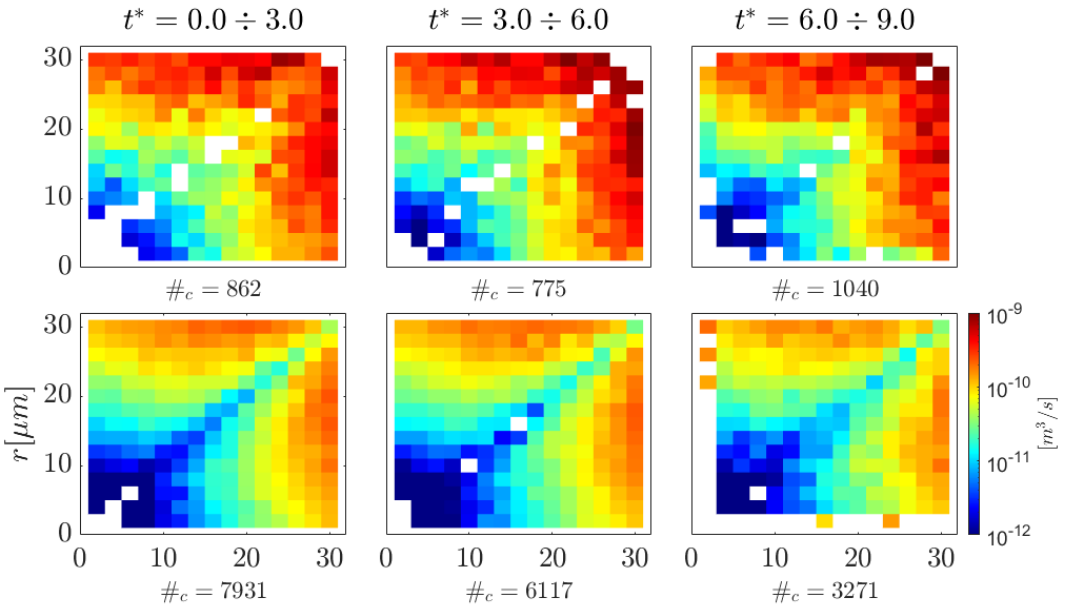

Figure 3.5. These are the measured collision kernel in mixing environment (first row) and homogeneous cloud (second row) for the three ensemble averages of the polydisperse, unstable simulation. All the details and the meaning of this pictures will be explained in the dedicated section (figure 5.3). At the moment the important thing is to notice how the results are changing with the number of bins. This picture is made with 16 bins, that is $\Delta r = 2\mu m$.

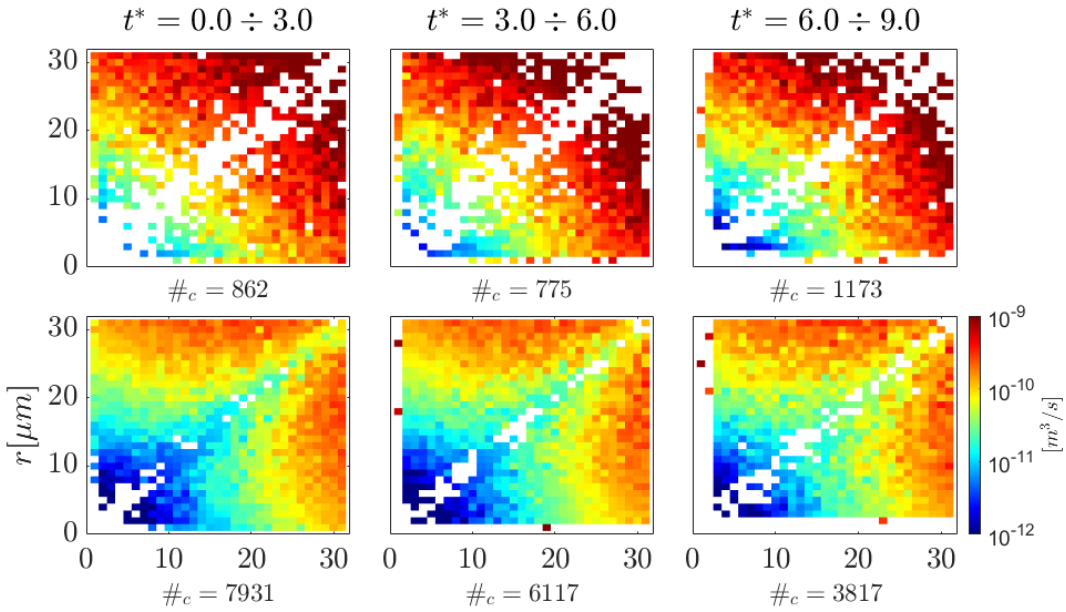

Figure 3.6. This picture is made with 32 bins, that is $\Delta r = 1\mu m$.

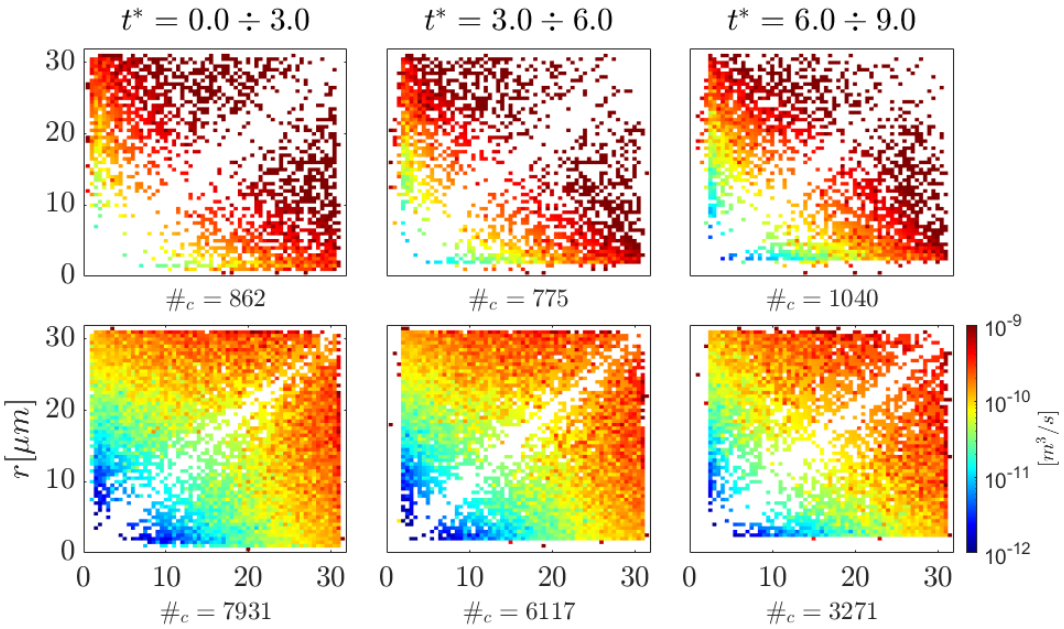

Figure 3.7. This picture is made with 64 bins, that is $\Delta r = 0.5\mu m$.

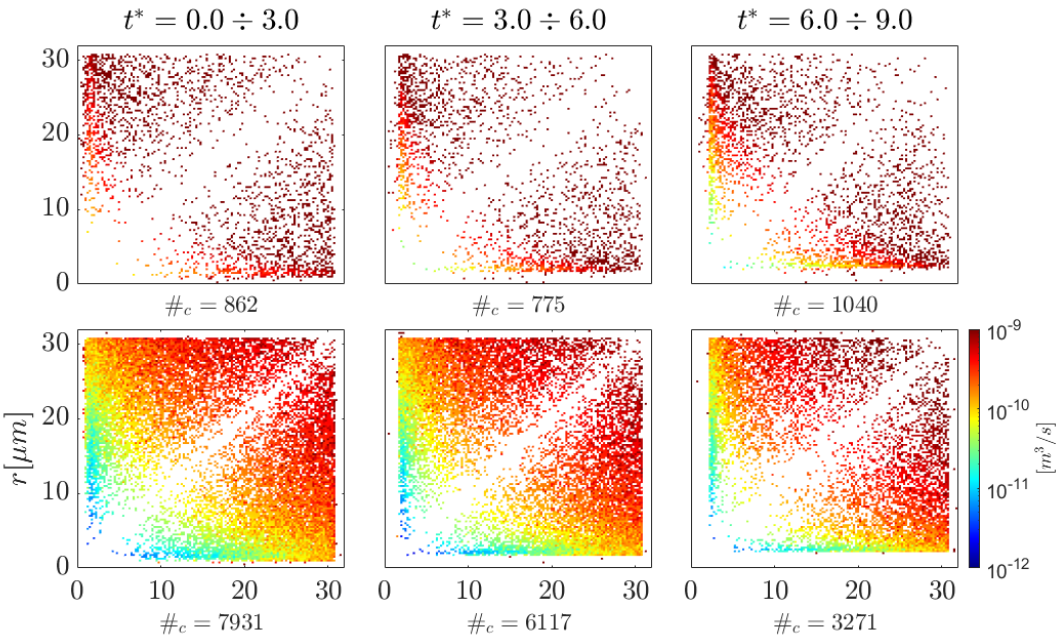

Figure 3.8. This picture is made with 128 bins, that is $\Delta r = 0.25\mu m$. It is important ot notice how different it appears with respect to the figure with $\Delta r \simeq 2\mu m$, in particular one can observe an overall increase in magnitude.

Chapter 4

Analysis of collision kernel in HIT cloud portion

Before studying an anisotropic environment as a cloud/clear-air mixing it is better to understand what happens in a simple environment: an homogeneous isotropic turbulent (HIT) flow representing the core of a cloud. This is the closest model to the supposed one by Saffman and Turner, so it will be important as a benchmark for the analytical formulation but also to have a sample to be compared with more complex simulations, in order to be able to distinguish the effects related to anisotropy.

4.1 Homogeneous cloud

In this section are provided the results of a simulation in full cloudy environment: 20 millions of water droplets, with initial diameter in the range of $0.6 \div 30\,\mu m$ are dispersed homogeneously in a domain of $1.024\,m \times 0.512\,m \times 0.512\,m$. The DNS is computed for a decaying turbulent flow with a grid resolution of 1 point every mm. The environment is saturated (100% RH) and there is not a temperature gradient, so it is set $T_0 = 281\,K$. This is our reference simulation for the collision kernel in a cloudy environment. The richness of drops in this simulation generates a large number of collision, that provides a good statistics and shows in a very clear way the time evolution of the collision kernel.

Figures 4.1 and 4.2 report the numerical results. It can be seen that the most probable collisions regard medium/big size particles (high magnitude), while small particles tend to not collide with other small particles, in fact the cells referring to these collisions (down left corner) are four order of magnitude weaker than the ones referring to big drops collisions. The fact that rarely were recorded collisions between equals droplet can be explained recalling that when particles have same inertia they follow in the same way the streamlines, so since streamlines do not cross each others, drops will not too. Time history shows that the unsteady conditions slightly affects the structure and magnitude of the kernel. Looking at the comparison with Saffman and Turner model, that is **not intended** for this kind of simulations, there are two main differences:

- The analytical model overestimates the magnitude of kernel.

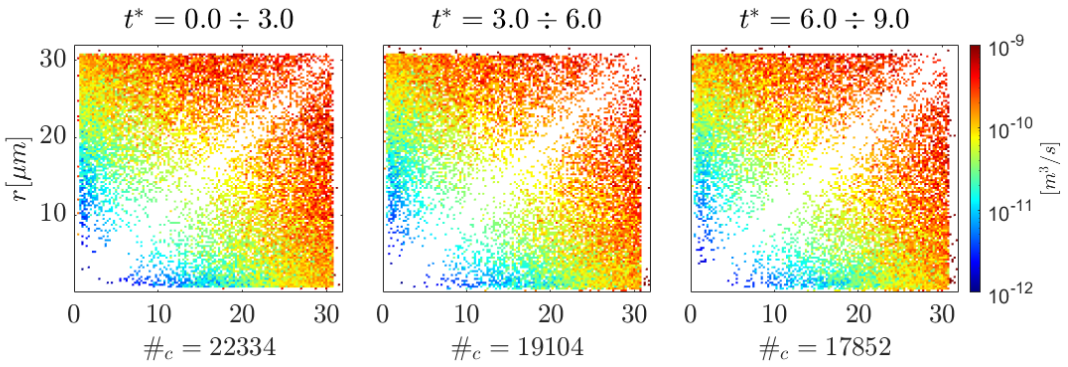

Figure 4.1. Measured states of collision kernel $\left[m^3/s\right]$ with a bin spacing $\Delta r \simeq 0.25\mu m$, corresponding to 128 bins for both kernel x, y coordinates. The dissipation of turbulent kinetic energy decays from an initial value $\epsilon \sim 800\, cm^2/s^3$ with a $(t^*)^{-2}$ time dependence. The values associated to every kernel are respectively the mean ones in the Δt^*, so $\epsilon \sim 300$,50,15 cm^2/s^3 as reported in fig.4.4. The value $\#_c$ is the number of detected collisions in the period of time in which kernel is evaluated.

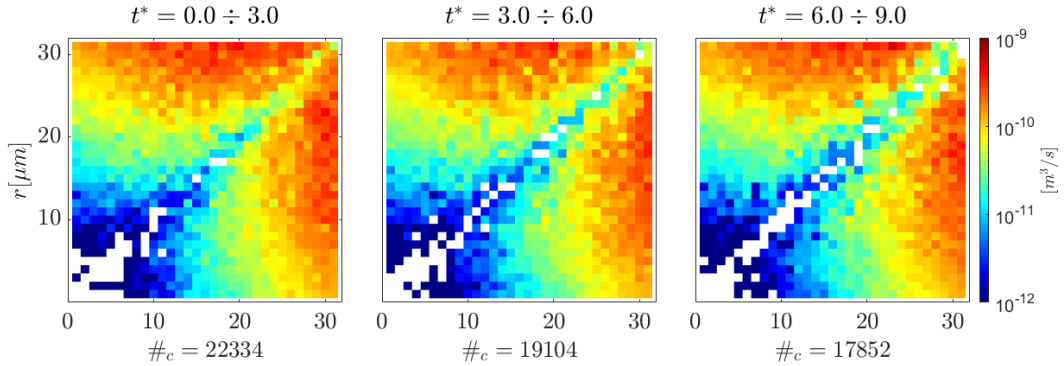

Figure 4.2. Measured states of collision kernel $\left[m^3/s\right]$ with a **coarser** bin spacing $\Delta r = 1\mu m$, corresponding to 32 bins for both kernel x, y coordinates. The dissipation of turbulent kinetic energy and the values associated to every kernel are respectively the same as the previous representation.

- There is a spreading in the *non-colliding* diagonal terms.

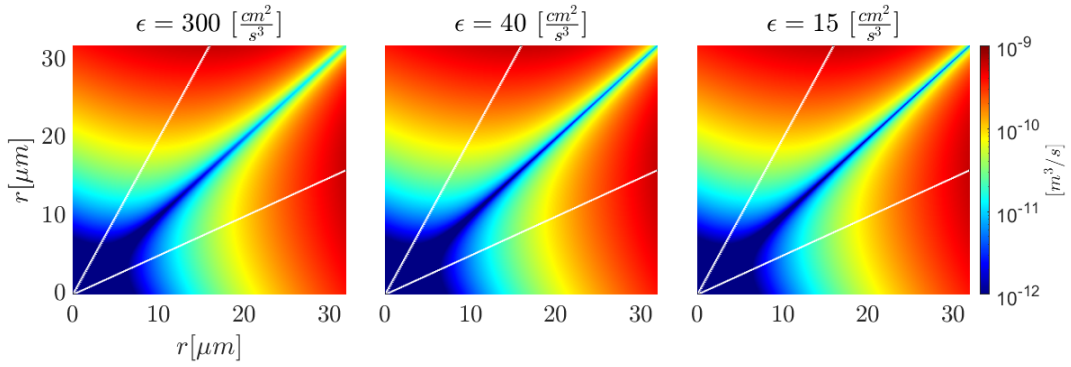

Figure 4.3. Analytical time evolution of collision kernel $[m^3/s]$ from Saffman and Turner formulation, one has to notice that the "lobes" pattern appears also in the numerical measurements, even if **Saffman and Turner model is not intended for this kind of simulations**. Notice also that the decrease of kinetic energy is not affecting the wideness of the diagonal but only its magnitude.

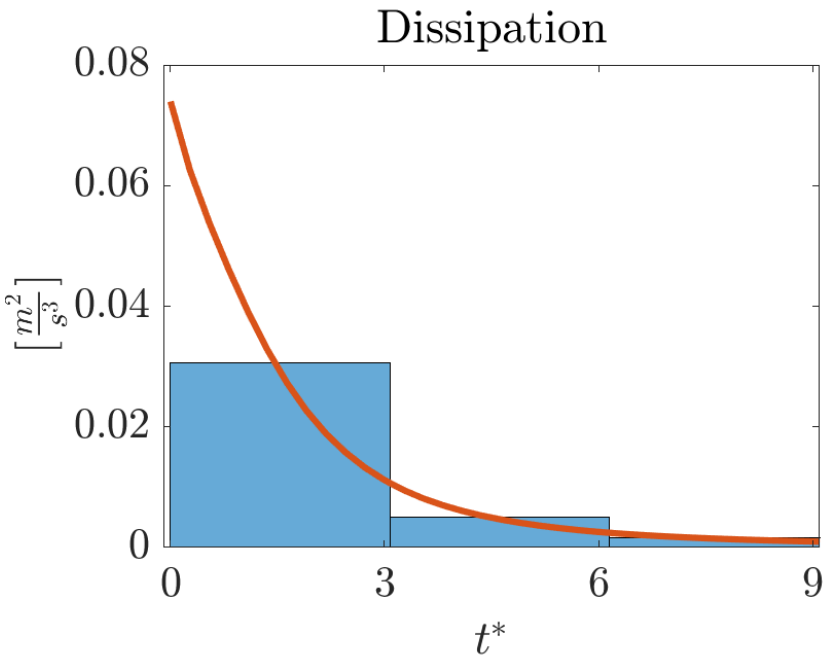

Figure 4.4. Dissipation of turbulent kinetic energy associated to this simulation. The blue columns are mean integral values adopted to compute the associated Saffman and Turner kernels.

The difference between Saffman and Turner model (Γ_a) and the numerical results (Γ_s)

has been computed as the following

$$e\left(r_1, r_2\right) = \frac{\Gamma_s\left(r_1, r_2\right) - \Gamma_a\left(r_1, r_2\right)}{\Gamma_s\left(r_1, r_2\right)} \tag{4.1}$$

In this way we will obtain

$$\begin{aligned}
&e = 0 \Leftrightarrow \Gamma_s\left(r_1, r_2\right) = \Gamma_a\left(r_1, r_2\right) \\
&e = 1 \Leftrightarrow \Gamma_s\left(r_1, r_2\right) >> \Gamma_a\left(r_1, r_2\right) \\
&e = -1 \Leftrightarrow \Gamma_a\left(r_1, r_2\right) = 2 \cdot \Gamma_s\left(r_1, r_2\right) \\
&e < -1 \Leftrightarrow \Gamma_a\left(r_1, r_2\right) >> \Gamma_s\left(r_1, r_2\right)
\end{aligned}$$

The results are shown in fig.4.5 and it is clear that the Saffman and Turner reduced model is not adapt to describe our system, it overestimates the collision rate almost uniformly (mostly true for 32 bins result). The uniformity of the error is consistent with the fact that the analytical pattern (but not the magnitude) looks similar to the one found in numerical measurements. As already said this fact is increasingly true for the 32 bins analysis.
But one should be aware that the **Saffman and Turner model is not intended for this kind of simulations**.
Table resumes the average relative error in time for both the 32 and 128 bins.

t^*	$0 \div 3$	$3 \div 6$	$6 \div 9$
32 bins error	-75%	-100%	-100%
128 bins error	-75%	-75%	-75%

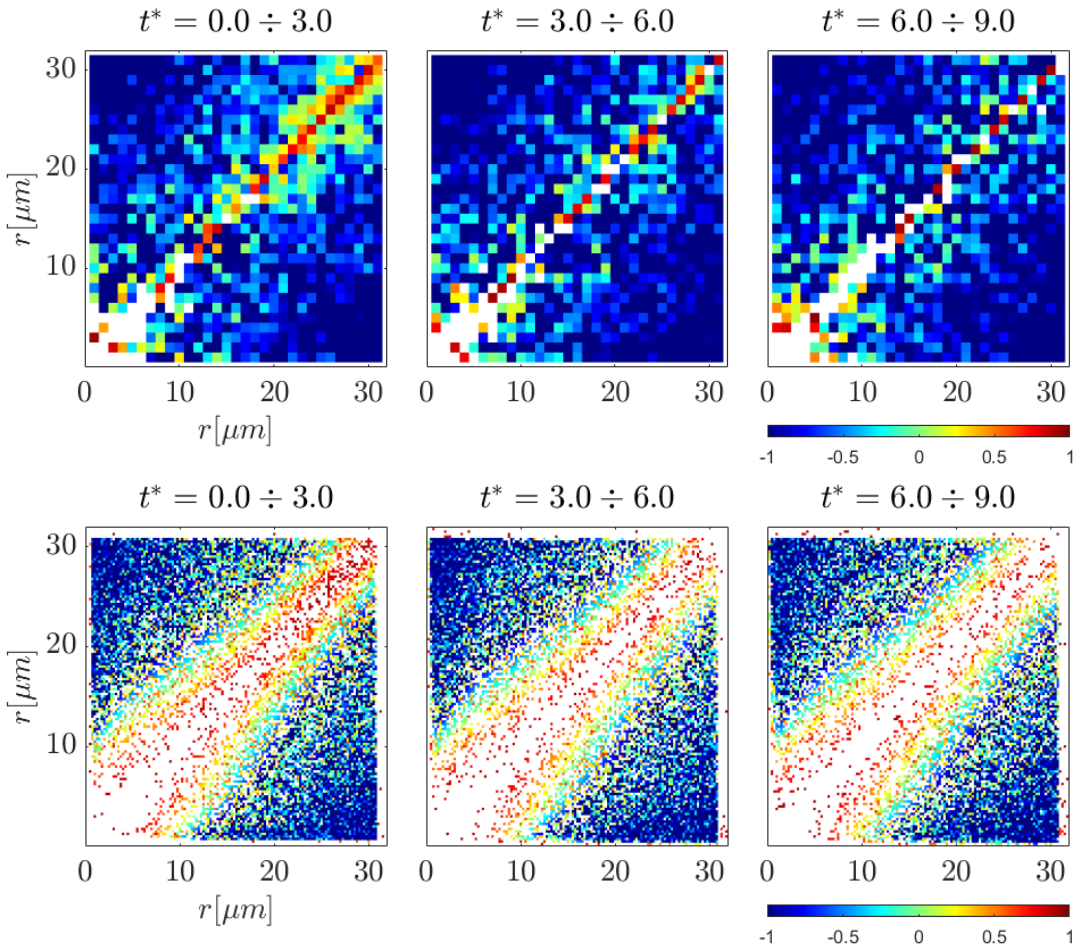

Figure 4.5. Relative error between the results obtained with Saffman and Turner reduced model and numerical results, limited between $e = \pm 1$. The first row refers to 32 bins results, the second one to 128 bins. Again one has to remember that **Saffman and Turner model is not intended for this kind of simulations** and this comparison helps to spot the main differences with the numerical results. The areas where the error is uniform highlights where the numerical results follow the pattern described by Saffman and Turner.

Chapter 5

Analysis of collision kernel in cloud/clear-air environment

In this chapter are provided the results of the simulation for a stable, unstable and neutral stratified flow, where a cloud interfaces in the upper part with clear air. Initially there are ~ 10 millions of water droplets, with diameters in the range of $0.6 \div 30\,\mu m$, that are dispersed homogeneously in the cloud region, that has a volume of $0.512^3\,m^3$. The DNS is computed with a grid resolution of 1 point every mm. The environment is over saturated (102% RH) in the cloud and under saturated (70% RH) in the remaining domain ($0.512^3\,m^3$ of clear air). The stability is due to the temperature initial condition (see fig. 1.1). The two portion of the domain are characterized by different kinetic energy associated to velocity fluctuations: cloud has ~ 6.6 times the kinetic energy associated to the fluctuations than clear air. All the simulations ran for the equivalent of nine initial eddy turnover time and the reason why we choose this time length is mainly due to energy decay, but also to the limits imposed by the high computational resources request for this kind of simulations.

Turbulent shearless mixing

A turbulent shearless[1] mixing area is formed at the interface between cloud and clear air, this region is widening in time, as already described by Tordella and Iovieno (2011) [8]. We are interested in measuring collisions there and compare them with measured ones in the homogeneous environment, in the cloud portion. It is important to notice that because of the periodic boundary conditions there is a mixing layer also under the cloud. It can be treated as an artificial mixing condition because there is a temperature jump (discontinuity due to periodic boundary) of $\pm 2\,K$, and it will be less physical and statistical accurate because particles crossing the lower boundary of the domain are removed. It is important to know how it is defined a turbulent mixing region and how it evolves in time, in order to analyze the collision kernel in this area. Referring to Tordella and Iovieno (2011) [8], since the anisotropic direction is only one (precisely the z coordinate), mixing wideness

[1]The two portions of the domain have null mean velocity, there is not relative motion between them.

Figure 5.1. Cloud and clear air represented by relative humidity (or saturation level), white is for $RH = 1.02$, while blue stays for $RH = 0.7$. In particular this image refers to $t^* = 4$, where the kinetic energy associated to fluctuations is $(u'_{rms})^2 = 0.0075\ \left[m^2/s^2\right]$.

is characterized by only one length. Calling $E_{1,2}$ the turbulent kinetic energy in the two fields (1,2) the mixing length Δ satisfies:

$$\Delta: \ 0.25 < \frac{E_2 - E\,(z)}{E_2 - E_1} < 0.75 \tag{5.1}$$

Some of the values that we measured has been reported in tab. 5.1 and compared with the power law found by Tordella and Iovieno for a non stratified flow. Globally we found that

t^*	**Power law** Δ/Δ_0	**Measured** Δ/Δ_0
3	1.66	1.67
6	2.28	2.00
9	2.75	2.47

Table 5.1. The table reports samples of the wideness of mixing region referred to the initial one. Left column contains the predictions of power law, the right one the unstable simulation measurements.

the mixing, in these conditions of unstable stratification, grows coherently with the power law. For all the following analysis (for neutral and stable stratification) the procedure in order to find the mixing region has been direct measurement.

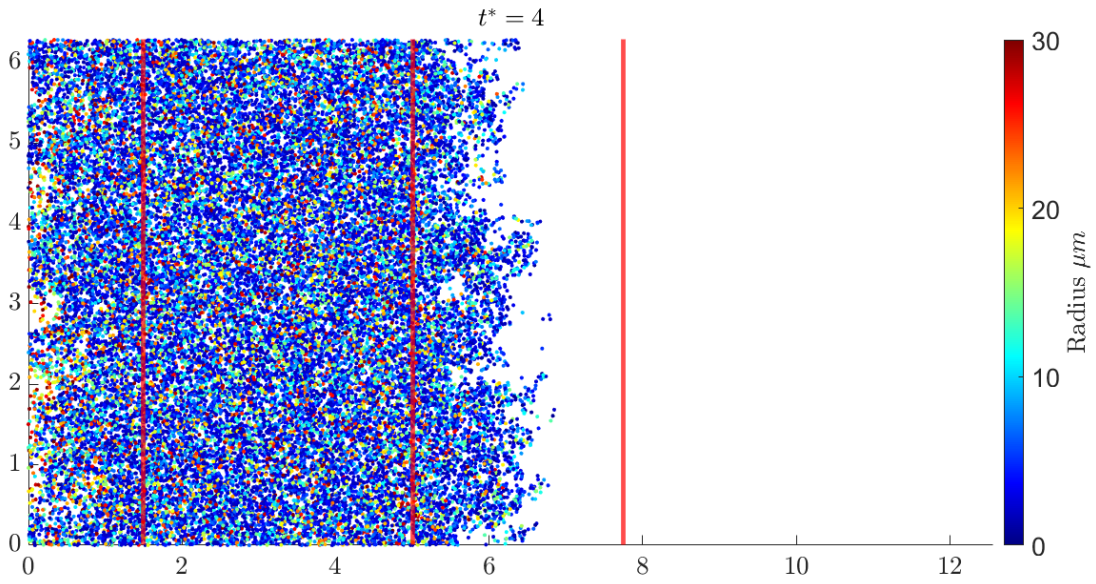

Figure 5.2. Beginning from the left we have: (i) lower mixing, (ii) homogeneous cloud, (iii) mixing, (iv) clear air. The regions are dynamically chosen in time, using both supersaturation level and velocity fluctuations as criteria. On has to know that also the upper boundary of the domain is characterized by a turbulent mixing, but since there are not particles it will not be studied. The spots in the image represent droplets, their color identifies their size according to the color bar.

5.1 Unstable

The numerical results that are reported in fig. 5.3, it represent both cloud and mixing region time evolution as result of three ensemble averages. We collect and mediate the results for three unstable simulations with different flow initial condition, in order to have a richer statistics. The first row is related to the mixing collisions kernel, while the second shows cloud one.

As regards the region of homogeneous cloud there is not much to add to what has already been said in the previous chapter, apart from the fact that in the last time interval the low turbulent energy plus the effect of gravitational shifting have depleted the population of the biggest particles, that are fallen out of the domain, resulting in a poor number of collisions.

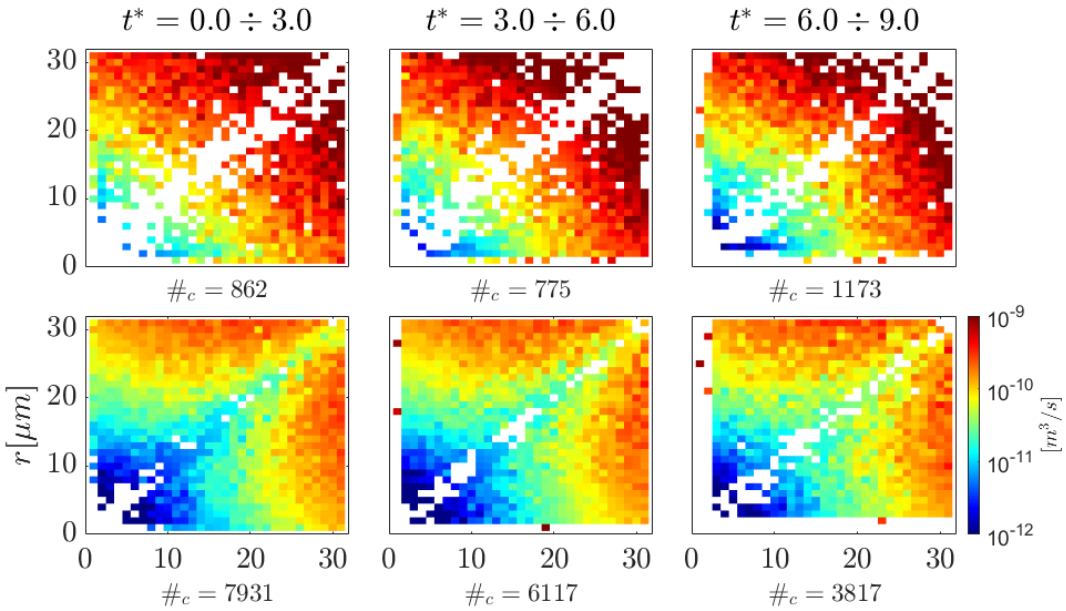

Figure 5.3. The first row describes the evolution of the collision kernel $[m^3/s]$ measured in the **mixing**, the second row is related to the **cloud** region (homogeneous isotropic), both computed with $\Delta r = 1\mu m$, that leads to 32 bins. The dissipation of turbulent kinetic energy decays from an initial value of $\epsilon \sim 600\, cm^2/s^3$ for HIT region and $\epsilon \sim 400\, cm^2/s^3$ for mixing region, with a $(t^*)^{-2}$ time dependence. The values associated to every kernel are respectively the mean ones in the Δt^*, so in HIT they are $\epsilon \sim 270{,}50{,}20\, cm^2/s^3$ and in mixing they are $\epsilon \sim 200{,}40{,}15\, cm^2/s^3$, as already reported in fig.3.3 in chapter regarding droplet collisions. The value $\#_c$ is the number of detected collisions in the period of time in which kernel is evaluated. The increasing lack of data related to the first two classes is due to the very low number of droplets in that bins: in the cloud they are growing in volume since $\Phi > 1$ and so less and less particles will result in the smaller classes. This effect is dumped in mixing since there, somewhere, it is $\Phi < 1$ and so bigger particles will decrease to smaller sizes.

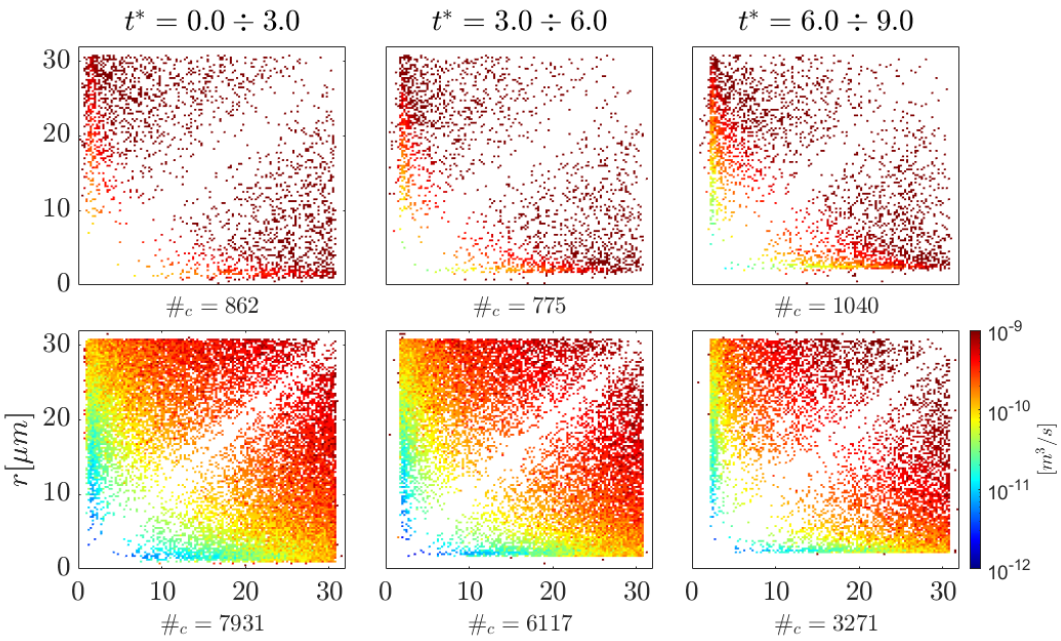

Figure 5.4. This picture represents the collisions kernels in the same conditions as the previous picture (first row is mixing region, second one is homogeneous region), but here the results are plotted for 128 bins ($\Delta r \simeq 0.25\mu m$). It is evident that changing the number of bins affects the magnitude of the results (Δr directly acts on the population associated to each cell, changing the kernel value), in particular here is found an overall increase in magnitude and the "lobes" pattern of the cloud portion is not so evident as in the 32 bins representation.

It is more interesting the result in mixing region: it appears clearly that the magnitude is much higher with respect to the cloud region. This can be explained looking at the way kernel is evaluated:

$$\Gamma_{ij} = \frac{\dot{n_{ij}}}{n_i n_j} = \frac{\dot{N_{ij}}}{N_i N_j} \cdot \frac{\Delta V}{\Delta t} \tag{5.2}$$

Looking at 5.2 we can see that the magnitude of a computational collision kernel depends on the volume in which is evaluated:

$$\Delta V \uparrow\downarrow \Rightarrow \Gamma_{ij} \uparrow\downarrow \tag{5.3}$$

We can notice now that in the mixing region the volume in which collisions effectively happen is smaller than ΔV that include the whole mixing region (see fig. 5.5,5.6), in fact collision between two drops happens mostly in branches of cloud, this is a sort of clustering of particles in the mixing. On another point of view we are showing that the density of drops n $[\#/m^3]$ is lower in the mixing than in the homogeneous region.

$$n_i, n_j \downarrow \Rightarrow \Gamma_{ij} \uparrow \tag{5.4}$$

So this is the reason why it is more intense, if we had chosen the real volume occupied by particles, and not the whole mixing volume, we will not have seen this increase in magnitude. This will be proven in chapter 6 where will be shown that the kernel in a mixing environment between two clouds is slightly changing respect to the homogeneous one. We can also underline that in mixing region we did not observe collisions between equals and nearly equals particles. The pattern also looks more striped, a part of course from nearly equal droplets; they seems very unlikely to collide because of lack of detected collisions.

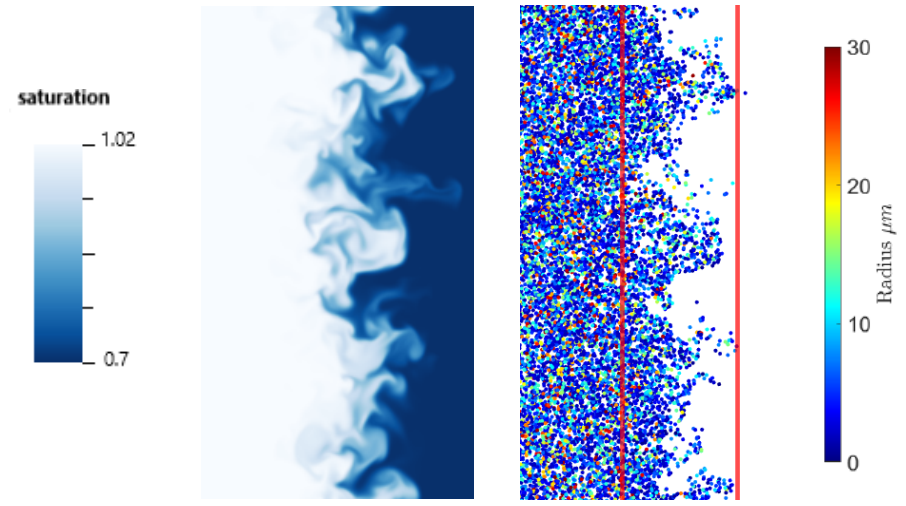

Figure 5.5. The picture shows a mixing region, the red rectangle represents the ΔV. The right hand side figure is the distribution of drops at $t^* = 3$ in mixing, the figure on the left is the saturation level in same region at same time. It can seen that particles are distributed mostly in over saturated branches (bright white areas).

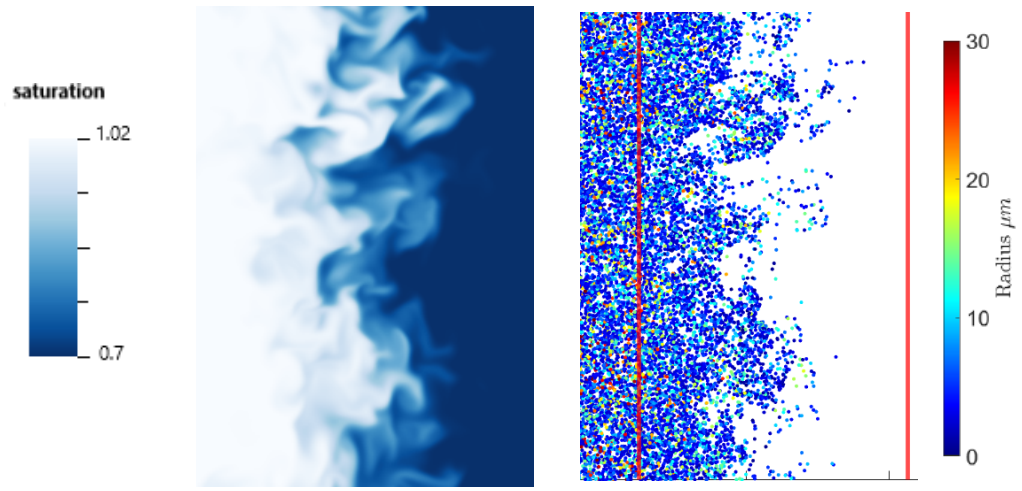

Figure 5.6. The picture shows the same mixing region at $t^* = 9$. At this time the gradient of saturation across mixing is not as sharp as in the previous figure, the environment is moving to an homogeneous point, and so particles lie in both over and under saturated zones (light blue plumes).

There is also an evidence of particles fall due to gravity, one can see that in the up right corner of the kernel (the one corresponding to the biggest particles) there is an emptying over time, it is because since the turbulence is less and less energetic heavier droplets leave the mixing region driven by gravity. This has been observed and clearly shown in fig. 5.7

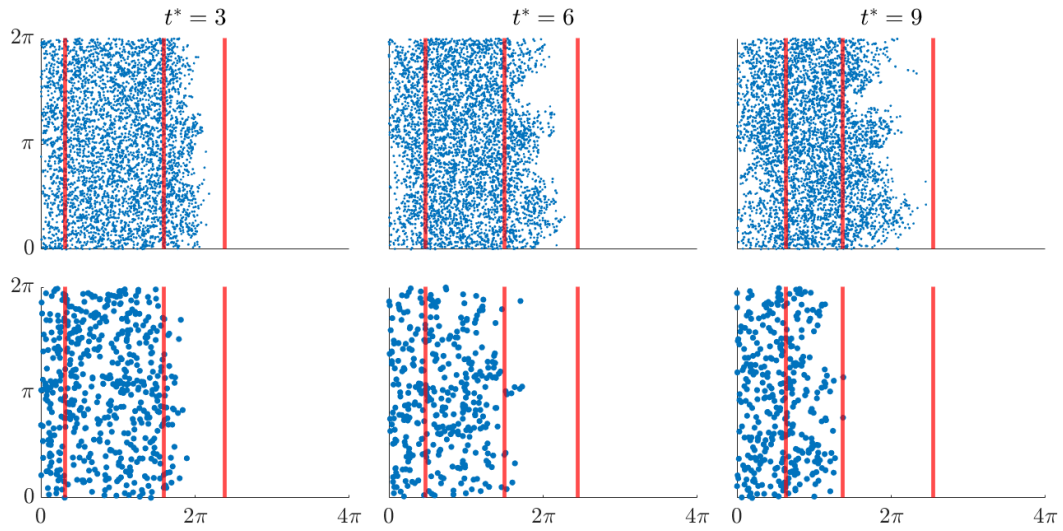

Figure 5.7. The panel reports two different classes of drops in subsequent instants; the first row describes the population in longitudinal plane of 5 μm radius droplets. The second row describes, in the same plane, the population of 30 μm radius droplets. It appears clearly that the larger ones are more affected by gravity (left shifting in the picture).

5.1.1 Mixing region: finer Δt^* analysis

In this subsection is briefly reported an analysis made on the three ensemble averages using $\Delta t^* \simeq 0.8$. Since there are data from three simulations one should be able to provide a more continuous solution, reducing the time interval but maintaining a significant number of collisions. As one can see in the next pages the number of ensemble averages done is still not large enough to provide data for every possible collision that the kernel could describe. So this lead to state that in order to have results regarding the full kernel one should run several more simulations and take the ensemble average.

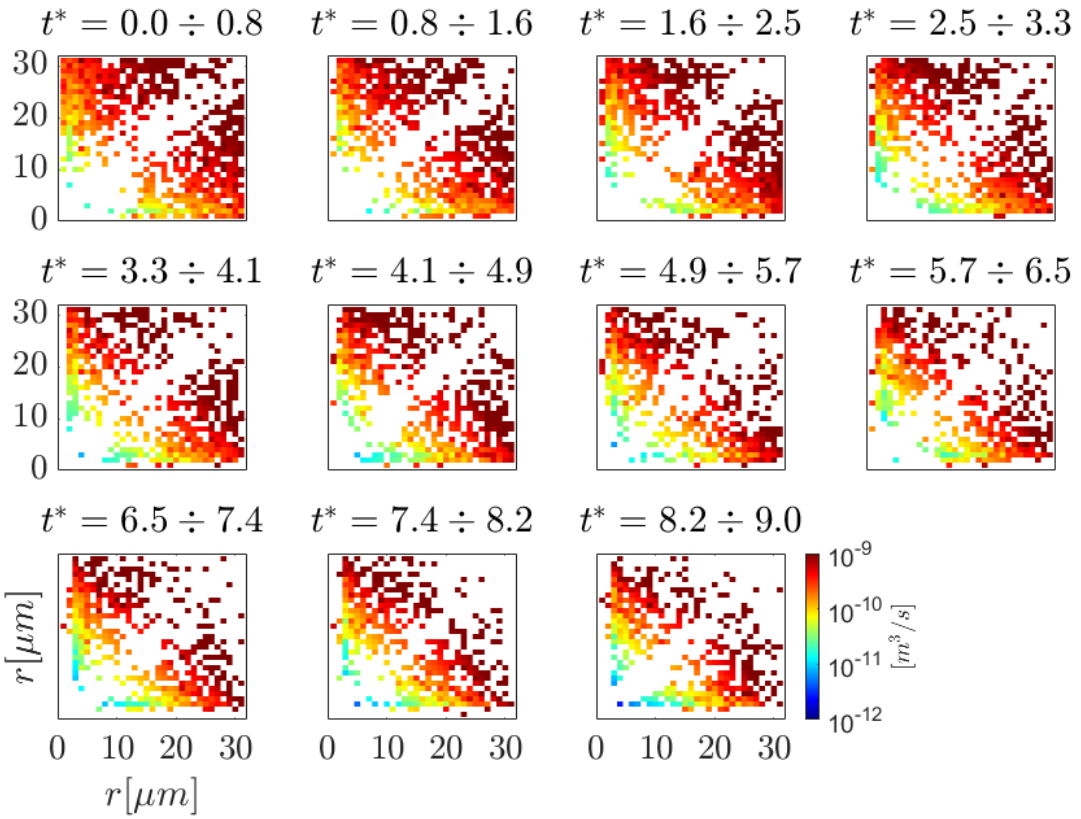

Figure 5.8. Time evolution of numerical collision kernel $[m^3/s]$ in mixing region for 32 bins. One can notice that there are not significant changes in pattern, but there is a decrease of detected collisions over time between high inertia droplets. The mean number of collision in $\Delta t^* \simeq 0.8$ is about 300 and the bins are $\Delta r = 1\mu m$ spaced.

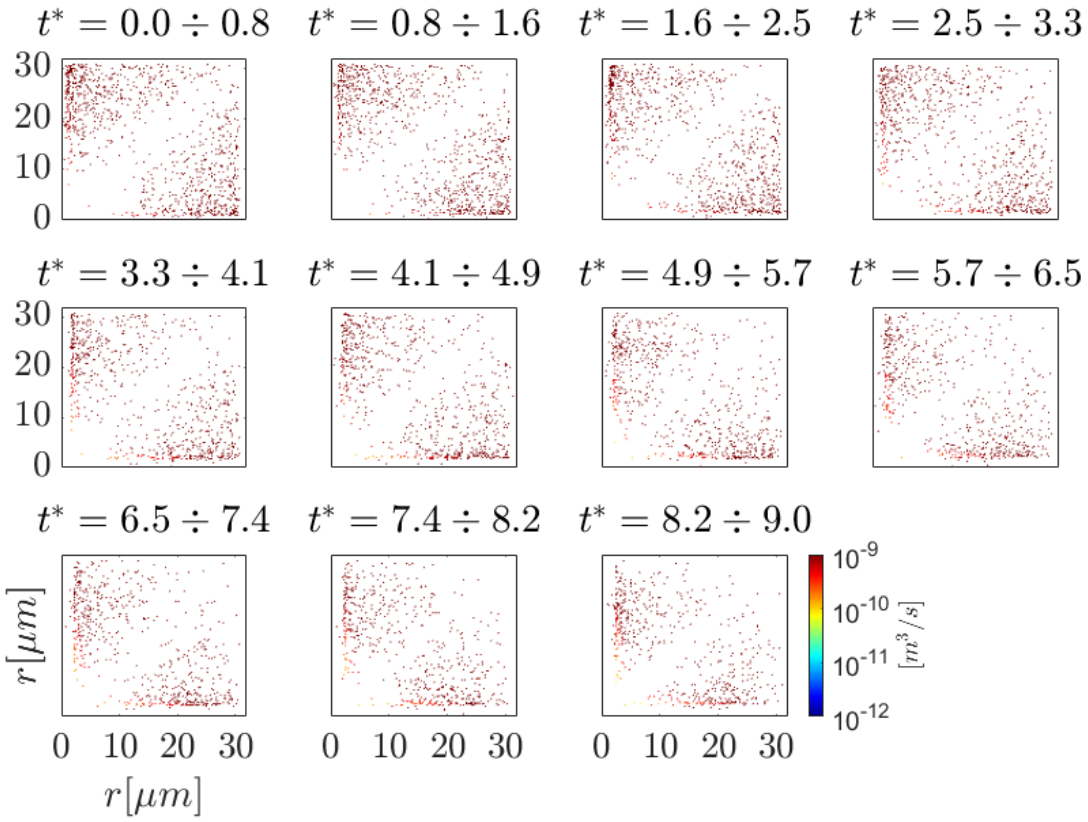

Figure 5.9. Time evolution of numerical collision kernel $[m^3/s]$ in mixing region for 128 bins. Once again the magnitude of the kernel has changed with Δr, this is a bias of our measurements. This picture can be a detailed visualization of which particles mostly collide in a short time interval. The regions that show a bigger number of collisions (clusters of point in the kernel) are the ones coupling medium/big size ($r > 10\mu m$) particles with very small ones ($r < 5\mu m$). This fact is reasonable if one considers that they have different inertia and so the dynamic action of the environment on them will act differently: they will not follow same trajectories and will tend to collide more frequently.

5.2 Lower cloud-clear air mixing region

The lower part of the cloud is interfacing with a clear air environment, because of the nature of pseudo spectral numerical methods, that requires periodic boundary conditions. So we use this bias as a benchmark for collision kernel in a mixing of different kind. In particular we have a positive temperature step from the bottom to the top, that means a stable stratification. The results are shown in 5.10 and 5.11. It can be seen that the mean magnitude is slightly greater than the corresponding one for the cloud, but is much smaller that the one relative to the other mixing region. This is because here the fraction of volume occupied by drops tend to be the full region, as can be clearly seen in fig. 5.2. This greater filling is due both to the initial condition, which foresees particles up to the lower end of the cloud (and therefore to the calculation domain), and to the effect of gravity combined with the energetic decay of the turbulence, which precipitates the particles. The stripes pattern that we spot in the other mixing collision kernel is no more evident, in time the pattern looks more similar to the one found in HIT cloud portion.

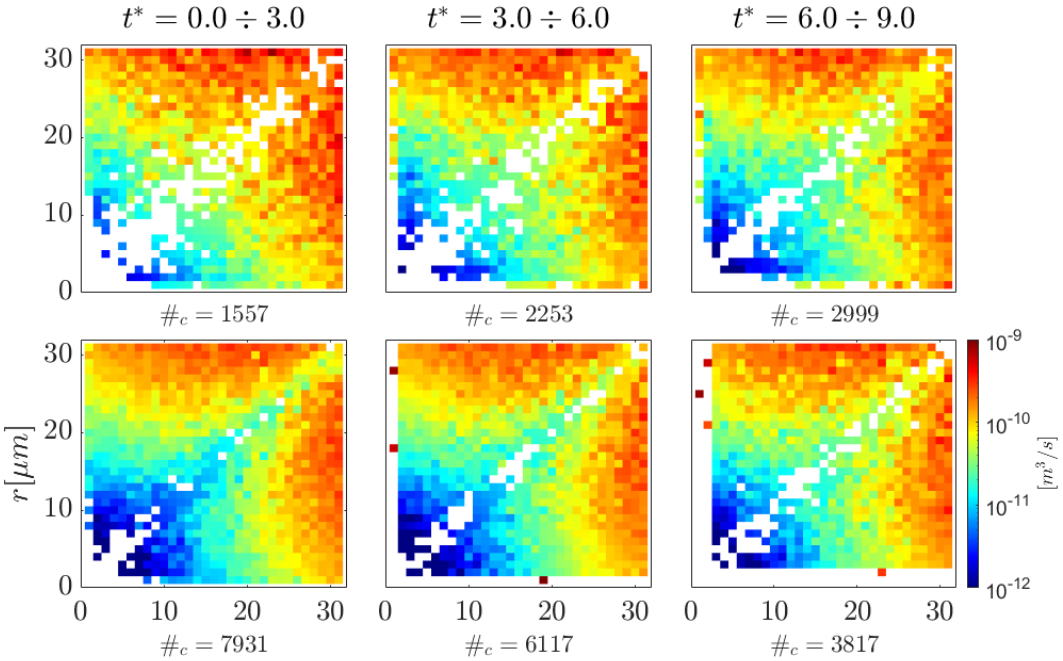

Figure 5.10. First row describes the collision kernel $[m^3/s]$ in the **lower mixing region** of the unstable simulations, the second row is the time evolution of homogeneous isotropic cloud collision kernel. The adopted bins are 32 with $\Delta r = 1\,\mu m$. The value $\#_c$ is the number of detected collisions in the period of time in which kernel is evaluated.

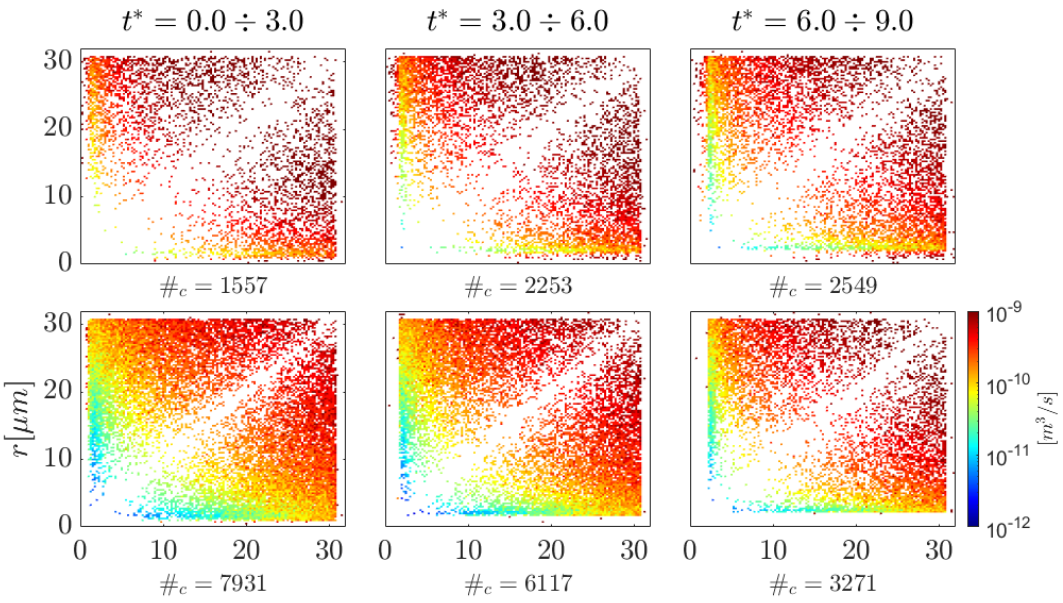

Figure 5.11. This plot reports the results obtained with the 128 bins computation. As before first row describes the collision kernel in the **lower mixing region**, the second row is the time evolution of homogeneous isotropic cloud collision kernel. It is adopted $\Delta r = 0.25\,\mu m$. The value $\#_c$ is the number of detected collisions in the period of time in which kernel is evaluated. Here, as in the previous picture, the pattern of the mixing region is quite close to the one found in HIT cloud portion.

5.3 Stable and neutral

The stable stratification is imposed swapping the maximum temperature from the cloud to the clear-air in the initial temperature profile. The neutral condition is imposed with a constant $T = 281K$ initial profile. This section comprehends two configurations because, as will be shown, the stratification slightly affects the behavior of the kernels.
Given the wide demand for computational resources for each of these simulations, in this case no ensemble averages were made, the results shown are relative to a single simulation. The figs. 5.12 and 5.14 show the results for both these configuration, by looking at them is pretty clear that there are not significant differences in cloud and mixing (respectively between the two configurations) collision kernels. In both simulations we can see already known patterns both in the cloud and in the mixing. In particular in the mixing it is more evident the effect of the gravitational fall: kernels are increasingly empty over time in the cells related to high radius particles (upper right corner), the action of gravity is shifting droplets out of mixing area.

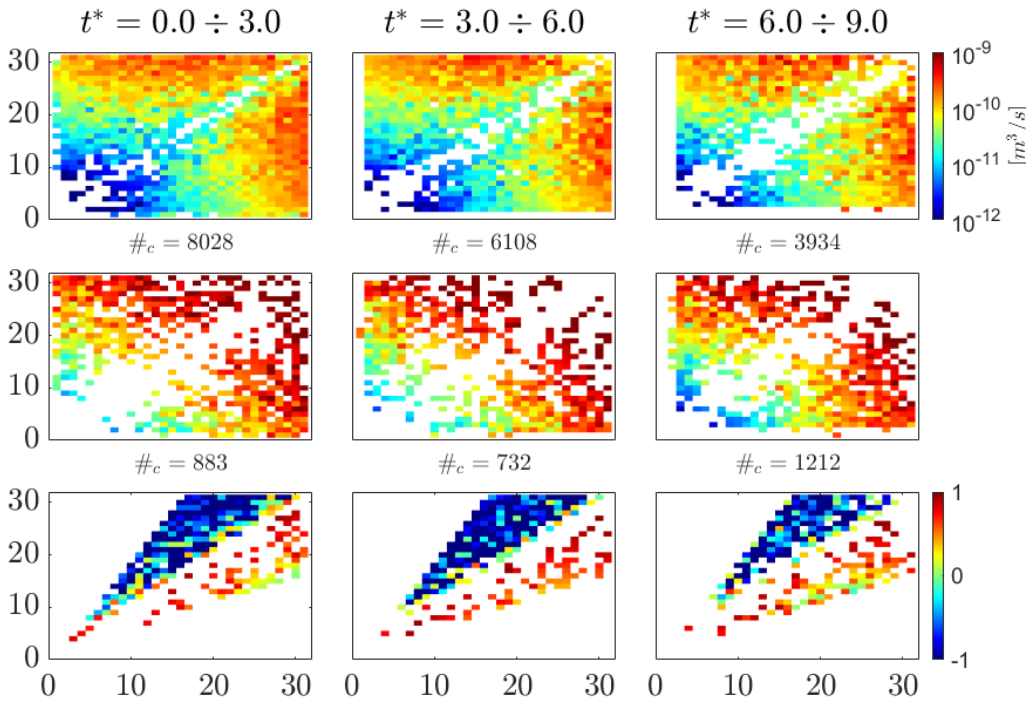

Figure 5.12. **Stable stratification.** The first row describes the evolution of the collision kernel $[m^3/s]$ measured in the **cloud** (homogeneous isotropic), the second row is related to the **mixing** region. The third row contains the relative errors time history for both cloud (upper triangular matrix) and mixing (lower triangular matrix) with respect to Saffman and Turner model (again it is important to remember that their model is not able to describe our system, but it is interesting to compare with, in order to highlight the main differences). The uniform error of the homogeneous region means, once again, accordance with Saffman and Turner pattern. The adopted bins are $\Delta r = 1\mu m$ wide. The dissipation of turbulent kinetic energy decays from an initial value of $\epsilon \sim 600\, cm^2/s^3$ for HIT region and $\epsilon \sim 400\, cm^2/s^3$ for mixing region, with a $(t^*)^{-2}$ time dependence. The values associated to every kernel are respectively the mean ones in the Δt^*, so in HIT they are $\epsilon \sim 250{,}40{,}15\, cm^2/s^3$ and in mixing they are $\epsilon \sim 170{,}35{,}15\, cm^2/s^3$. The value $\#_c$ is the number of detected collisions in the period of time in which kernel is evaluated.

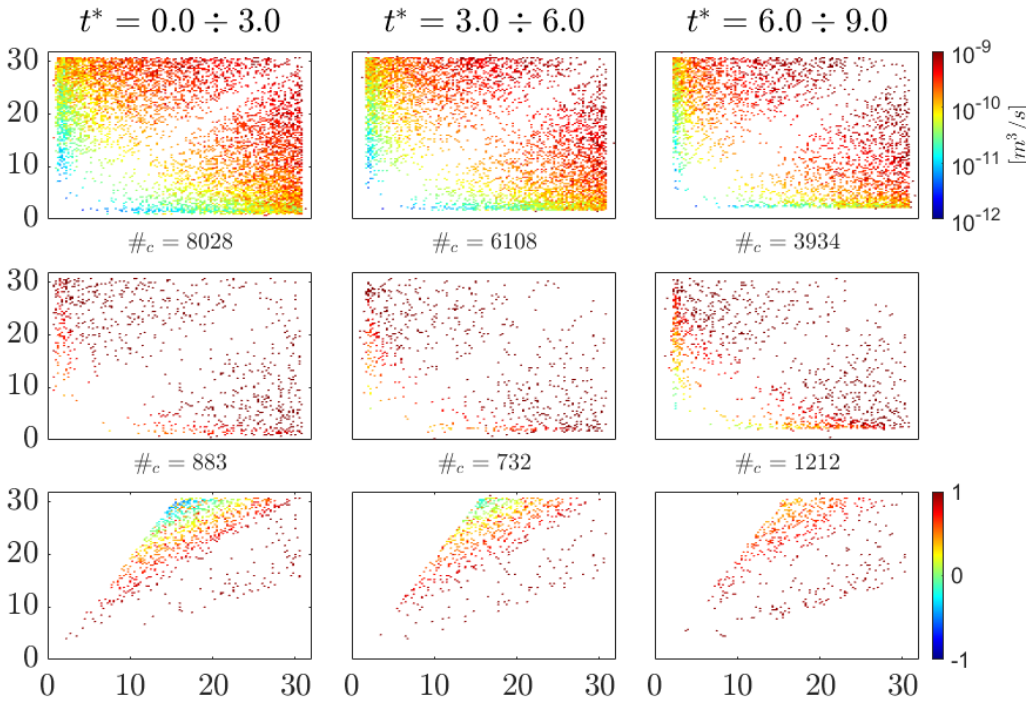

Figure 5.13. **Stable stratification.** This picture is the equivalent of the previous one, but the kernel is computed using 128 bins ($\Delta r = 0.25\mu m$ wide) and this has changed the results, with an overall magnitude increasing. The reason why this happens is reported in section 3.1.3. The first row describes the evolution of the collision kernel $[m^3/s]$ measured in the **cloud** (homogeneous isotropic), the second row is related to the **mixing** region. The third row contains the relative errors time history for both cloud (upper triangular matrix) and mixing (lower triangular matrix) with respect to Saffman and Turner model (again it is important to remember that their model is not able to describe our system, but it is interesting to compare with, in order to highlight the main differences). The dissipation of turbulent kinetic energy decays from an initial value of $\epsilon \sim 600\, cm^2/s^3$ for HIT region and $\epsilon \sim 400\, cm^2/s^3$ for mixing region, with a $(t^*)^{-2}$ time dependence. The values associated to every kernel are respectively the mean ones in the Δt^*, so in HIT they are $\epsilon \sim 250{,}40{,}15\, cm^2/s^3$ and in mixing they are $\epsilon \sim 170{,}35{,}15\, cm^2/s^3$. The value $\#_c$ is the number of detected collisions in the period of time in which kernel is evaluated.

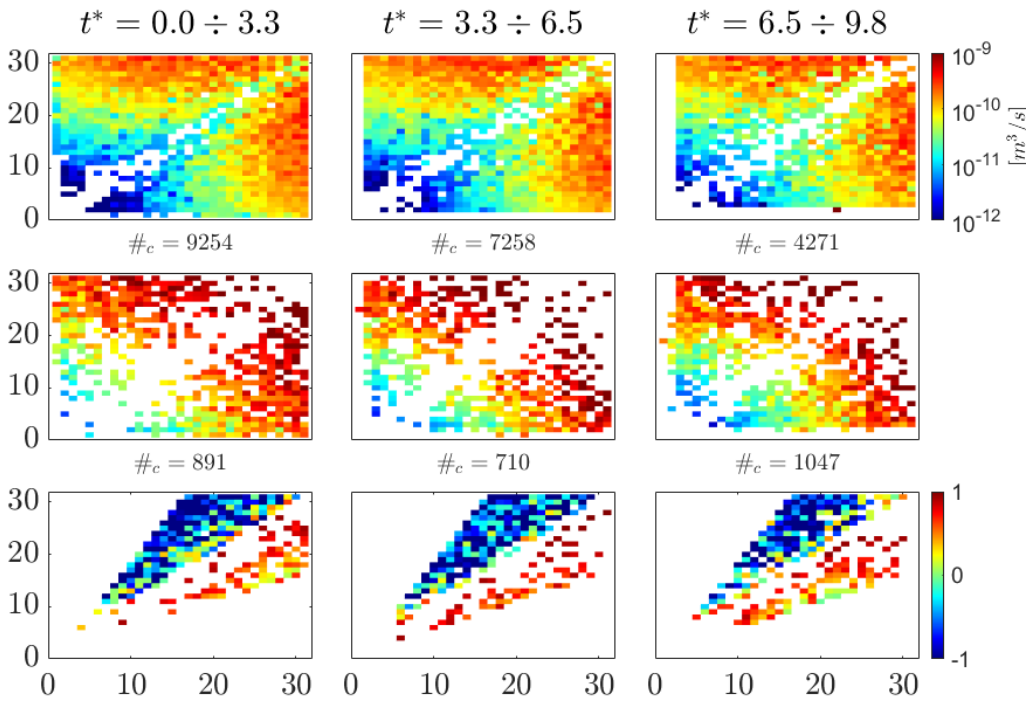

Figure 5.14. **Neutral stratification.** The first row describes the evolution of the collision kernel $[m^3/s]$ measured in the **cloud** (homogeneous isotropic), the second row is related to the **mixing** region. The third row contains the relative errors time history for both cloud (upper triangular matrix) and mixing (lower triangular matrix) with respect to Saffman and Turner model (again it is important to remember that their model is not able to describe our system, but it is interesting to compare with, in order to highlight the main differences). The uniform error of the homogeneous region means, once again, accordance with Saffman and Turner pattern. The adopted bins are $\Delta r = 1\mu m$ wide. The dissipation of turbulent kinetic energy decays from an initial value of $\epsilon \sim 600\, cm^2/s^3$ for HIT region and $\epsilon \sim 400\, cm^2/s^3$ for mixing region, with a $(t^*)^{-2}$ time dependence. The values associated to every kernel are respectively the mean ones in the Δt^*, so in HIT they are $\epsilon \sim 255{,}40{,}15\, cm^2/s^3$ and in mixing they are $\epsilon \sim 175{,}35{,}15\, cm^2/s^3$. The value $\#_c$ is the number of detected collisions in the period of time in which kernel is evaluated.

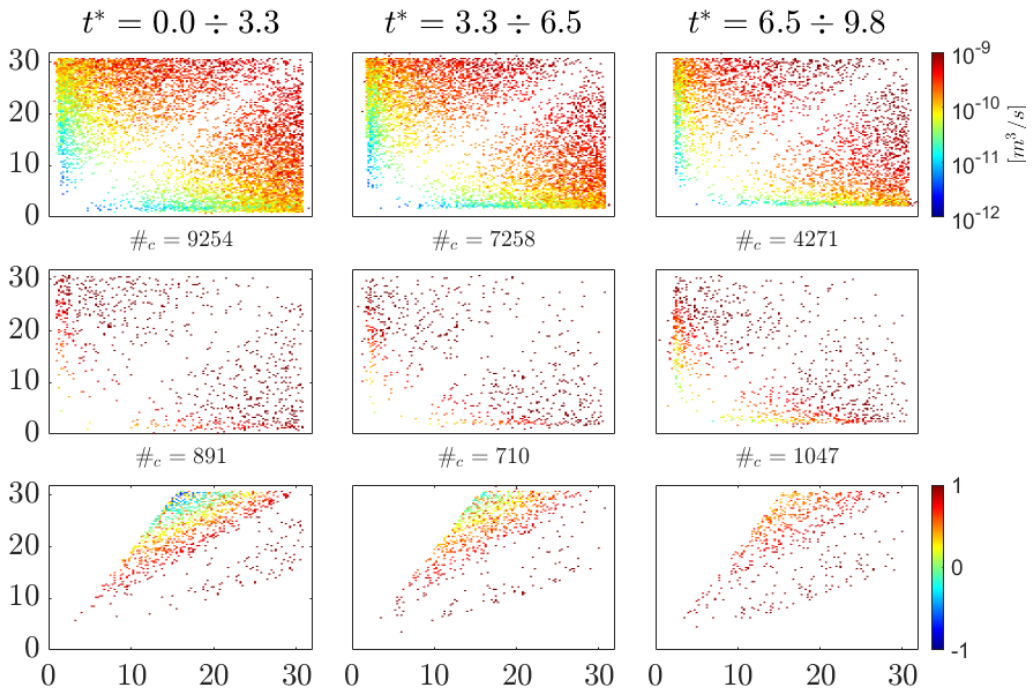

Figure 5.15. **Neutral stratification.** This picture is the equivalent of the previous one, but the kernel is computed using 128 bins ($\Delta r = 0.25\mu m$ wide). The first row describes the evolution of the collision kernel $[m^3/s]$ measured in the **cloud** (homogeneous isotropic), the second row is related to the **mixing** region. The third row contains the relative errors time history for both cloud (upper triangular matrix) and mixing (lower triangular matrix) with respect to Saffman and Turner model (again it is important to remember that their model is not able to describe our system, but it is interesting to compare with, in order to highlight the main differences). The dissipation of turbulent kinetic energy decays as in fig 5.14. This picture, in particular the mixing row, shows that the gravity is acting on the kernel, in a way that the collisions regarding bigger particles are less and less in time, this is because they are shifting down, leaving the mixing region. The changes of these kernels with respect to the 32 bins ones is as usual due to the different Δr, as explained in section 3.1.3.

Chapter 6

Analysis of collision kernel in anisotropic test cases

This chapter reports two simulations carried out in conditions different from those treated so far. In particular, they were carried out to study the effects of anisotropy of turbulent mixing, in the event that two portions of different environment come into contact, both loaded with water particles. In both cases the two turbulent fields have a kinetic energy of fluctuations ratio of ~ 6.6 (as in all the previous simulations), but in one we set a condition of relative humidity of 100% ($RH = 1$) all over the domain, in the other we set $RH = 1.02$ for the high energy turbulent field and $RH = 0.70$ for the remaining low energy turbulent field. The initial conditions for temperature and flow are the same that we have for the simulations in section 5.1.
From these simulations we can investigate a phenomenon that could happen in some industrial applications, but also we can test if the increase in magnitude that we observed for the kernel in mixing in chapter 5.1 is associated to the volume occupied by particles.

6.1 Different relative humidity

This simulation was specifically designed to verify what would have happened to the kernel in the mix between cloud and clear air (unstable stratification) if the particles had occupied the entire volume in which the mixing evolves. Results are reported in fig. 6.1 and they clearly show that both magnitude and pattern are not affected by the mixing condition. The mixing kernel is a bit sparser because it is computed in fraction of volume smaller than the clouds one, so there are less collisions. In this case also the nearly equal particles behave in the same way regardless if they are in cloud or mixing region (both kernels diagonals are empty). We can conclude remarking that in this configuration of mixing there are not significant differences with an homogeneous turbulent environment.

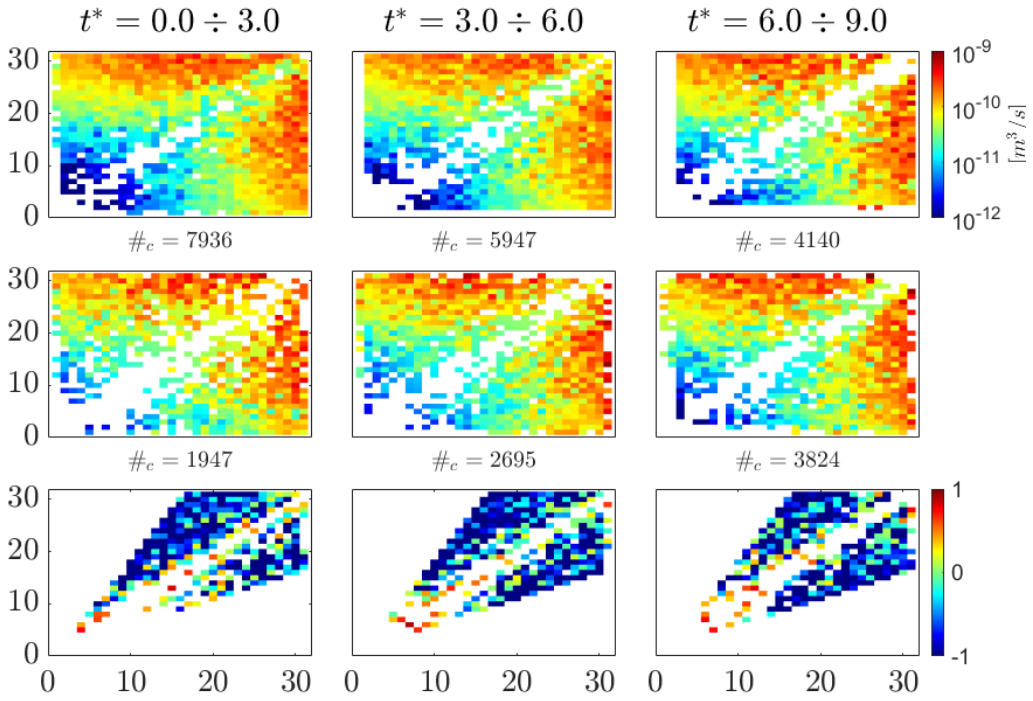

Figure 6.1. The first row describes the evolution of the collision kernel $[m^3/s]$ measured in the **cloud**, the second row is related to the **mixing** region. The third row contains the relative errors time history for both cloud (upper triangular matrix) and mixing (lower triangular matrix) with respect to Saffman and Turner model (again it is important to remember that their model is not able to describe our system, but it is interesting to compare with, in order to highlight the main differences). In these numerical analysis both mixing and HIT errors are uniform, so both regions are according the pattern of Saffman and Turner model. The adopted bins are $\Delta r = 1\mu m$ wide. The dissipation of turbulent kinetic energy decays from an initial value of $\epsilon \sim 600\, cm^2/s^3$ for HIT region and $\epsilon \sim 400\, cm^2/s^3$ for mixing region, with a $(t^*)^{-2}$ time dependence. The values associated to every kernel are respectively the mean ones in the Δt^*, so in HIT they are $\epsilon \sim$ 270,50,20 cm^2/s^3 and in mixing they are $\epsilon \sim$ 200,40,15 cm^2/s^3, as already reported in fig.3.3 in chapter regarding droplet collisions. The value $\#_c$ is the number of detected collisions in the period of time in which kernel is evaluated.

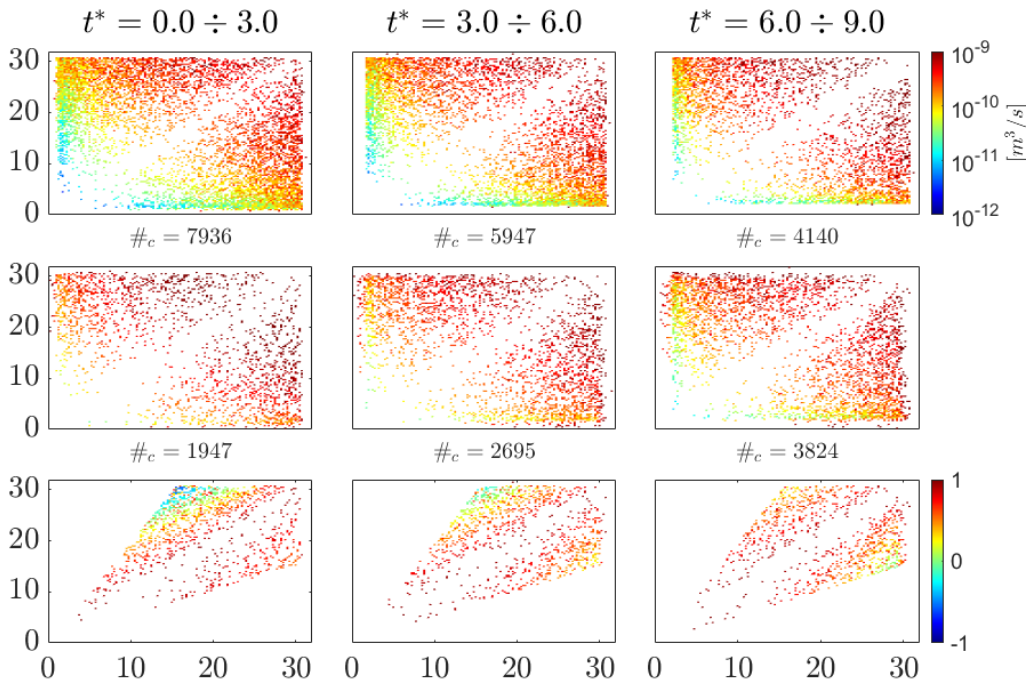

Figure 6.2. This picture is the analogue of the previous one, with kernels evaluated with 128 bins and $\Delta r = 0.25\mu m$. All the fluid dynamics details are reported in the previous picture, see fig. 6.1, while the reason of the change in magnitude is explained in section 3.1.3.

6.2 Saturated environment

This simulation denies the effect of supersaturation: in this way, comparing with the simulation of the previous section, we can investigate how much the under saturation level was influencing the collision kernels, because with a homogeneous level of unity saturation, droplets will not grow/decrease their volume. The only factor that can change their size is the coalescence by collision. The results are reported in fig. 6.3 in the usual way.

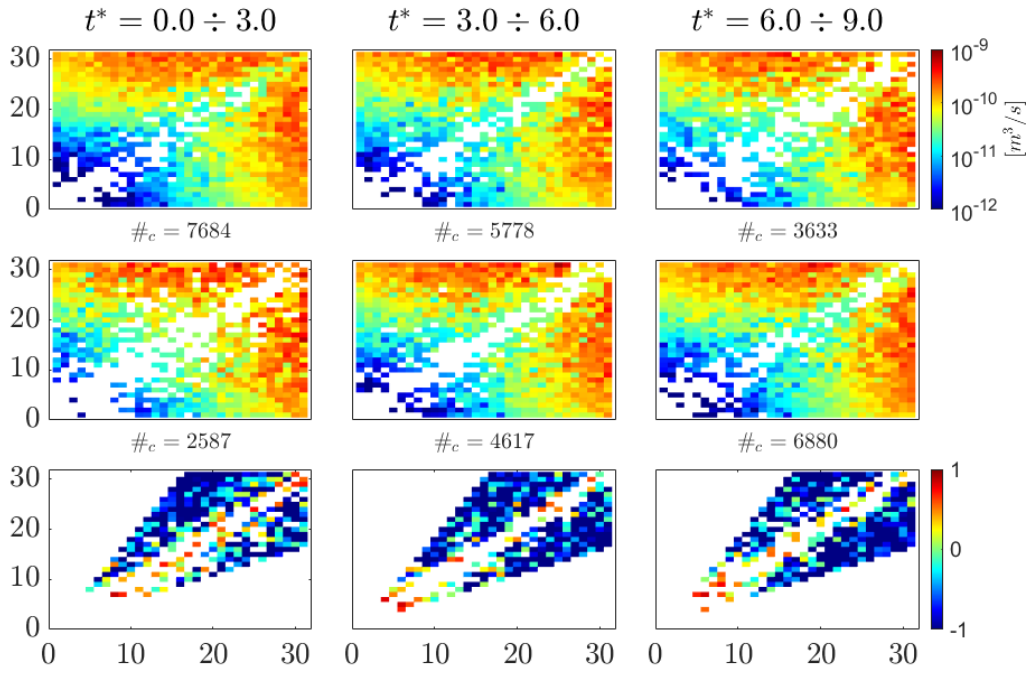

Figure 6.3. The first row describes the evolution of the collision kernel $[m^3/s]$ measured in the **cloud**, the second row is related to the **mixing** region. The third row contains the relative errors time history for both cloud (upper triangular matrix) and mixing (lower triangular matrix) with respect to Saffman and Turner model (again it is important to remember that their model is not able to describe our system, but it is interesting to compare with, in order to highlight the main differences). In this simulation, as in the previous one, both mixing and HIT errors are uniform, so both regions are according the pattern of Saffman and Turner model. The adopted bins are $\Delta r = 1\mu m$ wide. The dissipation of turbulent kinetic energy decays from an initial value of $\epsilon \sim 600\, cm^2/s^3$ for HIT region and $\epsilon \sim 400\, cm^2/s^3$ for mixing region, with a $(t^*)^{-2}$ time dependence. The values associated to every kernel are respectively the mean ones in the Δt^*, so in HIT they are $\epsilon \sim 270$,50,20 cm^2/s^3 and in mixing they are $\epsilon \sim 200$,40,15 cm^2/s^3, as already reported in fig.3.3 in chapter regarding droplet collisions. The value $\#_c$ is the number of detected collisions in the period of time in which kernel is evaluated.

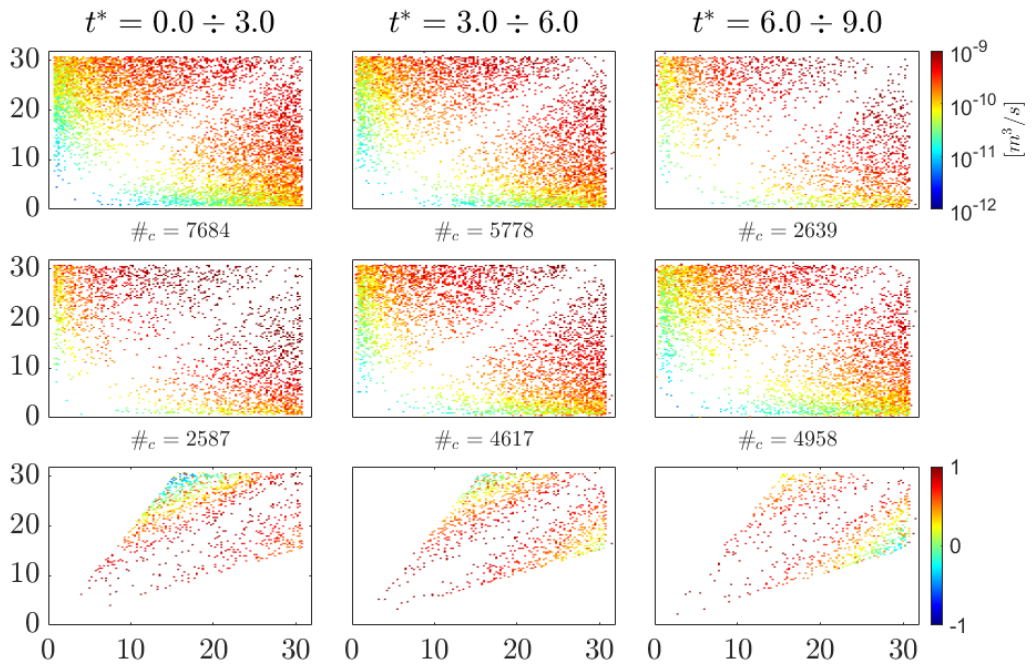

Figure 6.4. This picture is the analogue of the previous one, here the kernels are evaluated with 128 bins and $\Delta r = 0.25\mu m$. Again one can find all the fluid dynamics details in the previous picture, fig. 6.3 and the explanation of the differences between 32 and 128 bins results in section 3.1.3

In conclusion the kernels described in sections 6.1, 6.2 are very close to each other, regardless of the supersaturation level; the HIT ones are very similar with themselves and the same is true for the ones associated to mixing region (of course considering the same Δr). They refer to the same fluid dynamics conditions, but the particles are initially distributed randomly in the domain, for each simulation. Since we got this results we can state that in 9 eddy turnover time the effects on collision kernels of the whole saturated environment are quite the same as $1.02 \div 0.7$ supersaturation distribution.

The main difference that one can notice is that in time, for the non uniform supersaturation level (section 6.1), the collisions involving smallest classes are disappearing in the HIT kernel. This happens because since supersaturation $\Phi > 1$ in the cloud, they all grow, and since there is not fragmentation implemented, after some time scales all the smallest drops will be grown and will be recorded in bigger radius classes.

Chapter 7

Turbulent flow small scale anisotropy effect in mixing collision kernel

Now that one has the unstable simulation (exposed in 5.1) and the unstable one with particles everywhere in the domain (in 6.1), it is very interesting to look at them and compare their kernel in the mixing, using also some properties reflecting the anisotropy of the flow. In particular one can notice that there is correlation between the anisotropy properties of the turbulent flows studied and the associated collision kernels only for the simulation that has particles in half of the domain (5.1), while the *artificial* one has not any significant relationship with the turbulent shearless mixing anisotropy properties.

7.1 Skewness of velocity derivatives

The presence of small scale anisotropy in this kind of turbulent mixing has been proven by Tordella and Iovieno (2011) [7], they showed that studying the skewness of the velocity derivatives $\partial u_1/\partial x_1, \partial u_2/\partial x_2, \partial u_3/\partial x_3$ in isotropic planes in a shearless mixing flow, it can be seen that the one related to the anisotropic direction x_3 behaves in a different way from the others. This fact is also verified in our simulations, as shown in fig. 7.1. Before proceeding it is better to introduce the concept of skewness in a statistical distribution. The k-order statistical moment m_k is defined as:

$$m_k = \frac{\sum_{i=1}^{N} (x' - \bar{x})^k}{N} \tag{7.1}$$

The skewness defines as:

$$s = \frac{m_3}{(m_2)^{\frac{3}{2}}} \tag{7.2}$$

The skewness of a distribution is representative of its asymmetry:

s	**description**
< 0	The most probable values of the distribution are bigger than the mean value of the possible ones.
$= 0$	Symmetric distribution.
> 0	The most probable values of the distribution are smaller than the mean value of the possible ones.

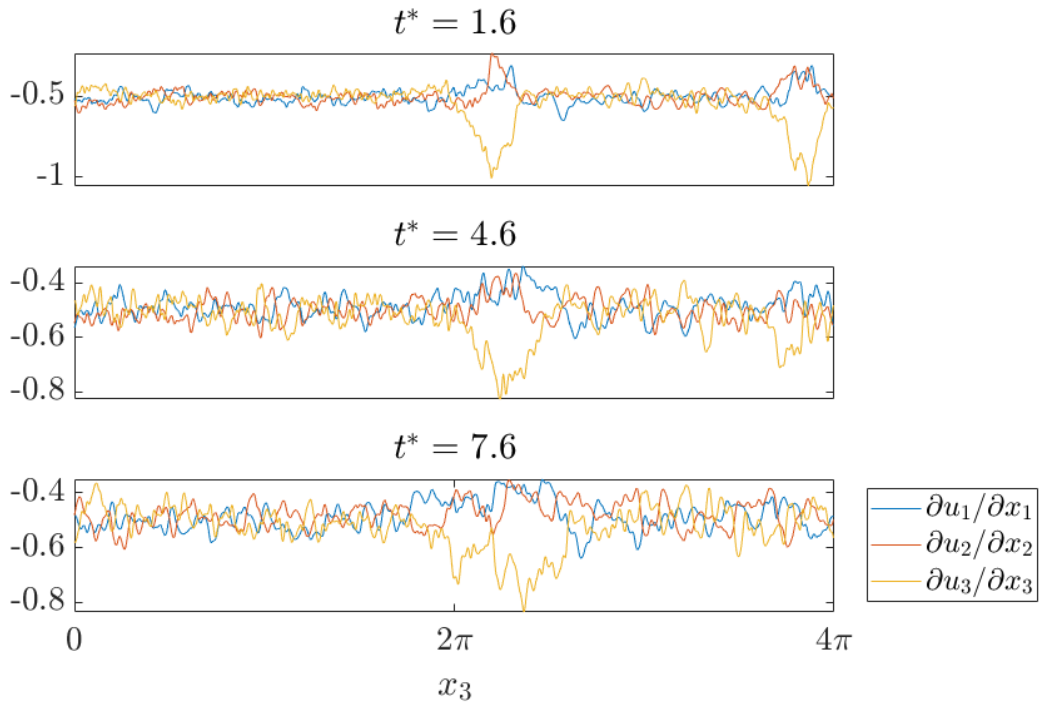

Figure 7.1. Ensemble average of the $\partial u_i/\partial x_i$ skewness for the unstable simulation 5.1. The values are plotted for three time instants t^* and represent the skewness of the derivatives on the isotropic planes ($x_3 = const$). It appears clearly that the derivatives related to isotropic directions (x_1, x_2) behave in the same way, that is different from the one in the anisotropic direction (x_3).

What happen is that there is a compression of the flow that moves perpendicularly to the mixing, while there is a relaxation for the fluid moving along isotropic directions (parallel to the mixing). What we did is to keep track in time of the peak value of the skewness in the mixing region, in order to compare it with the mean magnitude of the collision kernel, referred to the initial one, in time. The results are reported in fig. 7.2, where with the peak time history there are the mean collision kernels of both the simulations. It is evident that the kernel coming from the *artificial* simulation is substantially on average constant in time. A very different behavior is that of the kernel of the other simulation,

the calculated values have been interpolated with the least squares method with a third order polynomial. They show how the intensity of the kernel seems to be related to the skewness of the derivatives, as both have the same trend and have a maximum at similar time instants. So from this we can deduce that the magnitude evolution of the collision kernel in mixing region is strictly linked to the anisotropy of the turbulent mixing.

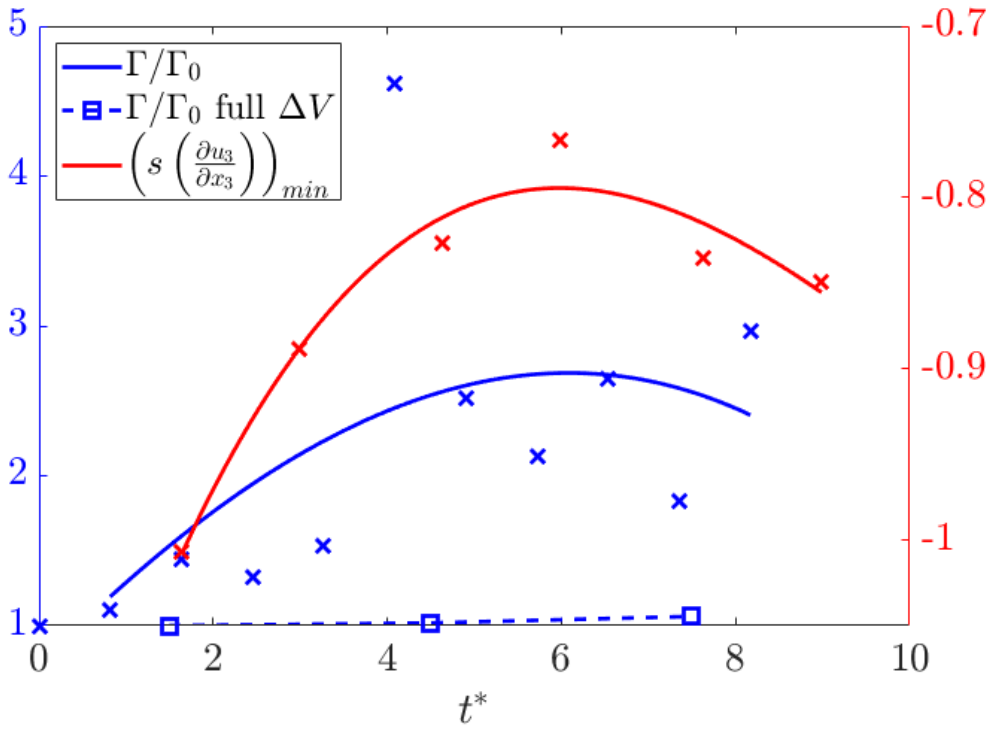

Figure 7.2. Scattered data of kernel magnitude Γ (normalized with the initial one Γ_0) with particle in half of the domain (blue crosses), of kernel magnitude with particle in all the domain (blue squares) and of the peak value of the skewness of $\partial u_3/\partial x_3$ (red crosses). The same trends are found only in the case of mixing between cloud and clear air. The other kernel, the one relative to the distribution of particles all over the domain, keeps a constant mean value in time. The kernel adopted in this plot are the ones evaluated in 32 bins.

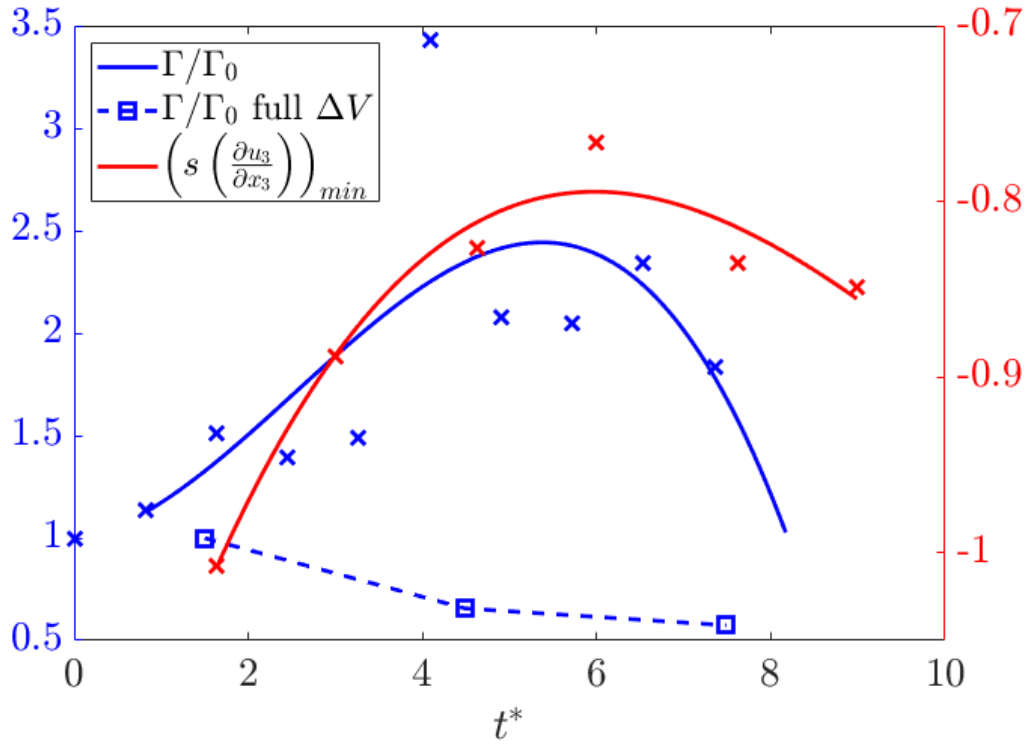

Figure 7.3. This plot reports the same analysis on the 128 bins kernel. As before there are scattered data of kernel magnitude Γ (normalized with the initial one Γ_0) with particle in half of the domain (blue crosses); data of kernel magnitude with particle in all the domain (blue squares) and data of the peak value of the skewness of $\partial u_3/\partial x_3$ (red crosses). As for the 32 bins analysis same trend of skewness is found only for kernel related to mixing region.

7.2 Kurtosis of supersaturation

Another correlation has been found between the mean collision kernel magnitude and the kurtosis of supersaturation. This one can be easily explained recalling the meaning of kurtosis: it is a measure of the intermittency phenomenon in turbulence, that in this case is a jump from supersaturated regions to under saturated ones and vice versa. Recalling that the k-order statistical moment m_k is defined as:

$$m_k = \frac{\sum_{i=1}^{N} (x' - \bar{x})^k}{N} \tag{7.3}$$

The kurtosis defines as:

$$K = \frac{m_4}{(m_2)^2} \tag{7.4}$$

Kurtosis is computed as a fourth order statistical moment and highlights the influence of far-from-mean events in a distribution, the ones represented by the queues of the distribution. This is because of course, since in a random phenomenon (as turbulence is),

intermittent behaviors are characterized by values far from the mean one, they will be represented by the queues of the distribution, and so by kurtosis.

As yet shown in section 5.1 particles tend to stay in supersaturated parts of mixing, because they are brought in mixing region into cloud plumes, that are supersaturated. So high kurtosis means high intermittency, that means high *clustering* of particles (they occupy less space in the ΔV of the mixing) and so an increase in probability of collision, that is the magnitude of the kernel. This strong correlation is reported in fig. 7.4, where the kurtosis of supersaturation is not computed for the first two time scales because the supersaturation initial condition is not physical as it has not fluctuations. From the figure is evident that both the functions oscillates in the same way, while if we have particles everywhere of course they will not be influenced by the kurtosis, because they already are in all the mixing domain.

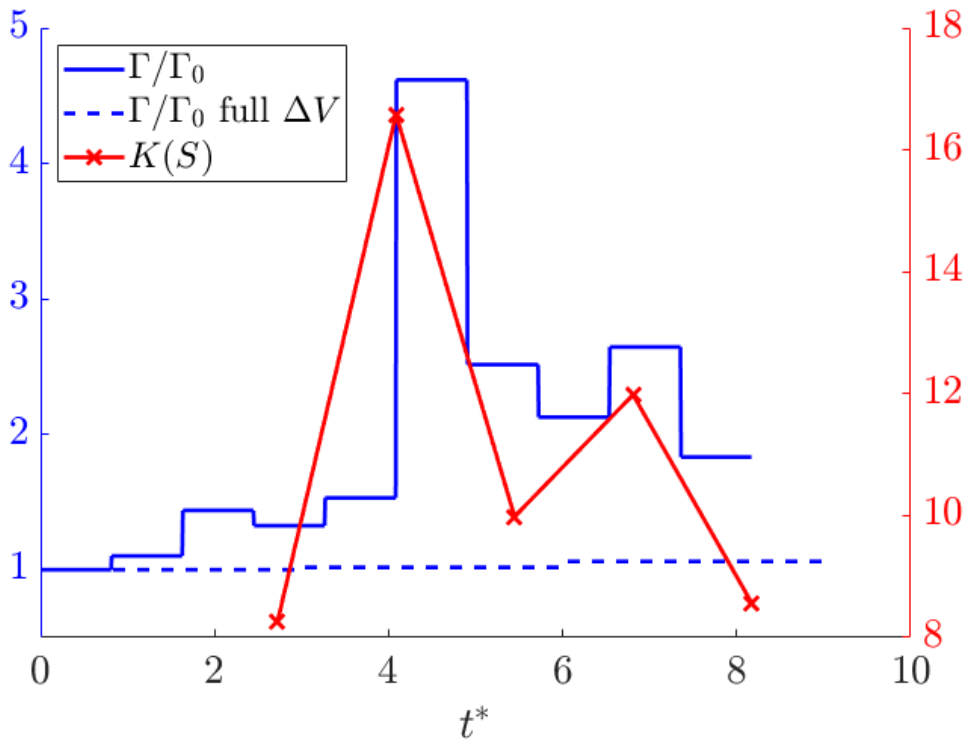

Figure 7.4. The figure above shows the strong correlation between kurtosis of supersaturation distribution $K(S)$ in mixing region (red marks) and the mean magnitude of the collision kernel, normalized with the initial one Γ/Γ_0 (blue line). The dashed blue squared marks reports the kernel mean magnitude in mixing with particle distributed in all the volume ΔV in which mixing happens. This picture refers to 32 bins kernels.

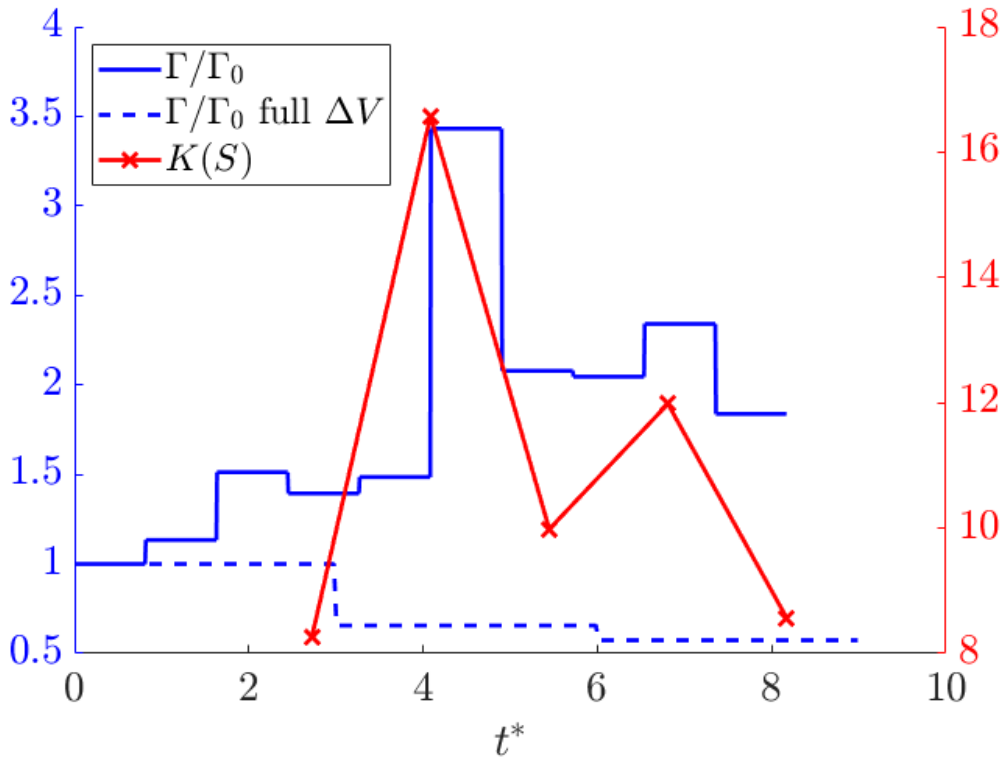

Figure 7.5. The figure above refers to the 128 bins kernels. It shows that even for this measurement there is correlation between kurtosis of supersaturation distribution $K(S)$ in mixing region and the mean magnitude of the normalized collision kernel. The blue squared marks reports the kernel mean magnitude in mixing with particle distributed in all the mixing volume ΔV.

Chapter 8

Collision kernel for mono-disperse initial particles distribution

An interesting application of the collision kernel is to monitor how a population of initially identical drops evolves. In particular it is an index of population expansion, as it reveals, through collisions, the presence of new particles compared to the initial distribution.
For this purpose we set a group of four simulations, all with a different initial condition, but with the same amount of droplets (around $\sim 10^7$) of radius $15\,\mu m$ in an unstable cloud-clear air stratification, as done for the ensemble averages of the multi disperse simulations. The results are exposed in 8.2 for the cloud region, the upper mixing region and the lower one. It appears clearly that in the cloud region droplets experience the same grow rate, because they are immersed in an environment homogeneously super saturated. The frame relative to the first three timescales shows that particles are growing, we can see that the collisions happen between same size particles, but the size is moving towards bigger value than the initial $15\mu m$. The following two frames describe collisions only between same size particles, growth by condensation, meaning that there are not collision with particles already born by collision. Probably because since a collision between two equal particles is very unlikely (see fig. 8.1), the new drops born are much less than those already present since the beginning of the simulation. We did not observe collision with big particles because otherwise we should have detected colliding drops with a radius of $r \simeq \sqrt[3]{2} \cdot 15\mu m \simeq 19\mu m$.
In the mixing areas situation is completely different, we observe an enlargement of the distribution towards smaller radii. This is due to the presence of under saturated branches, which reduce the drops size. The decrease rate is not uniform, because in mixing the level of super saturation is inhomogeneous, and so the distribution of radii is enlarging. At this point we have droplets with different inertia, that are more likely to collide, and that is what happens: we detect many collisions among different sizes particles. In the upper mixing, in the last time interval, we also found a collision with a particle that was already born by collision. In the end we can highlight that the lower mixing is the richer in collisions events, probably because the effect of gravity, that precipitates particles into this area, filling it continuously. This is a clear sedimentation effect. The pattern in the

mixing region is completely different from the one described by Saffman and Turner, but the same is not true for the points in homogeneous region, we found, as shown in fig.8.3, that the kernels have the same order of magnitude, but in the simulation there is a faster decay with respect to the analytical model.

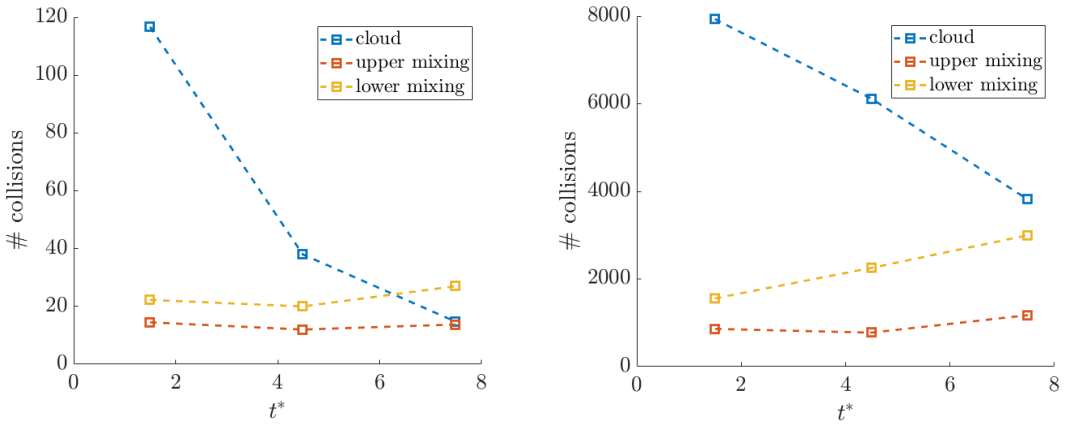

Figure 8.1. The picture shows the detected number of collisions in same turbulent areas, respectively lower mixing, cloud and upper mixing of the monodisperse (left column) and multidisperse (right column) unstable simulations. The most important thing that has to be underlined is that with the same number of particles, in the same turbulent environments, the number of collisions strongly depends on the drop sizes, in fact in the multidisperse simulation one can notice that the number of collision is two order of magnitude greater than the respective monodisperse one. These graphs confirm that, as predicted from Saffman and Turner, the collision between similar or equal droplets are very unlikely in homogeneous and isotropic turbulence. This tendency to not collide is still verified for anisotropic environments as the turbulent shearless mixing.

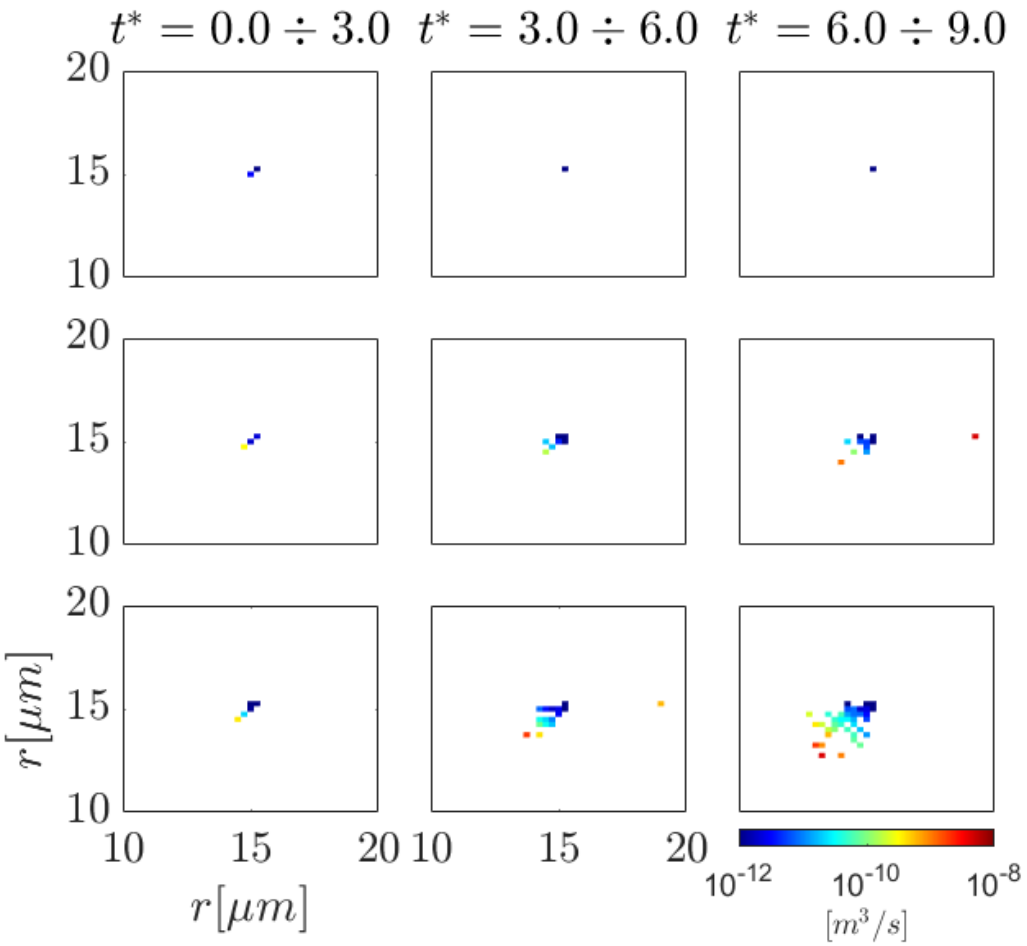

Figure 8.2. The first row describes the evolution of the collision kernel $[m^3/s]$ measured in the **cloud**, the second row is related to the **upper mixing** region between cloud and clear air. The third row contains the **lower mixing** region between cloud and clear air. The dissipation of turbulent kinetic energy decays from an initial value of $\epsilon \sim 600\, cm^2/s^3$ for HIT region and $\epsilon \sim 400\, cm^2/s^3$ for mixing region, with a $(t^*)^{-2}$ time dependence. The values associated to every kernel are respectively the mean ones in the Δt^*, so in HIT they are $\epsilon \sim 270{,}50{,}20\, cm^2/s^3$ and in upper mixing they are $\epsilon \sim 200{,}40{,}15\, cm^2/s^3$, as already reported in fig.3.3 in chapter regarding droplet collisions. The results just presented are the result of the ensemble average of four simulations. Note that here the radius bin adopted is $\Delta r = 0.25 \mu m$, it is smaller than in the previous simulations, this in order to highlight the growth of collision kernel. Since particles are very close in size they tend to not collide, in fact the number of collision in Δt^* is about an order of magnitude smaller than in the equivalent portions in multidisperse simulation.

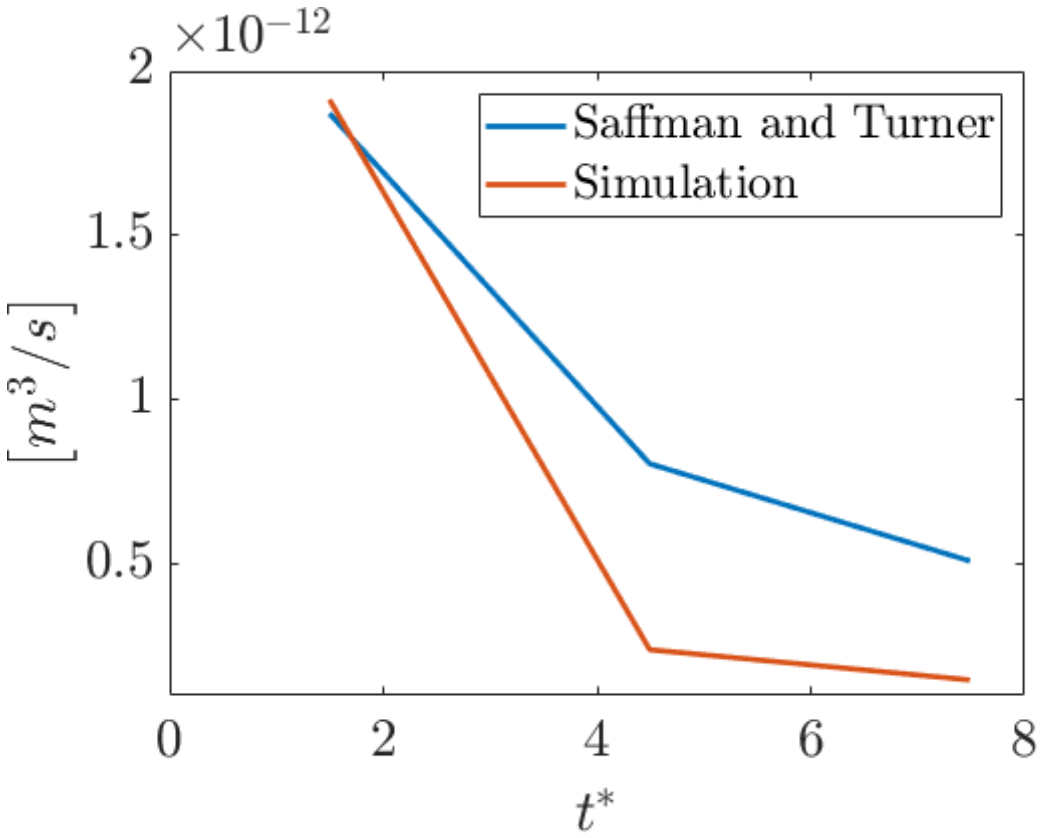

Figure 8.3. Kernels magnitude for monodisperse initial distribution of particles of $r = 15\,\mu m$ **in HIT region**. There is a good approximation of the Saffman and Turner model, that, even if it not intended for this simulation, provides a comparable prevision on the magnitude and time evolution. One can notice that globally the numerical analysis (ensemble average of four monodisperse simulations) reports lower kernel magnitude.

Chapter 9

Droplets clustering and enstrophy

The clustering of droplets consists of a non uniform spatial distribution of the liquid phase in a turbulent flow, in particular drops with greater inertia tend to move towards areas with low vorticity. This effect has been verified yet in various numerical simulations (again for example Franklin *et al*, 2005 [3]) and can be explained in a simple way studying the buoyancy due to centrifugal force in a vortex. In radial direction every drop, of density ρ_p is surrounded by fluid of density ρ_f, so it will be subjected to two opposed forces: the centrifugal one, due to the vortex, and the "bouyancy" one (the acceleration in this case is centrifugal, not gravitational), due to the different density between fluid and drop. Defining the vortex tangential velocity $v_\theta = \boldsymbol{v} \cdot \hat{\boldsymbol{t}}$, the net radial force acting on the droplet will be:

$$\boldsymbol{F} = (\rho_p - \rho_f) V \frac{{v_\theta}^2}{r} \hat{\boldsymbol{r}} \tag{9.1}$$

The radial unit vector $\hat{\boldsymbol{r}}$ points in the opposite direction to the center of the vortex. So it is easy to see that since $\rho_f << \rho_p$ the force will push away particles from the vortex center. So that is the reason for which it is hard to find particles in high enstrophy[1] regions. In case of different sizes of droplets the smallest ones, so the lightest, are the closest to the vortex center and vice versa. The way adopted to analyze this phenomenon uses the calculation of the punctual correlation on homogeneous plans.

[1]It is the measure of kinetic energy associated to turbulent vortexes.

$$\frac{1}{2} ||\nabla \times \vec{\boldsymbol{v}}||^2 \tag{9.2}$$

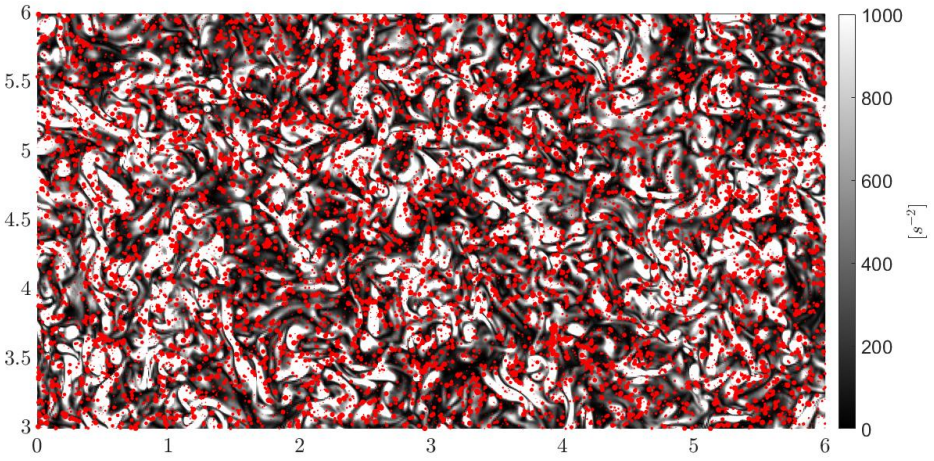

Figure 9.1. A frame of the enstrophy field at $t^* \sim 1$ on which drops are superimposed (red spots). It can be seen that particles, that are plotted in proportion with their radius (with a magnification factor of 10^6 with respect to the enstrophy field), tend to cluster into low enstrophy areas. This occurs the greater the inertia (and therefore the volume) of the particle.

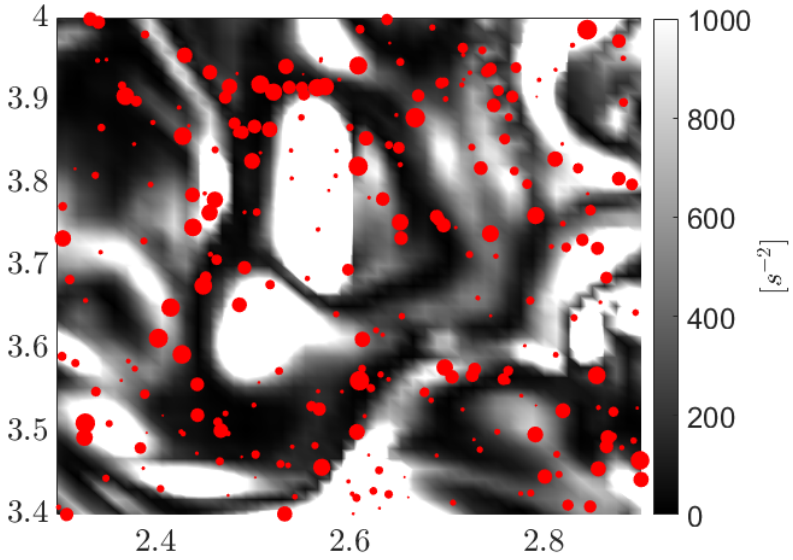

Figure 9.2. This picture is a detail of the previous one, in which filaments of droplets confined at the edges of high enstrophy vortexes are clearly visible. It appears immediately that the particles with greater inertia are those most subject to centrifugal confinement. Again it is important to remember that the size of the drops is kept proportional but enlarged with a 10^6 magnification factor with respect to the enstrophy field.

9.1 Point to point correlation algorithm

Since from our simulations we can know the enstrophy field in $512 \times 512 \times 1024$ grid points, spaced of $1\,mm$, while the particles can be everywhere in the domain, we have to match the data coordinates. In order to do so the droplets coordinates are set equal to the closest grid point, then one can sum the mass of water drops that lies in same points and divide it for the volume of a cell, in order to get the spatial density of liquid water. Since there are now two matching 3D fields it is possible to compute the point to point correlation c for each plane in the two homogeneous directions (x, y):

$$c = \frac{\sigma_{\omega\rho}}{\sigma_\omega \sigma_\rho} = \frac{\sum_{i=1}^{512}\sum_{j=1}^{512}\left(\omega_{ij} - \bar{\omega}\right)\left(\rho_{ij} - \bar{\rho}\right)}{\sqrt{\sum_{i=1}^{512}\sum_{j=1}^{512}\left(\omega_{ij} - \bar{\omega}\right)^2}\sqrt{\sum_{i=1}^{512}\sum_{j=1}^{512}\left(\rho_{ij} - \bar{\rho}\right)^2}} \tag{9.3}$$

Where ω is enstrophy and ρ is spatial density of water drops, bar symbol denotes in plane average value. At this point there is a correlation index function of the anisotropic coordinate $c\,(z)$. If you isolate portions of domain with coherent physical characteristics (the homogeneous cloud), you can calculate the average value of the correlation index, and diagram it in its temporal evolution. Regarding the mixing region the spatial averaging will not be always possible, will be shown that in some situations the correlation index is not uniform in the mixing domain.

9.2 Correlation index

In this section will be presented the results about the correlation indexes for some peculiar simulations. We will see that some aspects are common for all the simulations already treated in this work, while others will not.

9.2.1 Unstable cloud-clear air interface

From the ensemble averages made from the three simulations regarding un unstable cloud-clear air interface, applying the correlation algorithm before presented, we generated the following figures (9.3,9.5).

The first consideration that one can make is about the homogeneity along anisotropic direction: as expected the cloud region does not suffer of notable differences, the correlation index floats around a constant value. This is not true for the mixing region, that shows a bell profile along z direction. Since this situation we can study the time history of the mean value of the correlation index in the cloud region. The result, reported in fig. 9.5, shows a smooth time evolution. At the beginning the index is zero, meaning that there is not a link between droplets position and vorticity, and this is true because the initial distribution of velocity field and particle are chosen with independent random generators. Then there is a decrease until a minimum value: this is because drops are now moving towards low enstrophy, even the negative sign of the correlation is reasonable, in fact one can expect that the majority of the drops will stay in low enstrophy areas, that means inverse correlation and so a negative correlation function. Once reached the peak, it starts to lose magnitude: this can be explained by the fact that turbulence is decaying, so there is a loss in energy of the flow. The energetic vortexes that were confining particles are no

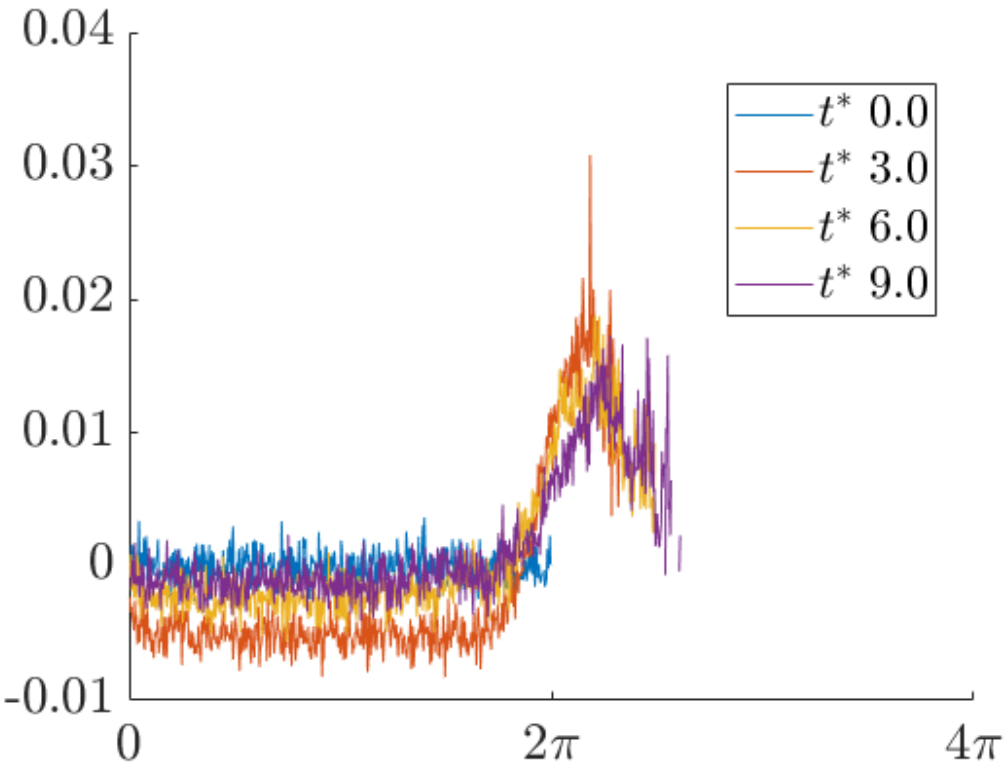

Figure 9.3. Ensemble average of correlation index between liquid water position and corresponding enstrophy level, along the anisotropic direction, at four different times. Of course in the clear air portion there are not drops, so the correlation index can not be computed.

more so strong, the enstrophy gradients are no more as sharp as in the beginning and all these factors affects the correlation, reducing the absolute value of its index. In the end we can notice that the magnitude of the correlation is weak, but since its time evolution is confirmed in other simulations and the index is always negative, one can doubt that this low intensity is not linked to the absence of correlation, but rather to the fact that the link between the position of the particles and enstrophy is not linear.

In mixing the situation is the opposite, we found positive correlation indexes, but not because particles are attracted towards high energy vortexes, but because this region has energetic vortexes alternating to very weak ones (ten times weaker) that comes from the clear air. But since particles come with the cloud, they mostly live in it, meaning that they are in the areas of the mixing that have higher enstrophy. This happens because the time interval studied is not sufficiently long to let them spread into the less energetic areas of the mixing. So that is why in this region particles position is associated to high enstrophy areas.

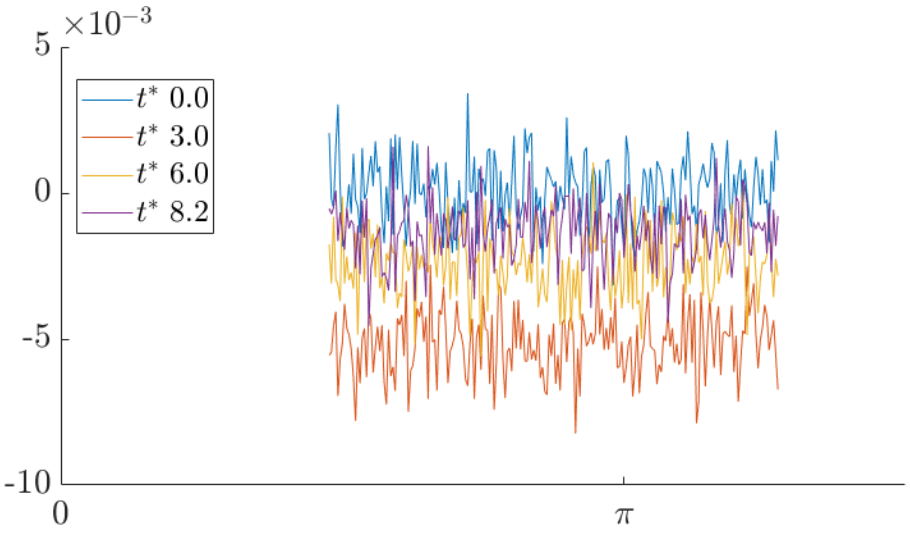

Figure 9.4. This picture represents a detail of the cloud region of fig. 9.3. It represents the ensemble average of correlation index in the cloud, along the anisotropic direction, at four different times.

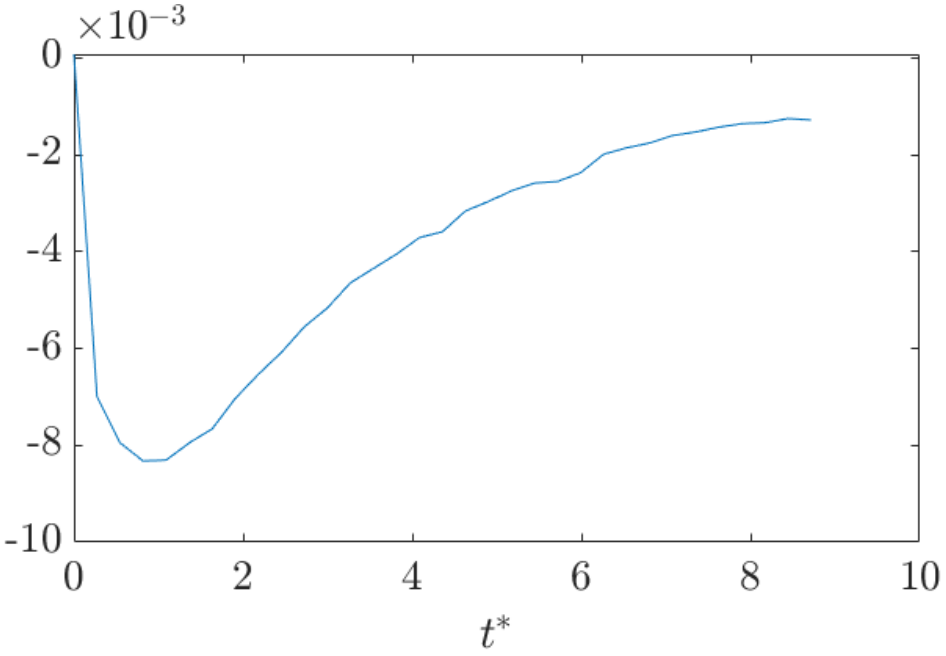

Figure 9.5. This picture is the time evolution of the correlation index mean value exposed in the previous plot. One can appreciate the smoothness of the function, the inverse correlation (highlighted by negative index throughout its evolution) and the weak magnitude of this correlation. This last information should not be interpreted as absence of correlation but but rather as an indication that the link between the position of the particles and the intensity of the enstrophy is not linear.

Since it seems that the behavior of the correlation index in time reflects the one of energy (that will be shown later in fig. 9.9, see in particular label 'High energy'), one can plot the correlation index of liquid water position and enstrophy with respect to ${u_{rms}}^2$. There is thus an almost linear dependence. The results for the HIT cloud portion (unstable simulation) are reported in fig. 9.6. Since in mixing the correlation index is not the adequate tool to evaluate whether particles actually accumulate in areas with low enstrophy, as previously mentioned, it is not presented in these analyzes.

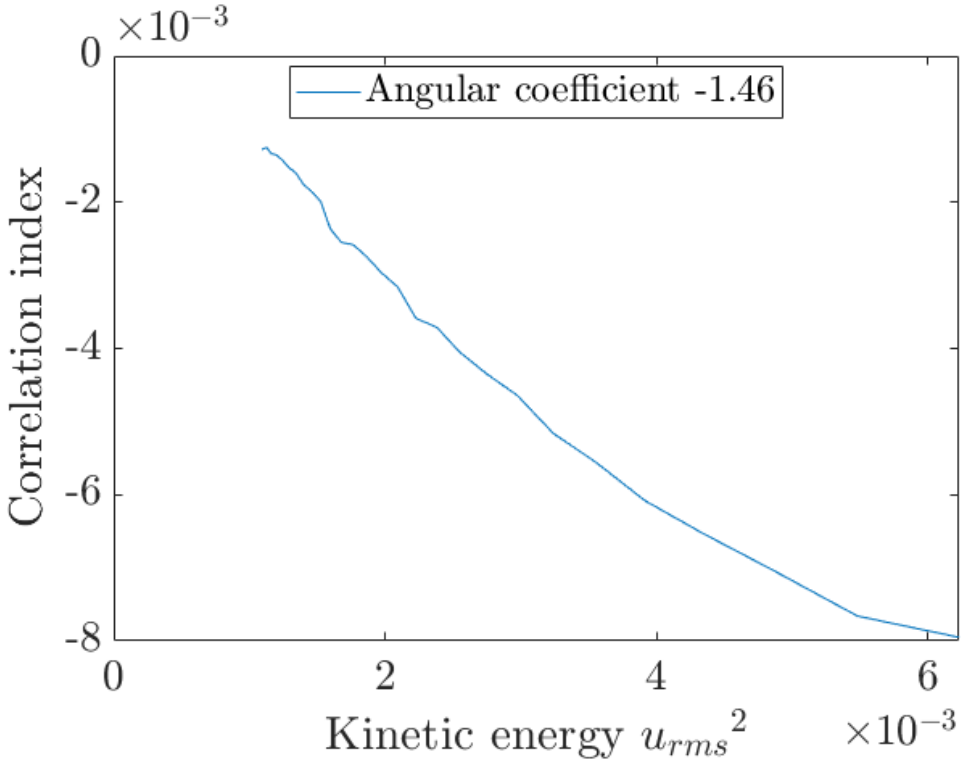

Figure 9.6. Almost linear dependence between correlation index and turbulent kinetic energy $[J/kg]$, both computed in the **homogeneous cloud portion**. Since in the mixing the correlation index is less significant it is not reported.

9.2.2 HIT cloud

In this section we briefly report the confirmation of the results before obtained into the quasi homogeneous isotropic turbulence cloud portion, as the results obtained have the same trend. The nature of this simulation involves the absence of anisotropic and mixing zones, as there are no gradients of energy, temperature and supersaturation.

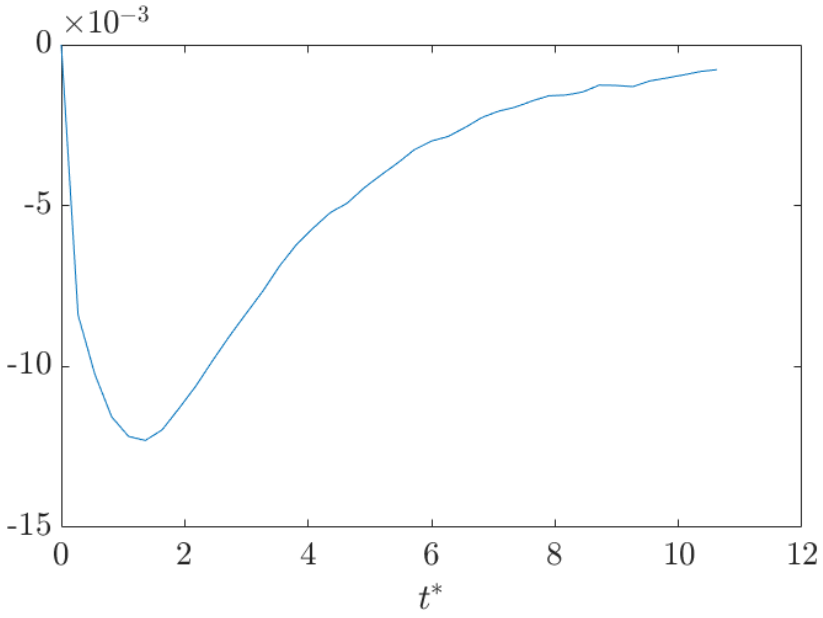

Figure 9.7. Time evolution of correlation index between enstrophy and liquid water position in a HIT cloud.

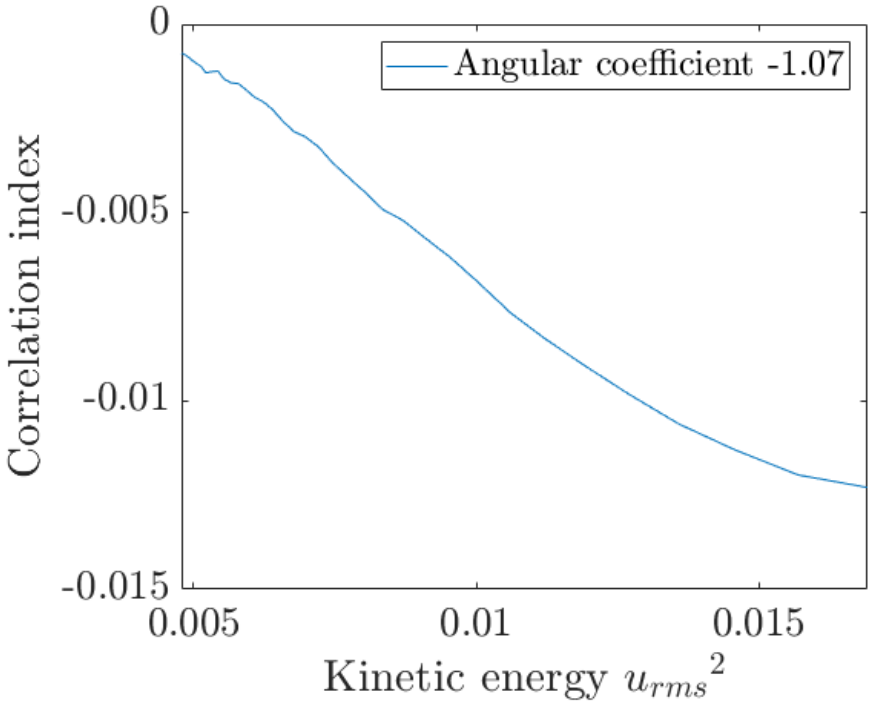

Figure 9.8. Even for this simulation is found an almost linear dependence between the correlation index and the turbulent kinetic energy $[J/kg]$, this picture refers to HIT cloud region.

9.2.3 Different energy cloud portions interface

This simulation once again confirms the results already seen for other ones, a part from the fact that here the mixing region shows the same kind of time evolution of the clouds, because in this case it has particles distributed everywhere. From this last simulation we can again see that the correlation index and the turbulent kinetic energy are decaying in the same way. So one can plot the correlation index in function of the kinetic energy, finding a linear dependence for post-peak values, as shown in picture 9.10.

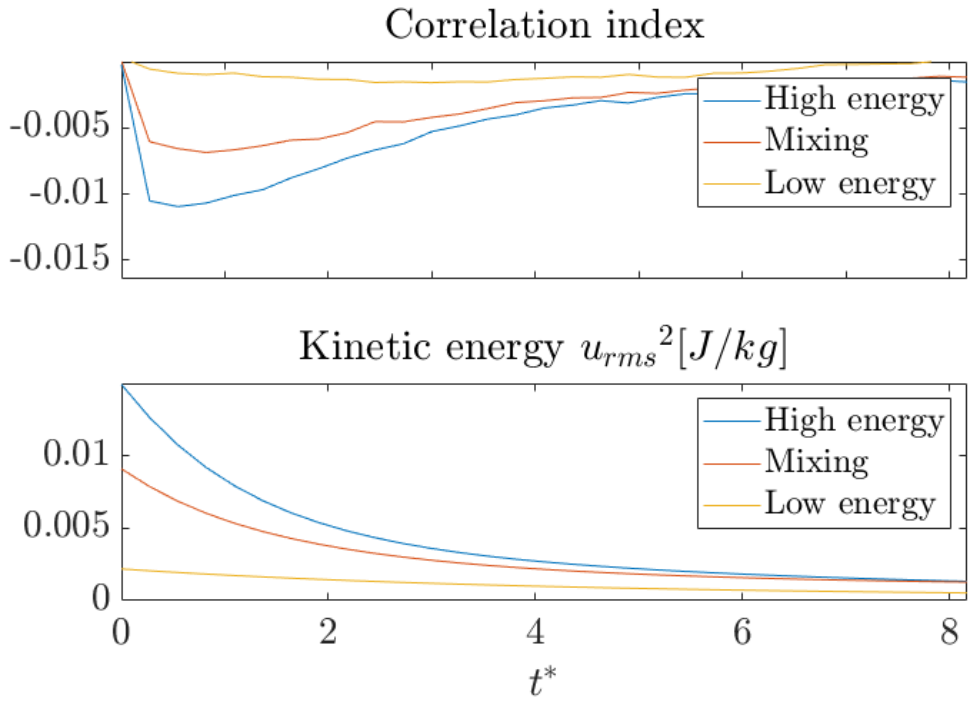

Figure 9.9. In the first image there is the time evolution of correlation index in high energy cloud, low energy cloud and the mixing region between them. The second figure shows the energy decay in time in the three portion of the domain. For this simulation is possible to plot also the result in mixing, as having particles throughout the region they can line up with the minimum values of enstrophy, which belong to the least energetic cloud. Of course the ones staying in the high energy portion of mixing are still reducing the correlation index absolute value, because in this few time they can not reach the real minimum values of enstrophy.

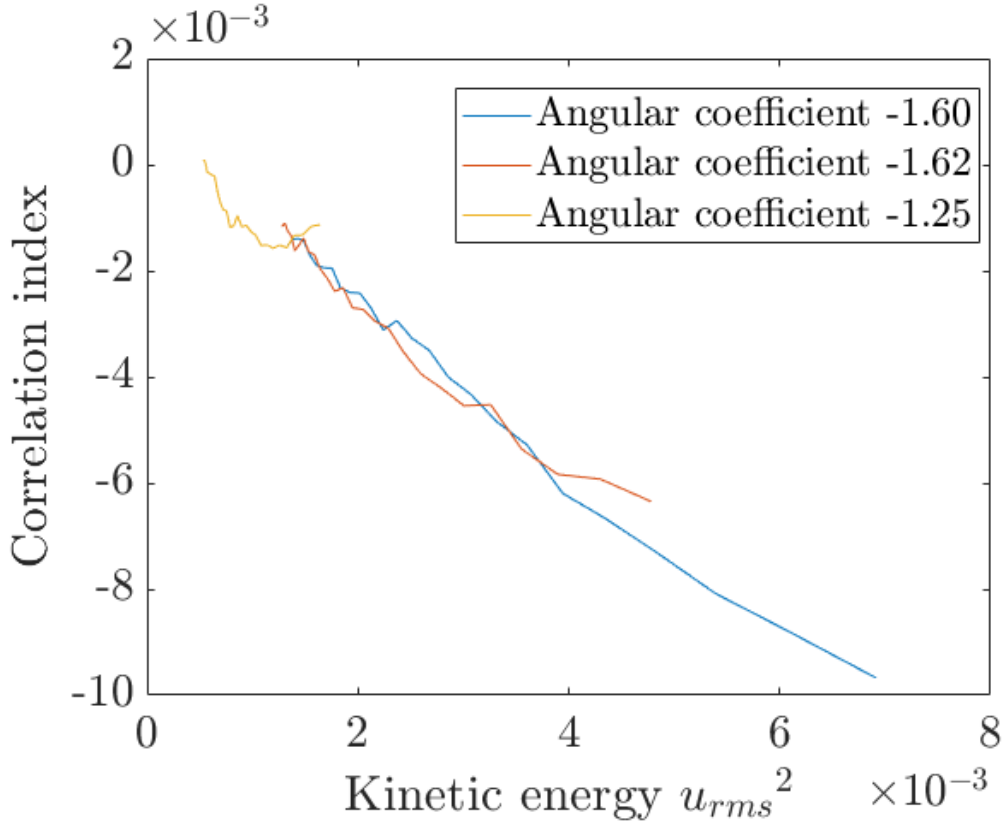

Figure 9.10. Linear dependence of correlation index with respect to the turbulent kinetic energy, in mixing and both cloud regions.

Appendix A

Saffman and Turner model

A.1 Droplets in motion with air

They described particles like spherical entities with a finite volume without inertia (zero inertia)[1] moving in an homogeneous and isotropic turbulent flow filed, in addiction they state that the body of the drops does not affect the streamlines.

Considering two species of volumetric density respectively n_1,n_2 and radius r_1, r_2; referring to the center of a particle 1, a collision will happen whenever a drop passes over the surface of a sphere of radius R, where $R = r_1 + r_2$. So it is natural to study collisions as an inward flux of drops through the surface of a sphere of radius R.
Mathematically the statistically mean flux is

$$f_{in} = -\left\langle \int_{S,u_r<0} u_r dS \right\rangle \tag{A.1}$$

Where u_r is the relative radial speed and include just negative values, in order to evaluate only the inward flux. The collision rate (per unit volume) is the flux multiplied for both volumetric densities of populations.

$$\dot{N} = -n_1 n_2 \left\langle \int_{S,u_r<0} u_r dS \right\rangle \quad [m^{-3}s^{-1}] \tag{A.2}$$

Flow is incompressible, hence the stationary continuity equation can be written as

$$\nabla \cdot \boldsymbol{u} = 0 \Rightarrow f_{in} + f_{out} = 0 \tag{A.3}$$

In particular the null flux balance leads to state that the inward flux is the half of the total flux through the sphere

$$f_{in} = \frac{1}{2}\left\langle \int_S |u_r| dS \right\rangle \tag{A.4}$$

[1] this last hypothesis is valid for $St << 1$, but allows to state that the trajectories of the particles are the streamlines of the fluid, but the sedimentation due to gravity is therefore also absent in this model.

Considering the radial direction along the x-axis

$$\langle |u_r| \rangle \equiv \langle |u_x| \rangle = R \left\langle \left| \frac{\partial u}{\partial x} \right| \right\rangle \tag{A.5}$$

Since the mean relative velocity is not a function of the position on surface it is possible to integrate A.4 substituting A.5, obtaining

$$f_{in} = 2\pi R^2 \left\langle \left| \frac{\partial u}{\partial x} \right| \right\rangle \tag{A.6}$$

The mean velocity gradient can be rewritten as state by Taylor[17]: a function of energy dissipation $\epsilon \left[\frac{m^2}{s^3}\right]$ and kinematic viscosity $\nu \left[\frac{m^2}{s}\right]$

$$\left\langle \left| \frac{\partial u}{\partial x} \right| \right\rangle = \sqrt{\frac{2\epsilon}{15\nu}} \tag{A.7}$$

Finally it is possible to write the collision rate per unit of volume

$$\dot{n}_{12} = n_1 n_2 \underbrace{(r_1 + r_2)^3 \sqrt{\frac{8\pi\epsilon}{15\nu}}}_{\Gamma_{12}} \quad [m^{-3}s^{-1}] \tag{A.8}$$

the term Γ_{12} is an element of the *collision kernel*: it describes the collision rate, known the populations of the particles involved. In this case we have a bi-dispersed set of particles, so the complete kernel is

$$\begin{aligned} \Gamma_{ij} &= \frac{\dot{n_{ij}}}{n_i n_j} \quad \left[\frac{m^3}{s}\right] \\ \Gamma &= \begin{bmatrix} \Gamma_{11} & \Gamma_{12} \\ \Gamma_{21} & \Gamma_{22} \end{bmatrix} \end{aligned} \tag{A.9}$$

The matrix is symmetric: collisions that 1 experiences with 2 are the same that 2 has with 1. The diagonal terms describes impacts between particles of the same kind.

A.2 Droplets in motion relative to air

This is the most accurate of the models presented, here the relative motion between air and drop is not neglected (but are neglected the streamlines deviations due to the presence of the droplet), so particles have a finite inertia. They assumed that the probability distribution of relative velocity between two drops is function of their distance, and if it is much smaller than the Kolmogorov's length scale[2] ($d << \eta$) it can be deduced from the particle momentum balance equation. They assumed that collision between two particles

[2]Where $\eta = \left(\frac{\nu^3}{\epsilon}\right)^{\frac{1}{4}}$ is a function only of dissipation and kinematic viscosity of the flow.

happens if the relative position of the second particle after a short time interval is included in the volume of the sphere of radius $R = r_1 + r_2$ around the first particle.

$$\|\mathbf{r_2} + \mathbf{w}\delta t - \mathbf{r_1}\| < R \tag{A.10}$$

In doing this is assumed that[3] $\delta t << \tau_\eta$ so that the relative velocity ($\mathbf{w}$) times this small time interval (δt) gives, in approximation, a straight line trajectory. Integrating over all the probability distribution is possible to compute the collision rate for two populations:

$$\dot{N} = \pi R^2 n_1 n_2 \int \|\mathbf{w}\| \, P(\mathbf{w}) d\mathbf{w} \tag{A.11}$$

This last equation can be written only if n is statistically independent from $\mathbf{w}$.Now, instead of look for $P(\mathbf{w})$, they computed the variance of $\mathbf{w}$. Recalling that $\mathbf{w}$ is simply the difference of absolute velocities of the two drops $\mathbf{c}$, where this one is the flow velocity $\mathbf{u}$ plus the particle relative velocity respect to the flow $\mathbf{q}$, and if they are statistically independent is

$$var(\mathbf{w}) = var(\mathbf{c_2} - \mathbf{c_1}) = var(\mathbf{q_2} - \mathbf{q_1}) + var(\mathbf{u_2} - \mathbf{u_1}) \tag{A.12}$$

For isotropic turbulence is known that for small eddies

$$var(\mathbf{u_2} - \mathbf{u_1}) = R^2 \frac{\epsilon}{3\nu} \tag{A.13}$$

They evaluated the variance of relative fluid/particle velocity from the droplet momentum equation

$$\dot{\mathbf{c}} = \underbrace{\frac{9}{2}\frac{\rho_a}{\rho_p}\frac{\nu_a}{r^2}(\mathbf{u} - \mathbf{c})}_{\text{Stokes drag}} + \underbrace{\left(1 - \frac{\rho_a}{\rho_p}\right)\mathbf{g}}_{\text{Gravity}} + \underbrace{\frac{\rho_a}{\rho_p}\dot{\mathbf{u}}}_{\text{Added mass effect}} \tag{A.14}$$

Assuming that:

- The flow is characterized by homogeneous and isotropic turbulence (in our simulations we have a decaying turbulent field, with a direction of anisotropy, therefore this model would not be suitable to represent the collisions that occur in our simulations)
- The particles relaxation time is much smaller than the Kolmogorov time scale

$$\tau_p = \frac{9}{2}\frac{r^2}{\nu_a} << \tau_\eta \Rightarrow \frac{d\mathbf{q}}{dt} \simeq 0 \tag{A.15}$$

- Mediating over time, in addition to the first assumption

$$\overline{\left(\frac{d\mathbf{u}}{dt}\right)^2} \simeq 3\overline{\left(\frac{D\mathbf{u}}{Dt}\right)^2} \tag{A.16}$$

- The undisturbed flow velocity for two colliding particles is the same

[3] τ_η is the Kolmogorov time scale, computed as $\tau_\eta = \sqrt{\frac{\nu}{\epsilon}}$

They obtained

$$var(\mathbf{q_2} - \mathbf{q_1}) = (\tau_2 - \tau_1)^2 \left(1 - \frac{\rho_a}{\rho_p}\right)^2 \left[3\overline{\left(\frac{D\mathbf{u}}{Dt}\right)^2} + \mathbf{g}^2\right] \tag{A.17}$$

That leads to

$$var(\mathbf{w}) = (\tau_2 - \tau_1)^2 \left(1 - \frac{\rho_a}{\rho_p}\right)^2 \left[3\overline{\left(\frac{D\mathbf{u}}{Dt}\right)^2} + \mathbf{g}^2\right] + R^2 \frac{\epsilon}{3\nu} \tag{A.18}$$

At this point they chose as a $P(\mathbf{w})$ a gaussian function, characterized by having $var(\mathbf{w})$ as variance, in order to easily evaluate the integral of $\dot{N}$. Hence their analytical formulation of the kernel $\Gamma = \frac{\dot{N}}{n_1 n_2}$ is

$$\mathbf{\Gamma} = 2\sqrt{2\pi}R^2 \left[\left(1 - \frac{\rho_a}{\rho_p}\right)^2 (\tau_2 - \tau_1)^2 \overline{\left(\frac{D\mathbf{u}}{Dt}\right)^2} + \frac{1}{3}\left(1 - \frac{\rho_a}{\rho_p}\right)^2 (\tau_2 - \tau_1)^2 \mathbf{g}^2 + R^2 \frac{\epsilon}{9\nu}\right]^{\frac{1}{2}} \tag{A.19}$$

It is very important to notice that $(\mathbf{u}, \mathbf{g})$ in the right hand side of the equations are considered in their magnitude, their direction does not affect the kernel, they are scalar quantities. The dependence from turbulence is linked to the dissipation ϵ that in this model is constant in time (steady state turbulence), and also to the mean derivative of flow field velocity in time. This last term can be evaluated in module from dissipation, using the Batchelor approximation (1951) [1]:

$$\overline{\left(\frac{D\mathbf{u}}{Dt}\right)^2} \simeq 1.3 \frac{\epsilon^{3/2}}{\nu^{1/2}} \tag{A.20}$$

At this point, knowing the energy dissipation of the turbulent field, one can plot the Saffman and Turner collision kernel for water droplets in a cloud, as reported in figure A.1.

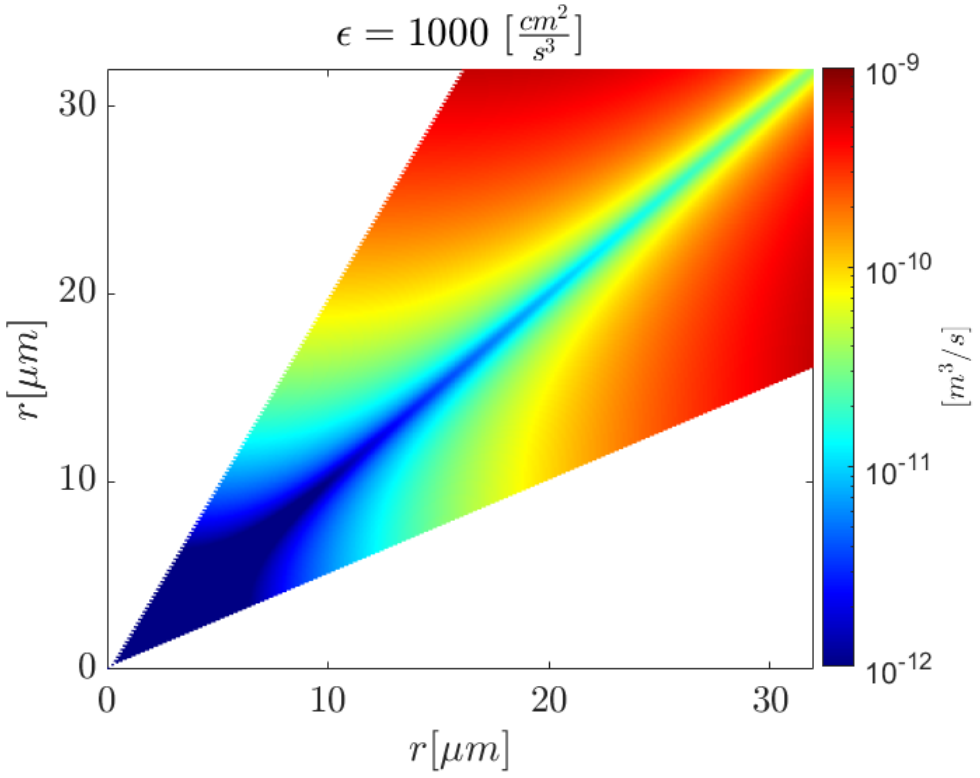

Figure A.1. Saffman and Turner collision kernel (from A.19), the limits on radius ratio does not allow to have information about some areas of the kernel that will be computed in this job.

A.2.1 Collision efficiency

The limits of these two models are due to the collision efficiency: this number ranges from 0 to 1, and expresses the probability that two particles, that are supposed to collide, will not because of the flow distortion around them. Saffman and Turner set this efficiency to 1, specifying that this is true only for ratios between the radii not bigger than 2.

A.3 Reduced model

Since we have a slightly different model to describe the particles momentum 1.30, we derived an analytical kernel based on our momentum equation, tracing the work done by Saffman and Turner. Our starting balance equation neglects the influence of fluid acceleration (the

"added mass" term[4]), considering only Stokes drag and gravity effect:

$$\dot{\mathbf{c}} = \underbrace{\frac{(\mathbf{u}-\mathbf{c})}{\tau_p}}_{\text{Stokes drag}} + \underbrace{\left(1-\frac{\rho_a}{\rho_p}\right)\mathbf{g}}_{\text{Gravity}} \tag{A.22}$$

Following the same steps as before we obtained

$$\mathbf{\Gamma} = \frac{2\sqrt{2\pi}}{3}R^2\left[3\left(1-\frac{\rho_a}{\rho_p}\right)^2(\tau_2-\tau_1)^2\mathbf{g}^2 + R^2\frac{\epsilon}{\nu}\right]^{\frac{1}{2}} \tag{A.23}$$

Recalling that the analytical derivation is valid only for steady and homogeneous isotropic turbulence, we can provide how different from the analytical previsions will be the measured kernel. We adopt the analytical model of collision kernel in time dependent processes considering the numerical kernels as they were in a sequence of steady state homogeneous isotropic turbulent fields. The pattern of kernel A.23 is reported in fig. A.2.

We computed the difference between the reduced kernel formula and the Saffman and Turner one, for different dissipation values, in order to see how different is the approximation adopted in this work.

The difference has been computed as a relative error from Saffman and Turner model (Γ_{ST}) for each couple of radius, and it shows that there is an underestimation that quickly tends to zero as the dissipation decays.

$$\frac{\Gamma_{ST} - \Gamma_{reduced}}{\Gamma_{ST}} \tag{A.24}$$

The detailed results are reported in fig. A.3, briefly one can highlight that in the beginning of our simulations we always have $\epsilon \sim 500\,cm^2/s^3$, that implies a 5% underestimation error. In a bit more than one eddy turnover time the dissipation is halved and the error is reduced to values close to 1%.

[4]The maximum $\frac{du}{dt}$ measured is $\sim 15g$, so the added mass acceleration term has a maximum order of magnitude $\sim 0{,}15\,m/s^2$ since it is multiplied by the air to water density ratio. Compared to the buoyant term, that has an order of magnitude of $\sim 10\,m/s^2$, it is negligible. This is reported in details in fig. A.3

$$\underbrace{\left(1-\frac{\rho_a}{\rho_p}\right)\mathbf{g}}_{\simeq 10} >> \underbrace{\frac{\rho_a}{\rho_p}\dot{\mathbf{u}}_{max}}_{\simeq 0.15} \tag{A.21}$$

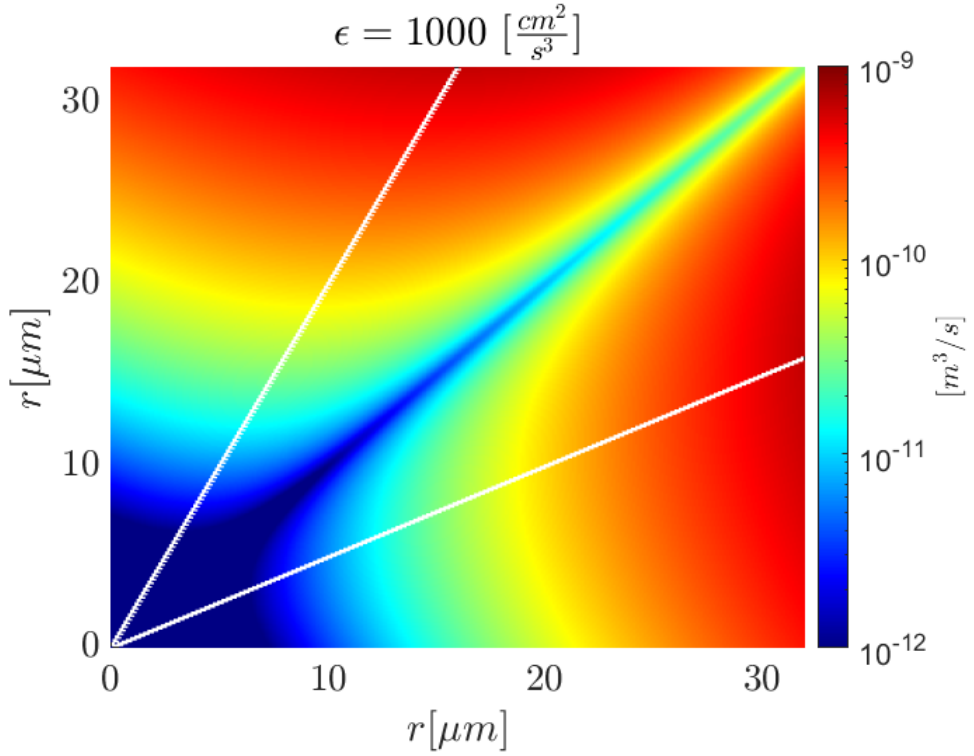

Figure A.2. Collision kernel for the reduced model (A.23), the white lines represents the boundaries of radii ratio less than 2.

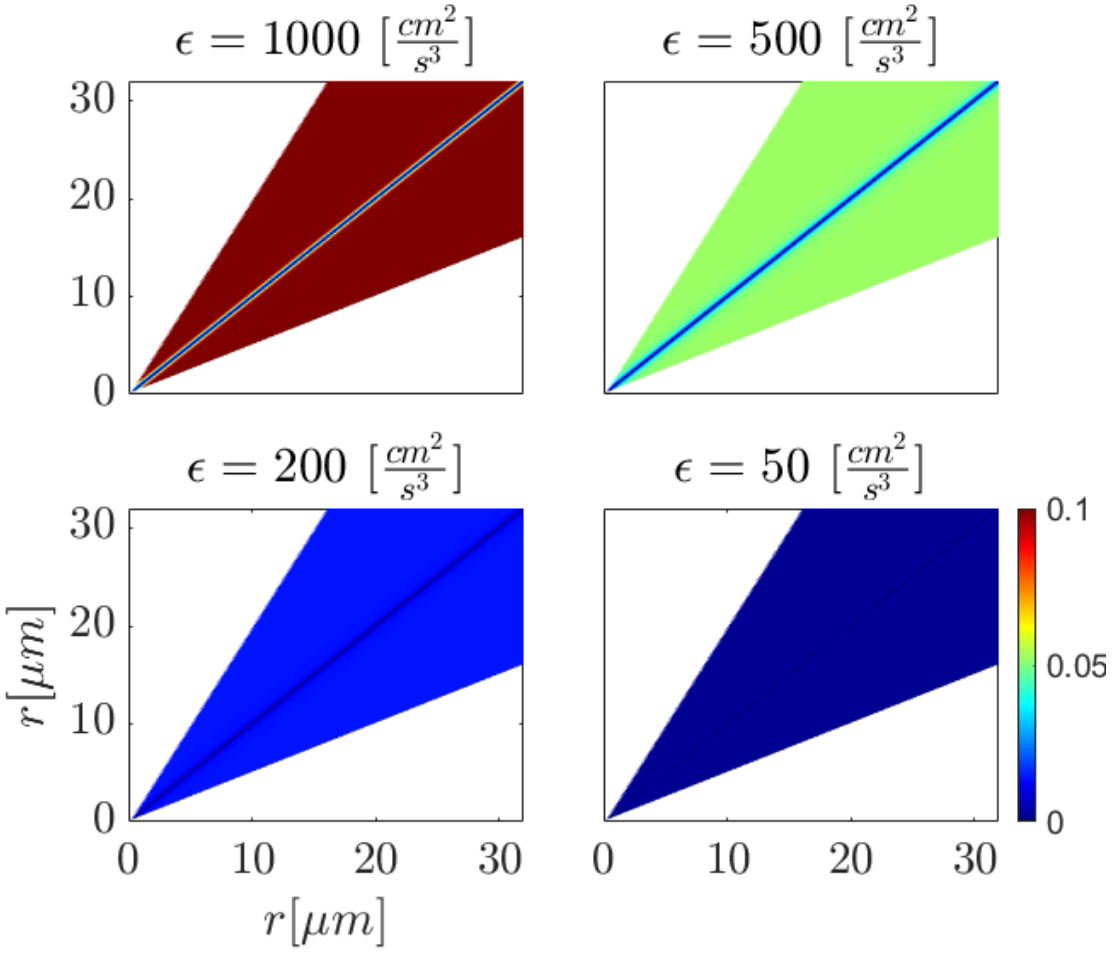

Figure A.3. The picture reports the underestimation percentage that is made adopting the reduced model. Since in all our simulations the maximum value of dissipation is $\sim 500\, cm^2/s^3$ we can see that the error between the two formulation is at most 5%, but since the dissipation decay as t^{-2} this error quickly tends to zero. Again the white lines delimit the kernel in Saffman and Turner hypothesis.

A.4 Analysis of some kernel properties

This section concerns the physical properties of the Saffman and Turner model for inertial particles immersed in a turbulent flow. As shown from the following formulation there are two terms that determines the behavior of the kernel: the ones related to the fact that drops are inertial objects and the other due to turbulent transport acting on droplets.

$$\mathbf{\Gamma} = 2\sqrt{2\pi}R^2 \left[\underbrace{\left(1-\frac{\rho_a}{\rho_p}\right)^2 (\tau_2-\tau_1)^2 \overline{\left(\frac{D\mathbf{u}}{Dt}\right)^2} + \frac{1}{3}\left(1-\frac{\rho_a}{\rho_p}\right)^2 (\tau_2-\tau_1)^2 \mathbf{g}^2}_{\text{Partcle inertial effects}} + \underbrace{R^2\frac{\epsilon}{9\nu}}_{\text{Passive transport}} \right]^{\frac{1}{2}}$$

A.4.1 Inertial effects

This fluid dynamic effect is the one describing the contribution to the collisions of the acceleration of the flow field (the so called "added mass") and the gravitational field. It is natural now to look at which is their contribution to kernel magnitude.

It is clear from figs. A.4 A.5 that with an initial dissipation of $\epsilon \simeq 500\ [cm^2/s^3]$, both terms act in the same way, but the gravitational one is more influencing the collision dynamics.

The inertial term is the responsible of the shape of the kernel: in other words the dependence from the difference between the relaxation time of two particles is the reason why collisions between equal droplets are very unlikely. In fact this can be explained underlining that two particles which have same inertia (same radius) will follow in the same way the streamlines, so since streamlines do not cross each other, the particles will not too.

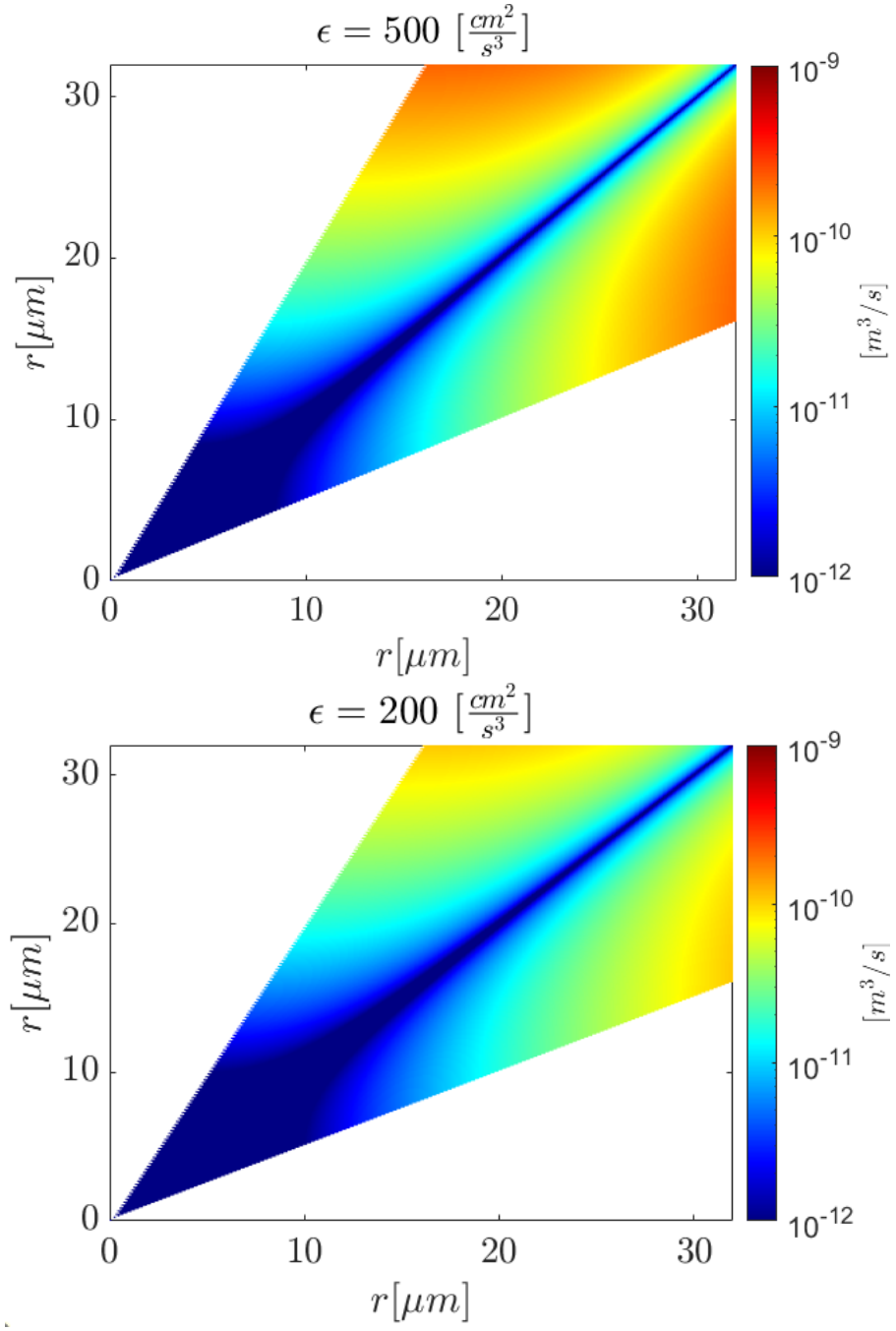

Figure A.4. The figure reports the kernels if they were computed only using added mass with two different values of dissipation.

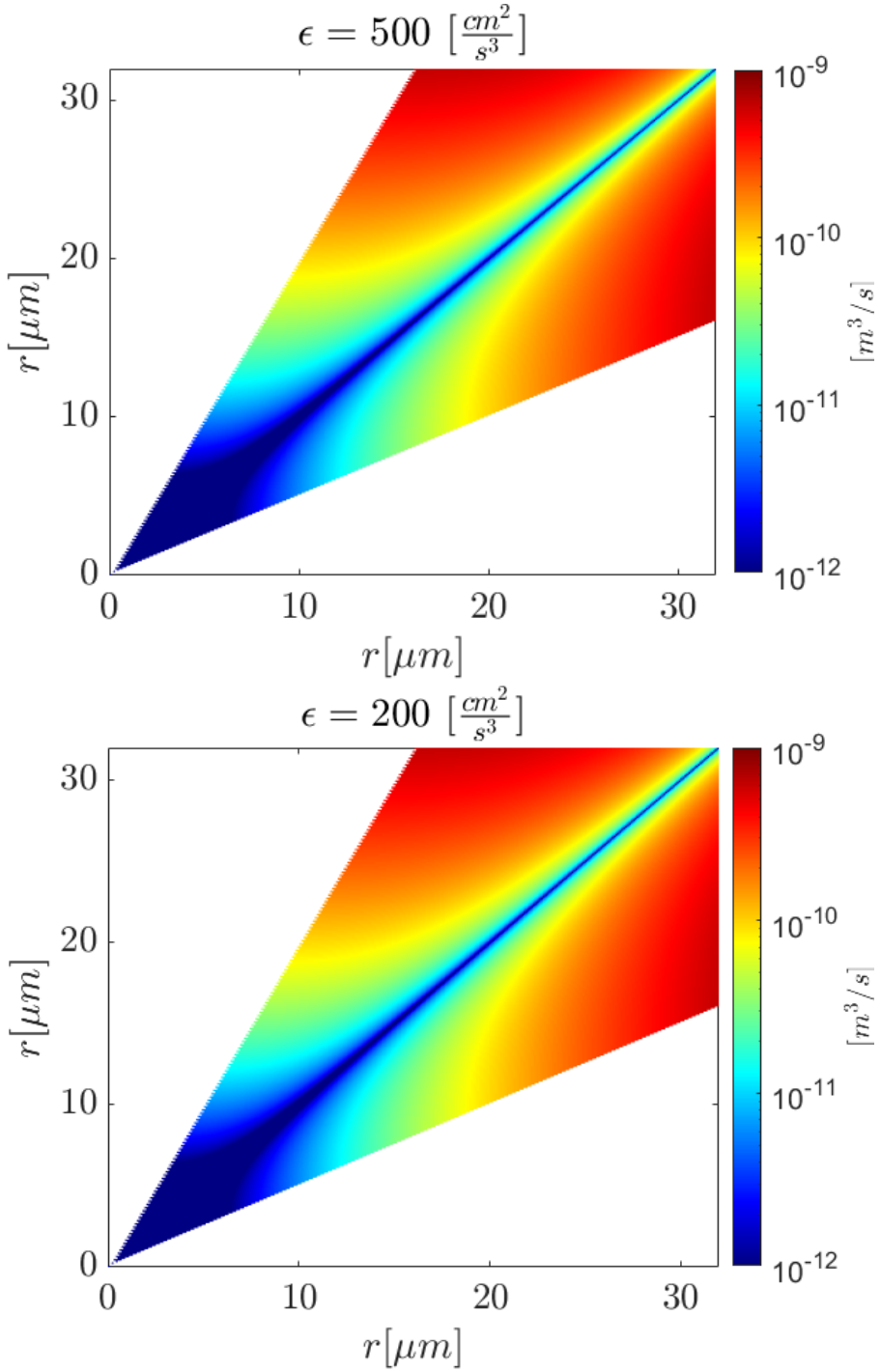

Figure A.5. The figure reports the kernels if they were computed only using gravitational field, with two different values of dissipation.

A.4.2 Transport effect

The remaining term that has to be evaluated comes from the turbulent transport affecting the particles. The dependence of the kernel is well described in the following formula:

$$\mathbf{\Gamma} \propto (r_1 + r_2)^3 \sqrt{\frac{\epsilon}{\nu}} \tag{A.25}$$

There is a clear square root dependence from the dissipation, that acts on the collision probability of every couple of colliding particles, and a dependence on the sum of the radii of the colliding particles. This last effects enhances the collision probability among large drops, it will appear clearly from fig. A.6.

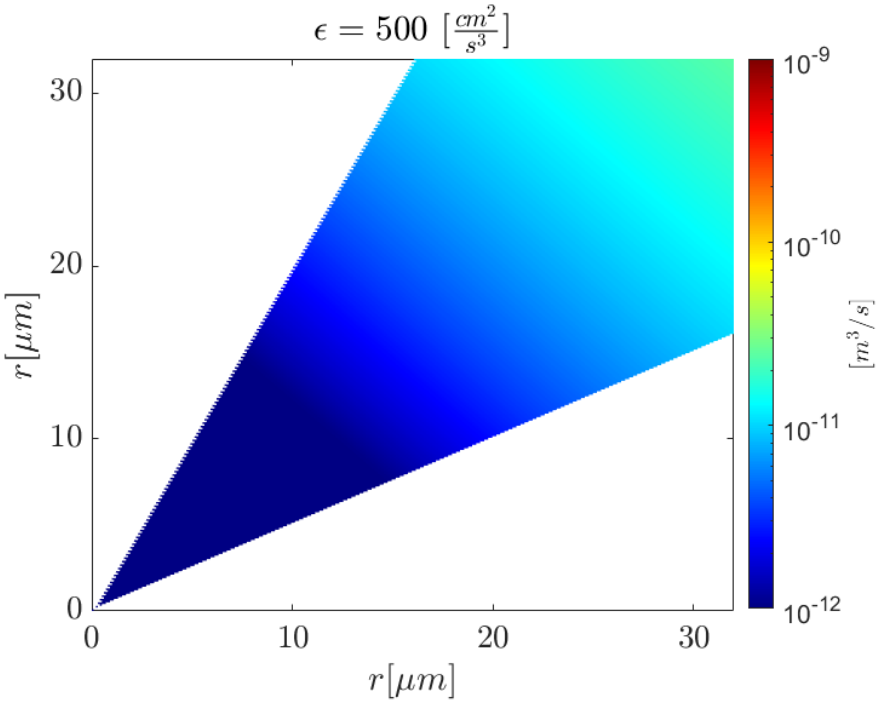

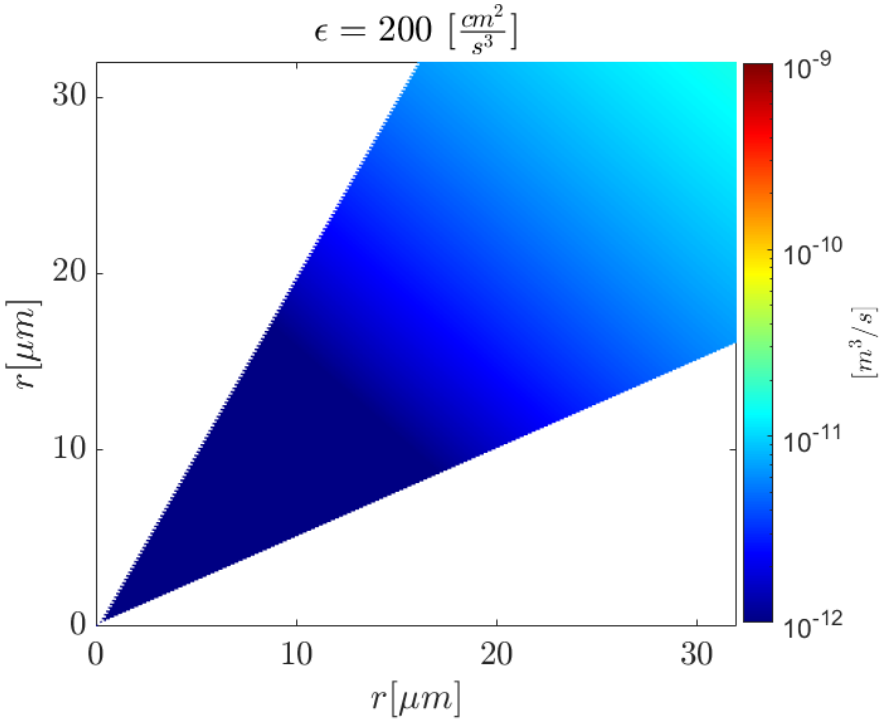

Figure A.6. Collision kernel transport term computed at two significant dissipation levels. The stripe-like pattern is due to the $(r_1 + r_2)^3$ dependence.

Bibliography

[1] Batchelor G. K., 1951. *The application of the similarity theory of turbulence to atmospheric diffusion*. Q. J. R. Meteorol. Soc.

[2] Devenish B.J., Bartello P., Brenguier J.-L., Collins L.R., Grabowski W.W., IJzermans R.H.A., Malinowski S.P., Reeks M.W., Vassilicos J.C., Wang L.-P., Warhaft Z. 2012. *Droplet growth in warm turbulent clouds*. Q. J. R. Meteorol. Soc. 138: 1401–1429. DOI:10.1002/qj.1897

[3] Franklin C.N., Vaillancourt P.A., Yau M.K. and Bartello P., 2005. *Collision Rates of Cloud Droplets in Turbulent Flow*. J. Atmos. Sci., 62, 2451–2466.

[4] Gallana L., 2012. *High resolution numerical simulation of the turbulent transport of a passive scalar by using a new pencil parallelization method suitable for massive parallelized machines*, Master thesis, Politecnico di Torino.

[5] Ghan S.J., Abdul-Razzak H., Nenes A., Ming Y., Liu X., Ovchinnikov M., Shipway B., Meskhidze N., Xu J., Shi X., 2011. *Droplet nucleation: physically-based parameterizations and comparative evaluation*. Journal of Advances in Modeling Earth Systems.

[6] Howell W., 1949. *The growth of cloud drops in uniformly cooled air*. Journal of meteorology.

[7] Iovieno M., Cavazzoni C., Tordella D., 2001. *A new technique for a parallel dealiased pseudospectral Navier-Stokes code*. Computer Physics Communications 141(2001) 365-374.

[8] Iovieno M., Tordella D., 2011. *Small scale anisotropy in turbulent sherless mixing*. Physical Review Letters (PRL 107,194501).

[9] Kumar B., Schumacher J., december 2011, *Cloud microphysical effects of turbulent mixing and entrainment*, Theoretical and Computational Fluid Dynamics

[10] Maxey M., Riley J., 1982, *Equation of motion for a small rigid sphere in a nonuniform flow*, The Physics of Fluids 26, 883 (1983); DOI: 10.1063/1.864230

[11] Mozurkewich M., 1986, *Aerosol Growth and the Condensation Coefficient for Water: A Review*, Aerosol Science and Technology, 5:2, 223-236, DOI: 10.1080/02786828608959089

[12] Ovadnevaite, J., Zuend, A., Laaksonen, A. et al., 2017, *Surface tension prevails over solute effect in organic-influenced cloud droplet activation*, Nature 546, 637–641. https://doi.org/10.1038/nature22806

[13] Saffman P.G., Turner J.S., 1956, *On the collision of drops in turbulent clouds*, J. Fluid Mech. 1: 16–30.

[14] Saito I., Gotoh T., Watanabe T., 2019, *Broadening of cloud droplet size distributions by condensation in turbulence*. Journal Of The Meteorological Society Of Japan

2019;19:867–91.

[15] Siebert H., Franke H., Lehmann K., Maser R., Ewe Wei Saw, Schell D., Shaw R. A., Wendisch M., 2006, *Probing Finescale Dynamics and Microphysics of Clouds with Helicopter-Borne Measurements*, Journal of American Meteorological Society.

[16] Smoluchowski M., 1916, *Drei Vorträge über Diffusion, Brownsche Molekularbewegung und Koagulation von Kolloidteilchen*. Phys. Z. (in German). 17: 557–571, 585–599.

[17] Taylor G.I., 1935, *Statistical theory of turbulence*, Proc. Roy. Soc. A, 151, 429

[18] Yau M.K.,Rogers R.R., 1996, *A short course in cloud physics*, Elsevier